2015

Implementation of fringe projection profilometry using triangular fringe patterns and spatial shift estimation

Pu Cao
University of Wollongong, pc241@uowmail.edu.au

IMPLEMENTATION OF FRINGE PROJECTION PROFILOMETRY USING TRIANGULAR FRINGE PATTERNS AND SPATIAL SHIFT ESTIMATION

A thesis submitted in fulfilment of the requirement for the award of the degree of

Doctor of Philosophy

from

University of Wollongong

By

PU CAO

B.E, Huazhong University of Science and Technology, China

Master of Engineering Research, University of Wollongong

School of Electrical, Computer and Telecommunications Engineering

2015

CERTIFICATION

I, Pu Cao, declare that this thesis, submitted in partial fulfilment of the requirements for the award of Doctor of Philosophy, in the School of Electrical, Computer & Telecommunications Engineering, University of Wollongong, is wholly my own work unless otherwise referenced or acknowledged. The document has not been submitted for qualifications at any other academic institution.

Pu Cao

23 March 2015

TABLE OF CONTENT

LIST OF TABLES

LIST OF FIGURES

LIST OF ABBREVIATIONS

3D	Three-dimensional
DFP	Digital fringe projection
FPP	Fringe pattern profilometry
IFSE	Inverse function-based shift estimation
PDE	Phase difference estimation
SSE	Spatial shift estimation
CCD	Charge-coupled device
FTP	Fourier transform profilometry
PSP	Phase shifting profilometry

ABSTRACT

As an enabling technology for non-contact three-dimensional (3D) profile measurement, fringe pattern profilometry (FPP) has attracted intensive research due to the advantages of high accuracy, high speed and simply in implementation. Popular FPP approaches retrieve the 3D profile information based on the detection of phase differences. Recently, an alternative FPP approach, referred to as spatial shift estimation (SSE), has been proposed, which retrieves the 3D profile information based on spatial shifts. In contrast to phase difference estimation approaches, SSE approaches are advantageous as the fringe patterns do not need to be sinusoidal, and accurate reconstruction can be obtained even when nonlinear distortions exist on the fringe patterns. However, efficient implementation of SSE approaches is still an issue.

This thesis aims to implement the SSE approach for FPP. Firstly, a digital fringe projection (DFP) system is designed and implemented, which is used as an experimental platform for the work presented in this thesis. A few problems associated with the implementation are studied and solved, including elimination of noise and distortion in the fringe patterns. An improved inverse function-based shift estimation method is then proposed to improve the performance of SSE approaches, which greatly reduced the computation time. Based on analysis of the limitations of traditional sinusoidal fringe patterns, a triangular fringe pattern is proposed. Theoretical analysis is presented to evaluate the complexity of the proposed triangular fringe pattern based algorithms, and practical experiments are performed to prove the efficiency of this proposed fringe pattern.

Secondly, the shift unwrapping problem associated with SSE is investigated. Based on a review of the phase unwrapping problem in phase difference estimation based FPP, a reliability-guided algorithm and a multiple-wavelength algorithm are proposed to unwrap the shift map. Experiments are presented to demonstrate the effectiveness of

the methods proposed.

Finally, a selected-frequency shift unwrapping algorithm is proposed. An improved method is then introduced that uses selected wavelengths instead of frequencies. Combining the multiple methods introduced in the thesis, a novel 3D shape measurement method based on the projection of triangular patterns of two selected wavelengths is proposed. This method successfully solves the shift unwrapping problem of complex object surfaces with significant step heights or multiple separate objects, with the efficiency also increased since fewer images are used.

ACKNOWLEDGEMENT

I wish to express my deepest appreciation to all the people that have contributed to the completion of this thesis. First of all, I would like to express my genuine gratitude to Professor Jiangtao Xi, Dr Yanguang Yu and Dr Qinghua Guo, my supervisors, for their invaluable guidance and encouragement in the research and preparation of this thesis. Without their patience, this work would not be possible.

I sincerely thank Dr Matthew J. Baker and Dr Yingsong Hu for sharing their knowledge and experience in the area of three-dimensional profile measurement by digital video fringe projection. They gave me patient and valuable direction throughout the experiment process.

I am also indebted to all my best friends for their friendship and supports.

Finally, I would like to thank my grandmother and my parents for their endless love, which encourages me to overcome all problems.

LIST OF PUBLICATIONS

Pu Cao, Jiangtao Xi, Yanguang Yu, Qinghua Guo and Limei Song, “3D shape measurement based on projection of triangular patterns of two selected frequencies,” Optics Express, Vol. 22, No. 23, PP. 29234-29248, 2014.

Pu Cao, Jiangtao Xi, Yanguang Yu and Qinghua Guo, “Spatial shift unwrapping for digital fringe profilometry based on spatial shift estimation,” Journal of Electronic Imaging, Vol. 23, No. 4, PP. 043002, 2014.

Pu Cao, Jiangtao Xi, Yanguang Yu and Qinghua Guo, “Digital fringe profilometry based on triangular fringe patterns and spatial shift estimation,” in *Dimensional Optical Metrology and Inspection for Practical Applications III*, Proceedings of SPIE, Vol. 9110, PP. 91100C, 2014.

Pu Cao, Jiangtao Xi, Yanguang Yu and Qinghua Guo, “A multiple wavelength unwrapping algorithm for digital fringe profilometry based on spatial shift estimation,” in *Three-Dimensional Image Processing, Measurement, and Applications 2014*, Proceeding of SPIE, Vol. 9013, PP. 90130E, 2014.

Pu Cao, Jiangtao Xi, Joe Chicharo and Yanguang Yu, “A fringe period unwrapping technique for digital fringe profilometry based on spatial shift estimation”, in *Optical Inspection and Metrology for Non-Optics Industries*, Proceedings of SPIE, Vol. 7432, PP. 743208, 2009.

Chapter 1 Introduction

In recent years, optical non-contact three-dimensional (3D) profile measurement has attracted increasing research efforts due to the increasing demands in many such applications as machine vision, animation, intelligent robot control, virtual reality, industrial monitoring, biomedicine, dressmaking and ergonomics. Among other approaches, fringe pattern profilometry (FPP) based on digital fringe projection (DFP) has been proven to be one of the most promising techniques for non-contact 3D profile measurement. Compared with other methods, FPP has the advantages of a simple system structure, high accuracy and speed. It, therefore, provides a flexible and practical approach for 3D profile measurement.

Although many FPP approaches have been introduced, the most widely used methods are those that use phase difference estimation (PDE). In these approaches, the deformed fringe pattern is considered to be the result of phase modulation of the original fringe pattern. Detection of phase maps from the original and the deformed fringe patterns enables retrieval of the 3D shape. Although PDE approaches have been the most popular, they suffer from a number of disadvantages. A major restriction is that the fringe patterns must be either sinusoidal or ideal periodic. This requirement is hard to meet in practice due to such factors as the nonlinear distortion inherent in digital video projections. To solve this problem, a new profilometry approach, called spatial shift estimation (SSE) profilometry was proposed, which is based on the estimation of spatial shift for corresponding pixels on the deformed and original fringe patterns.

This research aims to implement the SSE approach to profilometry. The implementation is achieved through the design of a DFP system, development of solutions for the unwrapping problems that are inherent in the SSE approach, and the proposal of a novel 3D shape measurement method based on SSE to improve efficiency.

This chapter gives the rationale and background knowledge for this thesis, which is organised as follows. Section 1.1 introduces 3D profile measurement and DFP. Section 1.2 presents a comprehensive literature review that encompasses the background of DFP systems and FPP approaches, including PDE and SSE. Section 1.3 discusses the issue associated with the implementation of SSE approaches. Section 1.4 descibes the aim of the thesis' work. Section 1.5 discusses the contribution of the research work. Section 1.6 gives the structure of this thesis.

1.1 General Introduction

1.1.1 3D Profile Measurement

Over the past few decades, a number of optical methods for 3D profilometry have been proposed [1]. Some significant approaches include: photogrammetry methods [2], such as stereovision [3, 4], shape from shading [5], shape from texture [6] and shape from focusing [7, 8]; interferometric methods, including two or multiple wavelenghs [9 - 12], reactive index [13 - 15] and illumination direction or number of sources [16, 17]; moiré methods [18, 19]; time of flight methods [20, 21]; and structured light methods [22] such as code structure light [23], faster scanning [24] and fringe projection. Structured light methods, including fringe profilometry, became one of the most popular techniques, especially since recent progress in DFP technology has provided the required attributes for the development of dynamic and more robust structured light methods.

1.1.2 3D Profile Measurement using DFP

Compared with other structured light methods, FPP based on DFP is particularly attractive due to the advantages of a simple system structure and controllable fringe patterns [25]. Figure 1.1 shows the structure of a FPP system, consisting of a digital

video projector, a charge-coupled device (CCD) camera and the reference plane. A set of images with a particular fringe pattern are cast respectively onto the reference plane and the surface of the object and the reflections are captured by the CCD camera. Due to variance in the height of the object's surface, the image patterns reflected from the object's surface are a deformed version of the image patterns from the reference plane. These deformed patterns carry information about the shape of the object's surface and can be used to retrieve the profile of the object. Two of the most promising FPP approaches are PDE profilometry and SSE profilometry.

1.2 Literature Review

1.2.1 Introduction

The literature review provides an overview of FPP approaches, including PDE and SSE. In this section, the fundamentals of FPP approaches are first introduced. A review of the existing PDE approaches is then given, especially Fourier transform profilometry and phase shifting profilometry. The phase unwrapping problem is also introduced. Finally, the SSE approaches are introduced.

1.2.2 FPP based on DFP

FPP is based on the triangulation principle, which is described as follows. Without loss of generality and for simplicity in expression, we assume that the projector has a fringe structure where the light intensity varies periodically along the x direction, while keeping constant along the y direction, as shown in Figure 1.1. $s(x)$ and $d(x)$ denote the variance in the light intensity of the fringe pattern on the reference plane and the object surface respectively, and $h(x)$ denotes the height distribution along the

x-axis. We also assume that the reference plane and the object's surface have the same reflective characteristics.

Let us consider what happens when a beam of light is projected onto point D on the object. From Figure 1.1, we can see that when the object is removed, the same light beam (with the same intensity) should be projected onto point H on the reference surface and then reflected back to the camera through point C. Because the triangles E_cE_PH and CDH are similar, we have the following relationship:

$$\frac{d_0}{l_0} = \frac{\overline{CD}}{h(x_d)} \tag{1.1}$$

where x_d denotes the coordination positions of point D. $h(x_d)$ denotes the distance between point C and the reference plane that is given by:

$$h(x_d) = \frac{l_0 \overline{CD}}{d_0} \tag{1.2}$$

The above relationship gives the foundation for FPP.

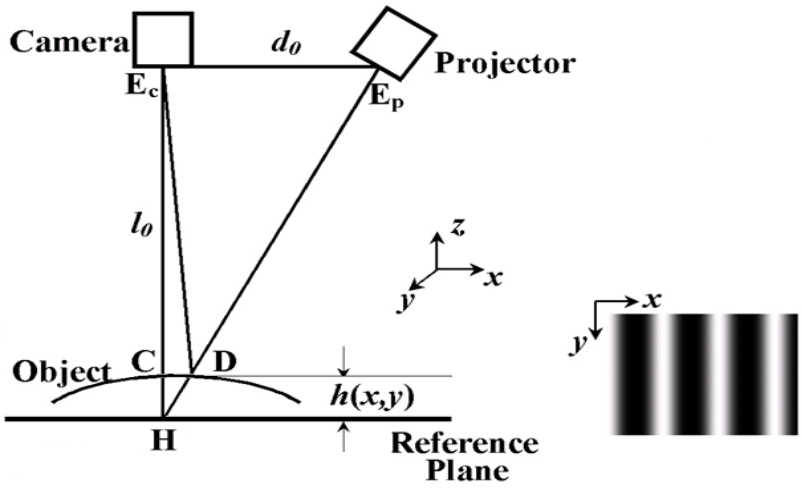

Figure 1.1 Schematic diagram of a DFP system

1.2.3 PDE Profilometry

A number of FPP approaches have been introduced. The most widely used one are the PDE profilometry in which the deformed fringe pattern is considered to be the result of phase modulation of the original fringe pattern. Detection of phase maps from the original fringe patterns and the deformed fringe patterns enables the retrieval of the 3D shape.

In detail, these approaches use fringe patterns that are periodic and can be expressed as [26, 27]:

$$s(x) = \sum_{k=0}^{+\infty} b_k \cos(2\pi k f_0 x + \psi_k) \tag{1.3}$$

and the deformed fringe pattern can be expressed as:

$$d(x) = \sum_{k=0}^{+\infty} b_k \cos(2\pi k f_0 x + \phi_k(x) + \psi_k) \tag{1.4}$$

In Equations (1.3) and (1.4), f_0 is the spatial frequency of the fundamental component in the fringe patterns, b_k is the amplitude of the *k*-th order harmonic component, ψ_k is the initial phase of the *k*-th order harmonic component and $\phi_k(x)$ denotes the phase difference between the *k*-th order harmonic components of the two fringe patterns.

Equations (1.3) and (1.4) show that $s(x)$ and $d(x)$ are related by the phase shift $\phi_k(x)$. Let us consider the light beam projected onto point D on the object and onto point H on the reference plane when the object is removed. The phase shift between C and D can be determined by the spatial distance $\overline{CD}$, and we have [26, 27]:

$$\phi_k(x_d) = 2\pi k f_0 \overline{CD} = k \cdot 2\pi f_0 \overline{CD} = k \cdot \phi(x_d) \tag{1.5}$$

where $\phi(x_d) = 2\pi f_0 \overline{CD}$ is the phase shift of the fundamental component.

Substituting Equation (1.5) into Equation (1.2) we have:

$$h(x_d) = \frac{l_0 \phi(x_d)}{2\pi f_0 d_0} \tag{1.6}$$

Because points D and H are arbitrary, the above derivations should apply to all points on the projected fringe pattern. Therefore, we have:

$$h(x) = \frac{l_0 \phi(x)}{2\pi f_0 d_0} \tag{1.7}$$

Equation (1.7) shows that as long as $\phi(x)$ can be detected, we are able to calculate the height distribution $h(x)$ of the object's surface. This is the foundation of all PDE-based approaches.

A number of fringe pattern analysis methods have been developed, such as Fourier transform profilometry [28], phase shifting profilometry [29 - 32], spatial phase detection [33, 34], phase lock loop profilometry [35], moiré technique [36], laser triangulation measurement [37], colour-coded fringe projection [38 - 41] and other methods [42, 43]. Of these fringe pattern analysis methods, two of the most popular and typical algorithms for FPP are Fourier transform profilometry and phase shifting profilometry [25].

1.2.3.1 Fourier Transform Profilometry (FTP)

FTP was first introduced by Takeda *et al*. [26, 27] in 1982. The concept underlying this approach is analysing the fringe image using the Fourier transformation.

From Equations (1.3) and (1.4) we know that $s(x)$ and $d(x)$ are composed of harmonic components. From Equation (1.7), we can see that the height distribution function $h(x)$ is only associated with the fundamental component of the phase difference.

The first step in the FTP approach is applying the Fourier transform to the fringe image. A filter is then used to remove all signals except for the fundamental components in the spatial frequency domain. Finally, an inverse Fourier transform is applied to this filtered signal.

After application of the inverse Fourier transform, we have $\tilde{s}(x)$ and $\tilde{d}(x)$, which are the fundamental components of $s(x)$ and $d(x)$ and can be expressed as:

$$\tilde{s}(x) = b_1 \cos(2\pi f_0 x + \psi_1) \tag{1.8}$$

$$\tilde{d}(x) = b_1 \cos[2\pi f_0 x + \phi(x) + \psi_1] \tag{1.9}$$

We use $\tilde{S}(x)$ and $\tilde{D}(x)$ to denote the complex signals of $\tilde{s}(x)$ and $\tilde{d}(x)$ respectively. We can then retrieve the phase difference $\phi(x)$ by using the following equation:

$$\phi(x) = unwrap(\mathrm{Im}\{\ln[\tilde{D}(x) \cdot \tilde{S}^*(x)]\}) \tag{1.10}$$

where $\ln(\cdot)$ is the natural logarithm function, $\mathrm{Im}(\cdot)$ denotes the operation to get the imaginary part of a complex number, $\tilde{S}^*(x)$ is the complex conjugate of $\tilde{S}(x)$ and $unwrap(\cdot)$ is the so-called phase unwrapping operation. In conventional PDE, the

retrieved phase difference $\phi(x)$ is restricted to principal values ranging between $-\pi$ and π. Therefore, the estimated phase is a modulo 2π distribution, but the true phase difference can be arbitrary and a wrapping problem occurs. The phase unwrapping operation is used to solve the wrapping problem in PDE. The details of the phase unwrapping problem will be discussed in Section 1.2.4. Figure 1.2 gives the flowchart of FTP.

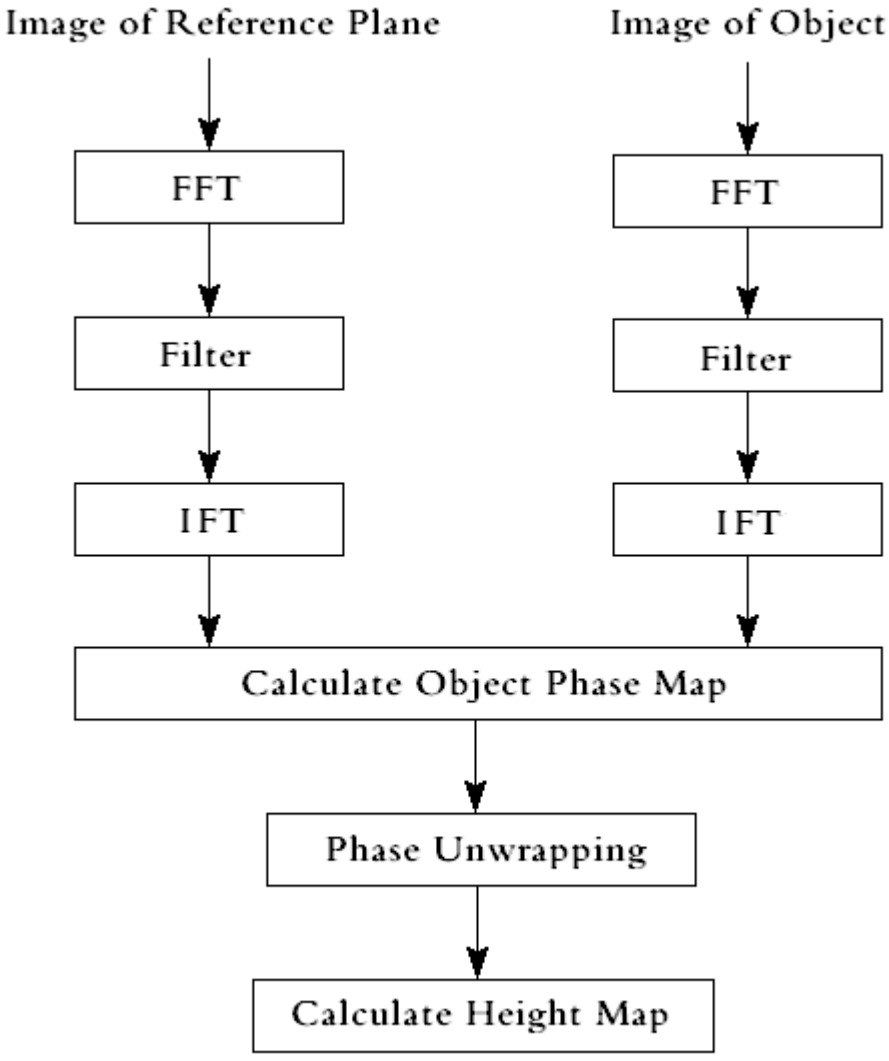

Figure 1.2 Flowchart of Fourier transform profilometry processing

1.2.3.2 Phase Shifting Profilometry (PSP)

PSP was first introduced by Toyooka and Tominga [33]. In this approach, multiple (at least three) frames of sinusoidal fringe patterns are projected onto the object's surface, and each frame is shifted by a certain amount of phase angle. The basic concept of PSP is as follows. The first acquired image is sampled with the fringe pattern projected at a given position. Then each fringe pattern is shifted $2\pi/N$ from the previous frame of the patterns, where N is the number of phase shifting steps. The fringe patterns on the reference plane and the object surface can be respectively expressed as:

$$s_n(x) = \sum_{k=0}^{+\infty} b_k \cos(2\pi k f_0 x + \psi_k + k\frac{2\pi n}{N}) \tag{1.11}$$

$$d_n(x) = \sum_{k=0}^{+\infty} b_k \cos[2\pi k f_0 x + k\phi(x) + \psi_k + k\frac{2\pi n}{N}] \tag{1.12}$$

for $n = 0, 1, 2, \ldots, N-1$.

Then the phase map $\phi(x)$ can be obtained by:

$$\phi(x) = unwrap(\arctan D_N) - unwrap(\arctan S_N) \tag{1.13}$$

where

$$S_N = -\left[\frac{\sum_{n=0}^{N-1} s_n(x)\sin(2\pi n/N)}{\sum_{n=0}^{N-1} s_n(x)\cos(2\pi n/N)}\right] \tag{1.14}$$

$$D_N = -\left[\frac{\sum_{n=0}^{N-1} d_n(x)\sin(2\pi n/N)}{\sum_{n=0}^{N-1} d_n(x)\cos(2\pi n/N)}\right] \tag{1.15}$$

Therefore, the height distribution function $h(x)$ can also be retrieved using Equation (1.7). Figure 1.3 shows the flowchart of PSP.

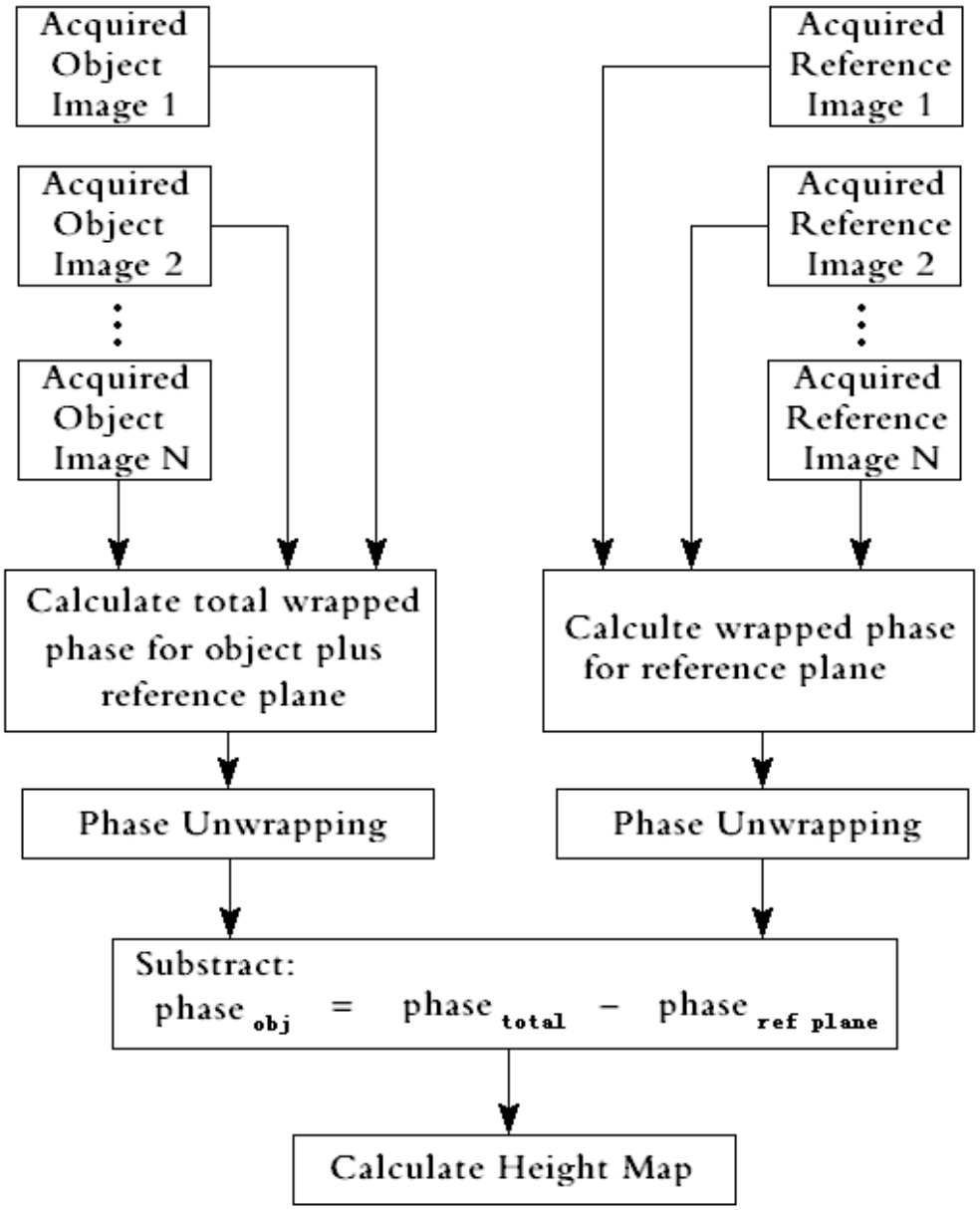

Figure 1.3 Flowchart of phase shifting profilometry processing

Compared with FTP, PSP has higher measurement accuracy, because the use multiple frames of images can eliminate the influence of noise in the fringe patterns. However, at least three images are needed for PSP, leading to the increase of time for 3D measurement.

1.2.4 Phase Unwrapping

With most phase detection method, such as FTP and PSP, the phase can only be detected within the main value range of $[-\pi, \pi]$, which is the wrapped version of the absolute phase. In order to retrieve the actual surface shape of the object, absolute phase maps [44, 45] must be used in Equation (1.7), which are usually continuous and monotonic with respect to x. The absolute phase maps can be recovered from the wrapped ones by phase unwrapping algorithms.

A number of methods have been proposed to solve the phase unwrapping problem. For the phase map associated with a single fringe pattern, quality-guided methods can be utilised, which carry out phase unwrapping by comparing the wrapped phase at neighbouring pixels and adding or subtracting multiples of 2π. A quality map is used to guide the phase unwrapping path, and several methods have been proposed to generate the quality map [46 - 53]. The unwrapping process starts from the highest quality point and continues to the lower quality points until it finishes.

Although quality-guided methods work well for a continuous phase map, they are not able to unwrap phase maps obtained from the object surface with steps or isolated parts. To overcome this problem, a two-wavelength phase shifting algorithm was proposed [9, 54 - 56]. In this algorithm, the measurable step height can be increased by setting the equivalent wavelength longer than any of the two wavelengths. However, this two-wavelength algorithm increases the measurable height step by sacrificing data quality, as the signal-to-noise ratio is smaller than that obtained using only a single-wavelength phase shifting algorithm. In order to futher increase the measurable height step with lower noise, multiple-wavelength phase shifting algorithms have been developed [11, 57 - 64]. Huntley and Saldner [65 - 67] proposed an approach called the temporal phase unwrapping algorithm, in which multiple fringe patterns with different frequencies were projected, yielding a sequence of wrapped phase maps, which are combined together to yield the unwrapped phase maps.

Zhang [68, 69] introduced a multiple-wavelength phase unwrapping algorithm. In this method, an image with only a single fringe that covers the whole measurement area is first projected, followed by a series of fringe images each with a wavelength decreased by a factor from the previous wavelength. Because the first image only contains one fringe, the unwrapping step is not required. The phase of the second image can be unwrapped by referring to the first image. After the phase of the second image is obtained, it can be used to correct the third image. The advantage of this method is that measurement noise is close to the one obtained using a single-wavelength phase shifting technique with the shortest wavelength. However, the number of image patterns required for this method is still an issue.

A reduction in the number of image patterns required while keeping an anti-noise capability is still a challenging problem. Recently, Ding, *et al*. [70, 71] developed an approach to recover the absolute phase maps of two image patterns with selected frequencies. In this method, only two image patterns with selected frequencies are needed, greatly reducing the number of image patterns needed. However, the method still has the restriction that the two selected frequencies for the image patterns must be coprime. To meet this requirement, the total number of pixels perpendicular to the fringe must be an integer multiple of the number of pixels within a fringe. This may not be possible in some cases.

1.2.5 SSE Profilometry

The PDE-based FFP methods suffer from some limitations. In particular, the fringe pattern must be periodic so that the phase maps of $s(x)$ and $d(x)$ exist and can be detected. However, due to many undesired factors inherent in digital projection, such as geometric distortion and nonlinear intensity distortion, the fringe patterns are hard to be pure sinusoidal [72]. To overcome nonlinear distortion, a number of methods have been proposed [73 - 82]. In an effort to combat the distortion problem, Hu, *et al*. [83 -

85] proposed a profilometry approach that is based on the estimation of the spatial shift for corresponding pixels on the two fringe patterns instead of detecting the differences between the phase maps. This approach is referred to as the SSE profilometry approach [83 - 85].

1.2.5.1 SSE

The idea underlying the SSE profilometry approach is rather simple and straightforward. Let us again consider $\overline{CD}$, the distance between C and D, which is obviously a function of the location of D (i.e., x_d), the location of H (or C, i.e., x_c) and the height of the object at point H (i.e., $h(x_d)$). Therefore, we have the following:

$$\frac{d_0}{l_0} = \frac{u(x_d)}{h(x_d)} \tag{1.16}$$

where $u(x_d) = \overline{CD} = x_c - x_d$, which is the spatial distance between x_d and x_c. Note that x_d and x_c are the points on $d(x)$ and $s(x)$ with the same light intensity, that is, $d(x_d) = s(x_c)$. Because the above derivation is valid for any x_d and x_c, we can replace x_d with x, yielding the following:

$$h(x) = \frac{l_0 u(x)}{d_0} \tag{1.17}$$

Note that $u(x)$ is the spatial distance between a point x on $d(x)$ and the corresponding point on $d(x)$ with the same light intensity, that is:

$$d(x) = s(x - u(x)) \tag{1.18}$$

Equations (1.17) and (1.18) provide a straightforward way to obtain the 3D profile of the object's surface. With $d(x)$ and $s(x)$ available, if we are able to calculate $u(x)$ to satisfy Equation (1.18), then we can use Equation (1.17) to yield $h(x)$, which is the height distribution of the object surface along *x*. By repeating the procedure for all *y*, we are able to obtain the 3D profile of the object's surface.

The SSE-based approach has a particular advantage because the projected fringe patterns are no longer required to be sinusoidal. This implies that, even if there are distortions in the fringe patterns, sufficient 3D information about the object's surface is contained in the variation between the projected fronge patterns and the deformed fringe patterns. Thus the profilometry can be achieved.

1.2.5.2 Direct Shift Estimation Algorithm

As discussed above, the key to reconstructing an object's surface using SSE is to obtain the shift distribution $u(x)$ from $d(x)$ and $s(x)$. Based on the curve-fitting technique, Hu, *et al*. [86] introduced a direct shift estimation method called the inverse function-based shift estimation (IFSE) method. The idea underlying this method is the use of the inverse function.

Suppose that the projected signal function $r = s(x)$ is a monotonic function, or that it is monotonic in intervals of *x*, in which $s(x)$ has a unique inverse function $s^{-1}(r)$, where:

$$s^{-1}(r) = x \tag{1.19}$$

Applying this inverse function $s^{-1}(r)$ to the deformed signal $d(x)$, we have:

$$s^{-1}(d(x)) = s^{-1}\{s[x-u(x)]\} = x-u(x) \tag{1.20}$$

and the shift distribution function $u(x)$ can be retrieved by:

$$u(x) = x - s^{-1}(d(x)) \tag{1.21}$$

Using Equation (1.21), the shift distribution function $u(x)$ can be easily calculated through the fringe patterns on the reference plane and object surface. The key problem now is to obtain the inverse function $s^{-1}(r)$. To solve this problem, Hu, *et al*. [86] introduced a method that uses polynomial curve fitting. However, errors will be consequentially introduced using this method and are defined as the curve fitting error e_f, which is evaluated by the mean square error:

$$e_f = E[(y_f(x) - y(x))^2] \tag{1.22}$$

where $E(w)$ denotes the operation to calculate the mean value of w, $y_f(x)$ is the values of the curve fitting results calculated by the approximate polynomial and $y(x)$ is the data to be fitted.

To reduce the curve fitting error, one solution is to increase the degree of polynomial for fitting. However, if the degree selected is too high, it will result in heavy computation complexity. So we need to set up an upper bound for the fitting error e_f, and then calculate the minimum degree of polynomial that makes e_f less than the bound we have set. The procedure can be described as follows:

Step 1: Set e_m, which is an upper bound for the curve fitting error, and *k*, which is the degree of polynomial used for curve fitting. We initialise the starting value of *k* equals to 1.

Step 2: Work out j_k, which is the polynomial of degree *k* to approximate the inverse function $s^{-1}(r)$ in the least squares sense. In this step, we first obtain a symmetrical curve of $s(x)$ in each monotonic interval by using the straight line $x = r$ as a symmetry axis. Because this curve is the inverse function $s^{-1}(r)$, we can calculate the curve fitting result j_k by making the curve fit to the obtained symmetrical curve.

Step 3: Calculate the curve fitting error e_f using Equation (1.22), where $y_f(x)$ is approximated by using the curve fitting result j_k. If $e_f \le e_m$, go to Step 4, otherwise $k = k + 1$ and return Step 2.

Step 4: Using the curve fitting result $s^{-1}(r) \approx j_k$ and the value of deformed signal $d(x)$, calculate the shift distribution function $u(x)$ using Equation (1.21).

Note that it has been proven that j_k, which satisfies $E[(j_k(r) - s^{-1}(r))^2] < e_m$, always exists [87].

Figure 1.4 shows the flowchart of IFSE processing. As with Fourier transform profilometry and phase shifting profilometry, an unwrapping operation is needed before we can retrieve the height information. However, one thing that should be noted is that unlike Fourier transform profilometry and phase shifting profilometry, *unwrap*(·) is not a phase unwrapping operation but a new operation that is referred as shift unwrapping. This unwrapping is based on shift estimation and will be discussed in Chapter 3.

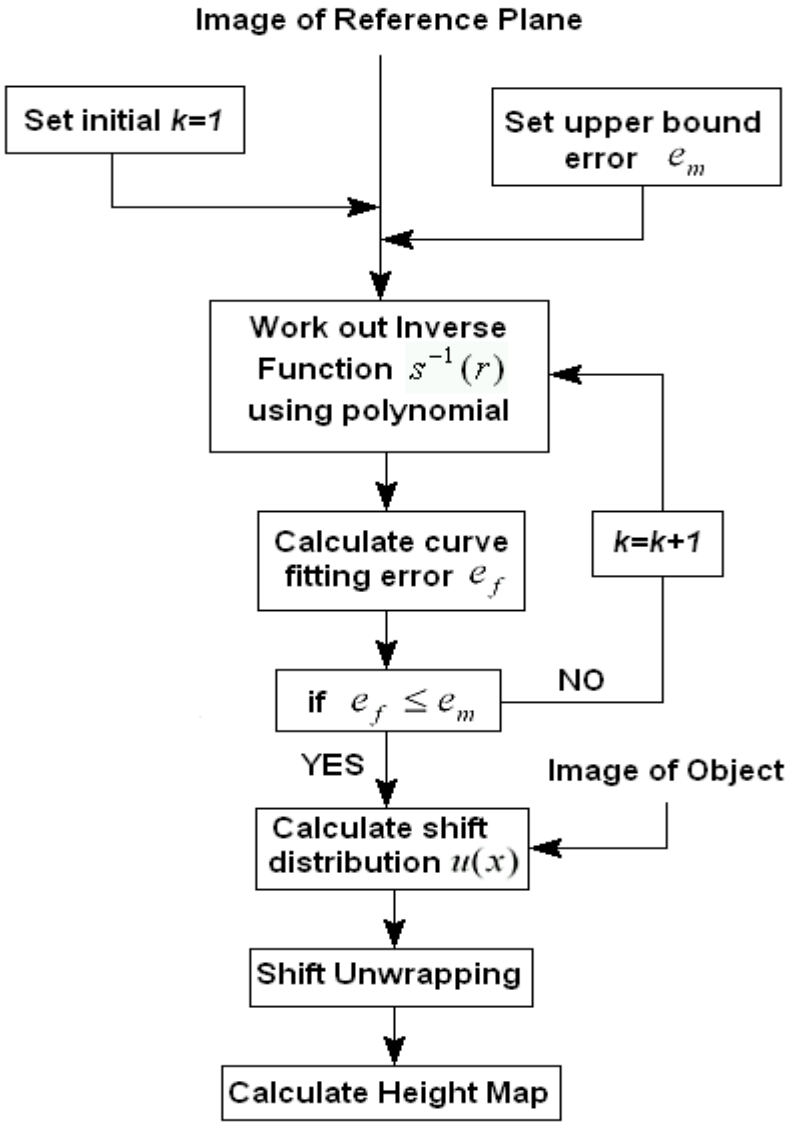

Figure 1.4 Flowchart of IFSE processing

The IFSE Method has two advantages. Firstly, because the curve fitting method is used to obtain the inverse function, the structure of the projected fringe pattern is no longer required to be sinusoidal. Secondly, because this method is directly based on the projected fringe patterns, it can be used even when the reference plane has been distorted by unknown effects.

1.3 Existing Issues

Let us now look at the existing research work in the area of the implementation of the SSE approach. Through evaluating the strengths, weakness and the gaps of other researchers' work, the following issues have been identified.

- **Implementation of SSE approach**

Although SSE-based FPP has been considered to be a promising approach in the area of 3D profilometry, few practical systems have been demonstrated to implement this approach. Problems associated with the implementation still exist. Therefore, to study the performance of the SSE approach and to develop solutions to these problems, the implementation of the SSE approach based on a DFP system is needed.

- **The efficiency of the SSE approach**

In most cases, the projected fringe pattern is selected to be sinusoidal. However, the use of a sinusoidal fringe pattern has many limitations, such as the vulnerability to geometric and nonlinear intensity distortion. To solve the problems, an additional filter is needed, which increases the computation complexity. A sinusoidal fringe pattern is not suitable for the IFSE method in SSE because of its long computation time. Hence, improvement is needed to increase efficiency. Because the SSE approach has the advantage that the projected fringe patterns are not required being sinusoidal or periodic, it is important to design a fringe pattern that has a strong counter-interference capability against the distortions and a short computation time for IFSE method.

- **Shift unwrapping in SSE approach**

For PDE-based approaches, the phase difference can only be detected within the main value range of $[-\pi, \pi]$, but the true phase difference can be arbitrary, which means that a wrapping problem exists. To retrieve the actual surface shape of the object, phase unwrapping must be carried out to obtain the actual phase maps. Many methods have

been proposed to solve this wrapping problem in the PDE approach. In the SSE-based approaches, the spatial shift between corresponding pixels on the two fringe patterns can also be arbitrary, but it only can be detected without ambiguity within the range of [0, λ], where λ is the width of the individual fringe. Obviously, shift unwrapping is also required in retrieve the 3D shape of the object surface correctly. Spatial shift unwrapping for SSE-based FPP is still an outstanding issue, which motivates the work presented in this thesis.

1.4 Aim of the Thesis Work

This thesis aims to solve the following research issues associated with DFP systems:

- Design a DFP system, including hardware settings and software program design. Then implement the SSE approach using this system.
- Increase the efficiency. The usage of sinusoidal fringe pattern in SSE approach suffers many limitations and all those results the long time in computation. Hence to find a solution to reduce the computation time and improve the efficiency is also important.
- Develop solutions for the unwrapping problem in the SSE approach. The unwrapping problem is a major impediment to retrieving height distribution information. Many methods have been proposed to solve the unwrapping problem in PDE approach. But these approaches are not able to solve the unwrapping problem in SSE approach.

1.5 Contribution of the Thesis Work

In this thesis, the following contributions are made:

- **A DFP system to implement the SSE approach**

A DFP system model based on the principle of FPP is proposed. This system consists of two sub-systems: projection and acquisition. A software interface is designed to control this system. The performance of the SSE approach is then evaluated by implementation using this system. Solutions to the problems associated with implementation are also developed.

- **Use of new fringe pattern to improve the efficiency**

In traditional FPP, the sinusoidal fringe pattern is selected as the projected fringe pattern. However, the use of sinusoidal fringe patterns has several limitations, such as vulnerability to nonlinear intensity distortion and being unsuitable for use with the IFSE method. These limitations decrease the efficiency by introducing additional computations. In the SSE approach, the projected fringe patterns are no longer required to be sinusoidal. However, in existing works on SSE, sinusoidal fringe patterns are still employed. Therefore, a new IFSE method which used a new fringe pattern, the triangular fringe is developed in this thesis. The advantages of the triangular fringe through several rules are analysed and compared with the sinusoidal fringe pattern in theory. An experiment is then performed. Detailed experimental data is presented to prove the improvement in efficiency resulting from the proposed method using this new fringe pattern against the existing method.

- **A solution to the unwrapping problem in SSE approach**

The unwrapping problem is a key problem in FPP. It causes the discontinuity in retrieving height information. After theoretical analysis, it is indicated that, in the SSE approach as well as the conventional PDE approach, the unwrapping problem exists and prevents us from retrieving the correct height information. Therefore, this problem must be solved. There are many methods are proposed to solve the unwrapping problem in PDE approach, however, while spatial shift estimation (SSE) based profilometry was proposed a few years ago, there is not such a work devoted to unwrap

the spatial shift map for complex objects. Hence based on the theory of phase unwrapping methods, several spatial shift unwrapping methods are introduced to solve the unwrapping problem in the SSE approach in this thesis. Experiments are also carried out to test their performances. Results are given to evaluate the effectiveness of the proposed unwrapping techniques and successful proven the work presented is novel and helpful in both theory and practice.

1.6 Organisation of the Thesis

The remainder of this thesis is organised as follows. Chapter 2 first describes the procedure to implement the SSE approach using a DFP system, which includes an illustration of a DFP system model and the implementation of SSE approach. Shortcomings and limitations associated with the use of sinusoidal fringe patterns are then discussed. To overcome these problems, a triangular fringe pattern is introduced instead of sinusoidal fringe pattern based on theoretical analysis. Experimental results are then presented to verify the effectiveness and advantages of the triangular fringe pattern. Chapter 3 introduces the spatial shift unwrapping problem and a solution based on a traditional reliability-guided phase unwrapping method is presented. Chapter 3 also introduces a multiple-wavelength unwrapping algorithm for the SSE approach, which is based on the multiple-wavelength phase unwrapping algorithm introduced by Zhang [69]. Experimental results are then given to demonstrate that the proposed method can be used to measure complex objects with significant step height or multiple separate objects using the SSE approach. Chapter 4 introduces a method for unwrapping spatial shift maps of two fringe patterns with different frequencies. An improved method with flexible selection of fringe wavelengths is then proposed. Based on this method, a novel 3D shape measurement approach is given. A set of experimental results are then presented to demonstrate performance of the proposed method. Chapter 5 concludes this thesis.

Chapter 2 Implemention of the SSE Approach

2.1 Introduction

In this chapter, the implementation of the SSE approach is described, including the system design and the procedure for implementation as well as problems encountered and their solutions.

In conventional PDE, the projected fringe pattern is required to be sinusoidal because the height distribution is retrieved from the phase map of the projected and deformed fringes. That means that the phase maps of $s(x)$ and $d(x)$ must exist and can be detected. However, the use of sinusoidal fringe patterns has the limitation that pure sinusoidal fringe patterns cannot be obtained in practice due to the many undesired factors inherent in digital projection. One major problem is the nonlinear projection luminous response, which is referred to as gamma distortion. Because the SSE approach retrieves the height distribution by directly estimating the spatial shift, it has the advantage that the projected fringe patterns are not required to be either sinusoidal or periodic. Thus, we can design a fringe that has strong counter-interference capability against nonlinear distortion.

This chapter is organised as follows. Section 2.2 presents the details of the hardware and software for the DFP system. The hardware section describes the configuration of the system, and the software section presents the design of software interface for generating and controlling the fringes. Section 2.3 elaborates on the implementation of the SSE approach, which includes pre-processing of captured image, IFSE and object reconstruction. Section 2.4 discusses the limitations of traditional sinusoidal fringe patterns. Section 2.5 presents a solution to these limitations that consists of design rules for fringe selection and a novel IFSE method that uses triangular fringe patterns instead of sinusoidal fringe patterns and is based on theoretic analysis. Section 2.6

carries out an experiment and uses the results to illustrate the advantages of the new triangular fringe patterns. Section 2.7 provides the conclusion to this chapter.

2.2 DFP System Model

2.2.1 System Structure

The hardware for the DFP-based 3D sensing arrangement used for the implementation is depicted in the schematic diagram in Figure 2.1.

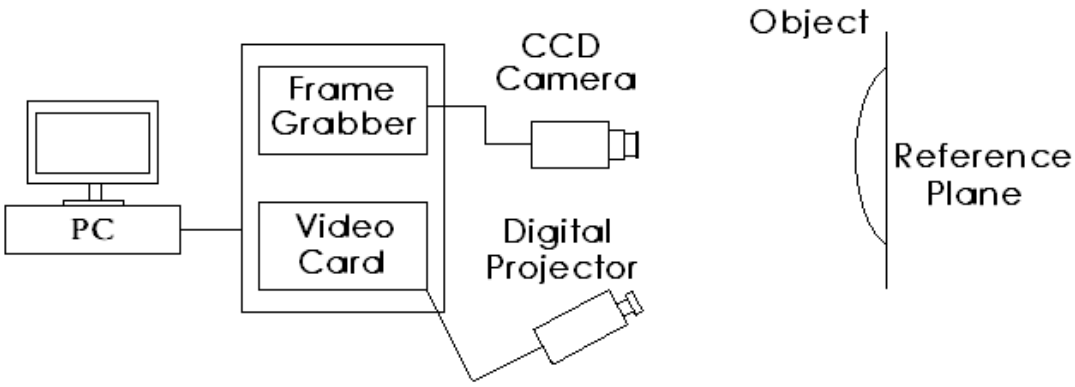

Figure 2.1 DFP arrangement

A personal computer is used to manage both the projector and camera via the video and frame-grabber cards respectively. This computer controls the projector and camera simultaneously and also processes the acquired data. The DFP system can be divided into two sub-systems: projection and acquisition.

Figure 2.2 shows a photo of the experimental set-up. The distance from the digital camera to the projector and the distance between the camera lens and the reference plane are adjustable. Hence the field of vision for the CCD camera can also be adjusted to adapt to different sized objects.

Figure 2.2 The experimental system set-up

2.2.1.1 Projection

In the projection sub-system, a digital projector is connected to the computer via a Matrox multiple head video card. The standard operating system display setting was then used to configure the projector as an independent display device. The Coloreal Visual software that accompanies the Matrox card allows precise calibration of each display output in terms of the display gamma, brightness and contrast for the individual colour channels. This facilitated the appropriate configuration of the display outputs.

The projector used in the system is a HITACHI CP-X260 3LCD projector [88]. The specification for the projector is given in Table 2.1.

Table 2.1 Projector specification

Specification	HITACHI CP-X260
Technology	1.6 cm Poly-Si 3-LCD
Native Resolution	1024 × 768
Contrast Ratio	500:1
Brightness (ANSL Lumens)	2500

2.2.1.2 Acquisition

The acquisition sub-system should be specifically selected to accommodate both single-channel and multi-channel environments. In the DFP system, a high resolution Duncan Tech MS3100 3-CCD camera was used for acquisition. This camera was connected to the personal computer via a National Instruments IMAQ-1428 frame grabber card. A dichroic prism was used in this camera, which contains three individual imaging channels with independent resolutions of 1392 × 1039 pixels at an 8 or 10 bit precision.

Specialised DTControl software developed by Duncan Tech is provided with this camera. This software allows the control of aspects of the device including individual channel gain, individual channel integration time and overall integration time, quantisation precision (8 or 10 bit) and triggering mode.

2.2.2 Software Interface

The software interface responsible for the integration of hardware components serves a distinct role: the generation and control of the fringes. In the DFP system, the software is written in MATLAB to produce the fringes in three colour channels: red, green and blue. Each channel is controlled by three parameters:

- Contrast: This parameter defines the amplitude of the sinusoidal fringe pattern. This is usually set at 1.0 as the default value.
- Phase: This parameter controls the phase offset of the sinusoidal fringe pattern. The default value is set to 0.
- Frequency: This value determines the frequency of the sinusoidal fringe pattern.

The flowchart of the fringe generate software is given in Figure 2.3. This software first generates three individual sinusoidal waveforms that are considered to be the

colour intensity information for the projected fringe. The three waveforms represent the red, green and blue fringes controlled by the parameters contrast, phase and frequency. These are then combined and the colour intensity information is transferred into a colour image.

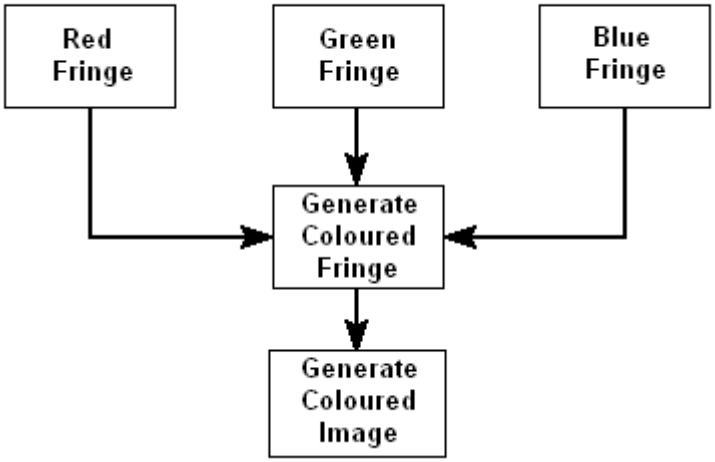

Figure 2.3 Flowchart of fringe generation

Figure 2.4 shows an example of the final colour fringe image. In this image, the contrast, phase and frequency are set at at the same value for the red, green and blue fringes. Hence, a black and white image is produced.

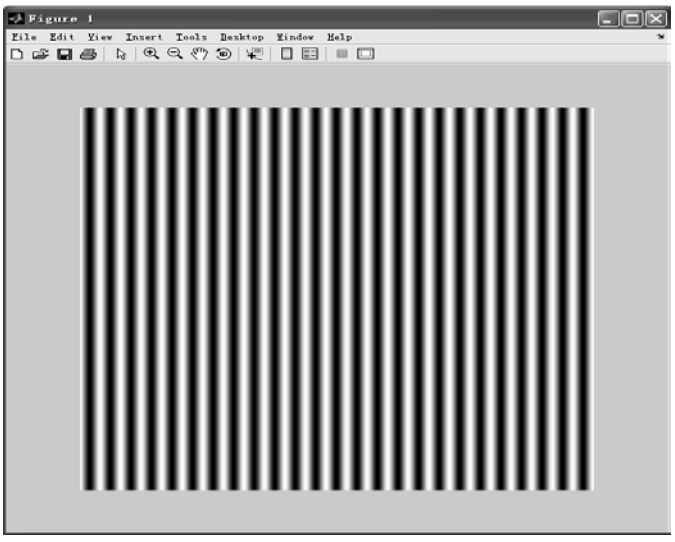

Figure 2.4 Fringe produced (contrast = 1.0, phase =0, frequency = 25)

2.3 Processing of the Images Captured

As discussed in Chapter 1, the SSE approach needs to acquire two images, one from the reference plane and one from the object surface. In the experiment, a dome set on a flat board was used as the object, with a maximum height of 22.8 mm. The diameter of the bottom surface of the dome is 99 mm, and the thickness of the base board is 16 mm.

Figure 2.5 shows two images, one from the reference plane and one from the object's surface. These images were captured using the following system set-up: The digital camera was placed on top of the projector with a distance of 350 mm. The distance between the camera lens and the reference plane was 1295 mm. The resolution of the CCD camera was 1392 × 1039 pixels, and the filed of vision of the camera was 250 mm × 187 mm. Hence, the equivalent spatial resolution was 0.1796 mm/pixel. Before measurement, camera calibration is performed to the fringe projection system, and the calibration method used is introduced in Hu, *et al*. [89].

It should be noticed that although the CCD camera supports the maximum capture range of 1392 × 1039 pixels, in order to get the best efficiency of measurement, the captured image resolution still should be selected depending on the objects to be measured. Using full resolution will result additional computation time, which will reduce the measurement speed. Hence the resolution of the captured images in Figure 2.5 is selected to 875 × 875 pixels.

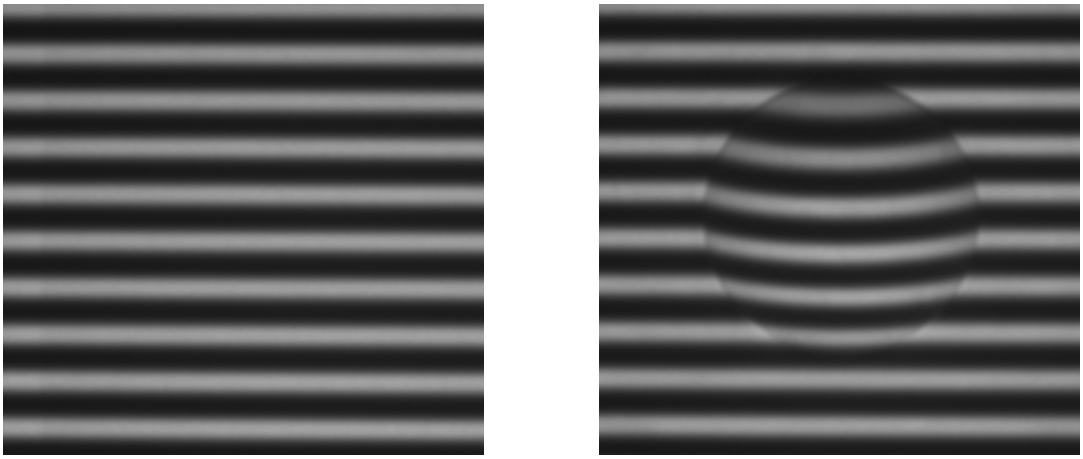

Figure 2.5 Captured image of reference plane (left) and object surface (right)

The SSE-based approach includes pre-processing the captured image, retrieving height information and reconstructing the object's surface.

2.3.1 Pre-processing of the Captured Image

The first step for image processing is retrieving the colour intensity information from the captured image. This can be easily performed using MATLAB. However, the captured images suffer from distortion and noise introduced by the equipment and the environment. Before the IFSE is applied, pre-processing is required to eliminate or reduce distortion and noise from the captured image.

The first problem is the noise. As discussed in Section 1.2.5.2, IFSE requires the retrieved signal function $r = s(x)$ to be a monotonic function, or to be monotonic in intervals of x. In theory, the fringe retrieved from the image of the reference plane should be an ideal sinusoidal, that is, monotonic in each half of its period. However, in practice, due to existence of noise, the monotonic requirement cannot be met. Thus it is impossible to apply the IFSE method. Figure 2.6 shows the acquired fringe data from the reference plane. For illustration purposes, one line from each of the captured images where $y1 = 750$ was selected, which is the middle of the dome object. From

Figure 2.6, we can see that the acquired signal in each half of its period is not monotonic due to the influence of noise.

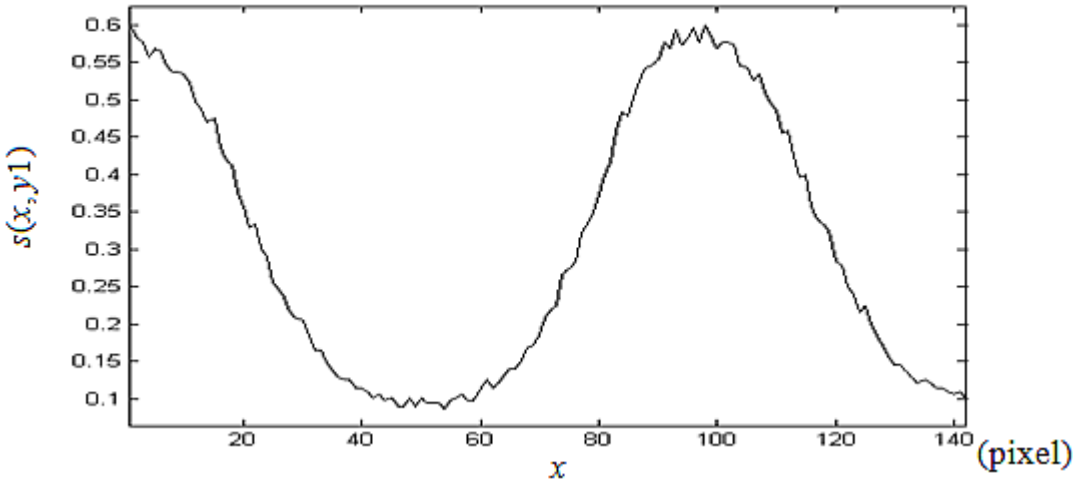

Figure 2.6 Acquired fringe data from reference plane

In addition to the noise, another problem also needs to be solved. Figure 2.7 shows the acquired fringe data from the reference plane and the object. Compared with the reference fringe, it is obvious that the fringe patterns from the object are severely distorted.

After analysis, we find that this distortion is caused by the colour and reflectivity of the object's surface. While the reference plane's surface has uniform colour and reflectivity, we cannot ensure that the object surface has the same colour and reflectivity. Therefore, the intensity distribution of the object surface is not uniform, causing distortion of fringe patterns as shown in Figure 2.7.

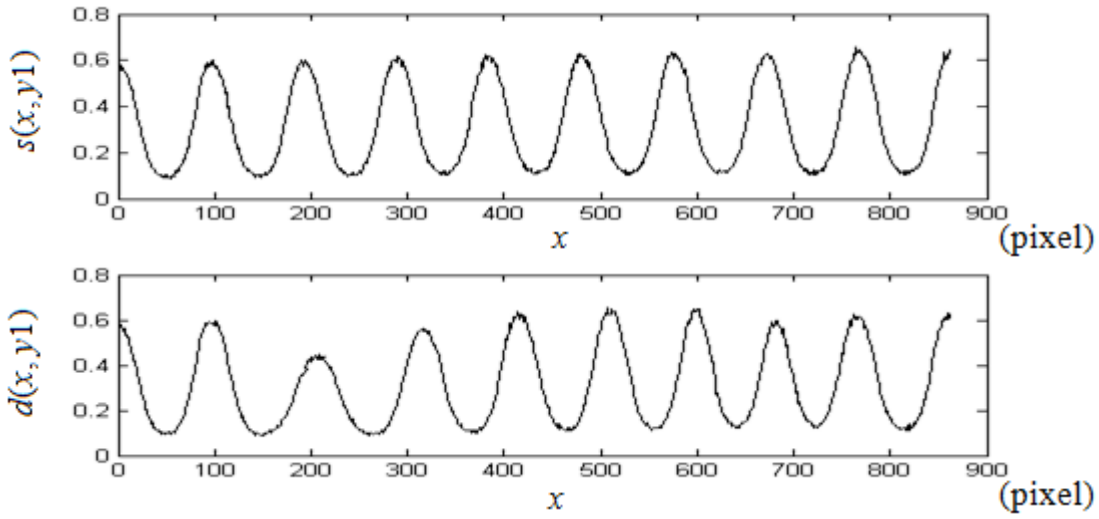

Figure 2.7 Acquired fringe data from captured image of the reference plane (top) and object (bottom)

With IFSE, the inverse function $s^{-1}(r)$ is obtained from the projected signal $s(x)$ which is then applied to the deformed signal $d(x)$; the shift distribution function $u(x)$ can then be retrieved using equation $u(x) = x - s^{-1}(d(x))$. However, this equation can only be used only when $s(x)$ and $d(x)$ have the same height range. Because the distortion changed the height range of the deformed signal $d(x)$, IFSE cannot be used until we eliminate the influence of distortion.

In the sections followed, a filter is first designed to reduce the noise and interferences, and then a method is proposed to solve the distortion problem.

2.3.1.1 Filter Design

The noise in the fringe patterns can be reduced by digital filters. From Figure 2.6, we can see that the frequency of noise higher than the fringe signal, and hence a low-pass filter can be used to attenuate the noise. However, the cut-off frequency must be

carefully selected. If the cut-off frequency is too low, the fringe signal will also be attenuated; if the cut-off frequency is too high, noise will remain.

Figure 2.7 also shows that the frequency of the deformed signal $d(x)$ is different from the frequency of the reference signal $s(x)$ due to the height information from the object's surface. The frequency of $d(x)$ is higher than the frequency of $s(x)$ when the slope of the object is negative. Therefore, the cut-off frequency should be chosen based on the frequency of the deformed signal to prevent the loss of height information. Figure 2.8 presents the frequency spectrum of the deformed signal $d(x)$ depicted in Figure 2.7, where the *x*-axis is normalised with 1.0 corresponding to half the sample rate, and the *y*-axis is the normalised frequency response.

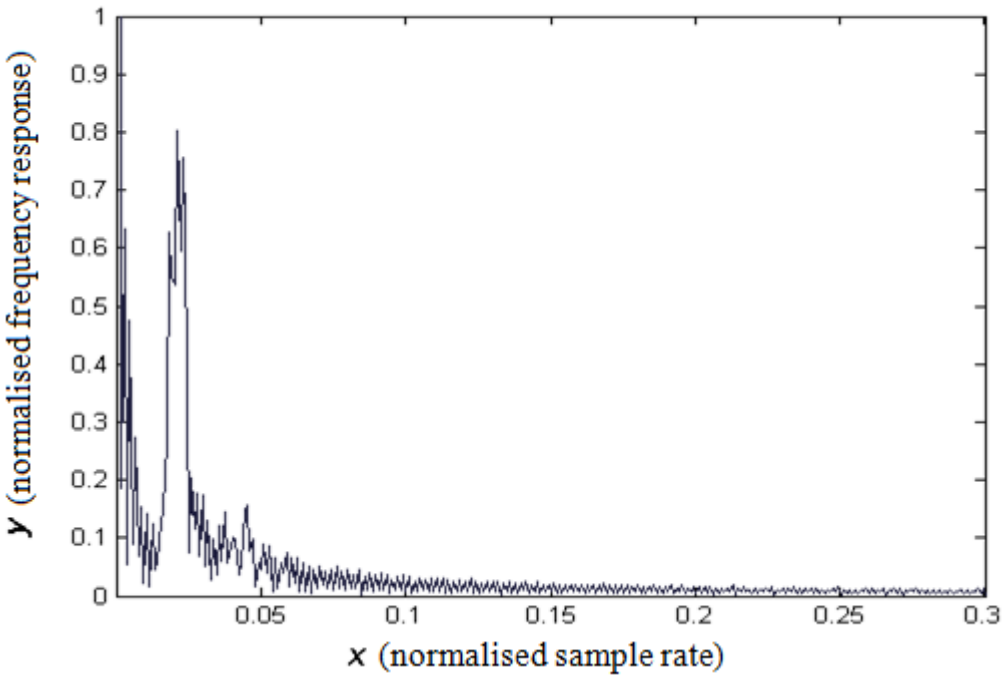

Figure 2.8 Frequency spectrum of the deformed signal

It can be seen from Figure 2.8 that when $x > 0.05$, the frequency response of the deformed signal falls below 0.1 and continues to decrease. It can be considered to be

the component of high-frequency noise signal, and to attenuate it, the cut-off frequency should be selected near $0.05\times(SampleRate/2)$.

In the experiment, a finite impulse response (FIR) digital filter is used. Figure 2.9 shows the frequency response of the filter. After calculation and experiment, the frequency breakpoints of this filter were set to $0.15\times(SampleRate/2)$. According to Figure 2.9, the cut-off frequency is the point where the frequency response at $\sqrt{1/2}$ is about $0.04688\times(SampleRate/2)$.

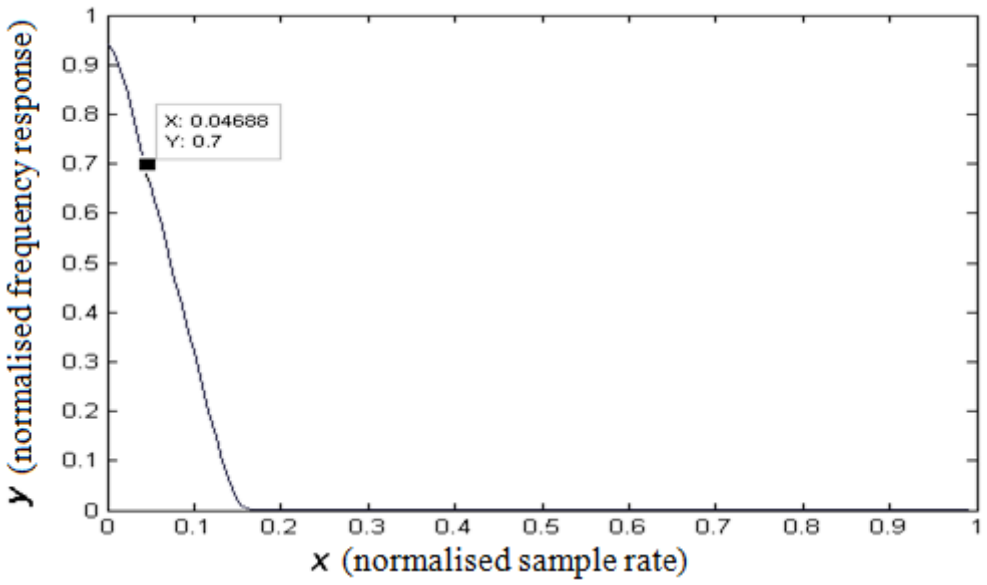

Figure 2.9 Frequency spectrum of designed filter

Figure 2.10 shows the fringe data after filtering, and we can see that the high-frequency noise has been successfully removed.

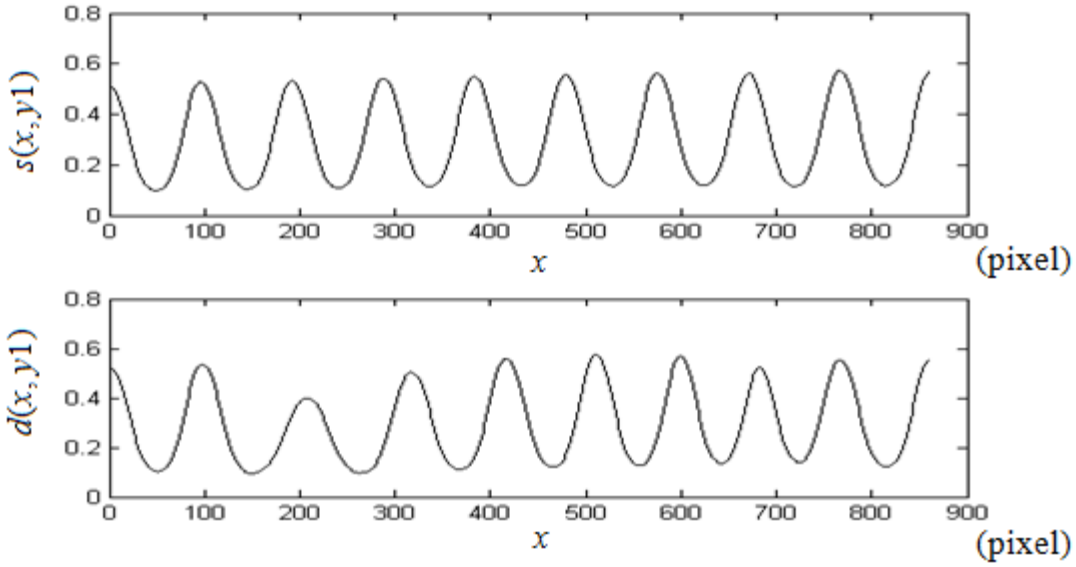

Figure 2.10 Acquired fringe data after filtering for the reference plane (top) and the object (bottom)

2.3.1.2 Normalisation of Fringe

The distortion of the deformed signal $d(x)$ is another problem that needs to be solved. As mentioned earlier, this problem is introduced by non-uniform reflectivity of object surface. As the intensity distortion does not influence the shift information, we only need to normalise the distortion in intensity to make IFSE available for use.

The procedure of fringe normalisation is very simple. First, we divide the projected signal $s(x)$ and deformed signal $d(x)$ into several monotonic intervals. As shown in Figure 2.11, we separate $s(x)$ into the monotonic intervals s_1, s_2, $s_3 \ldots$ and $d(x)$ is separated into d_1, d_2, $d_3 \cdots$ and so on.

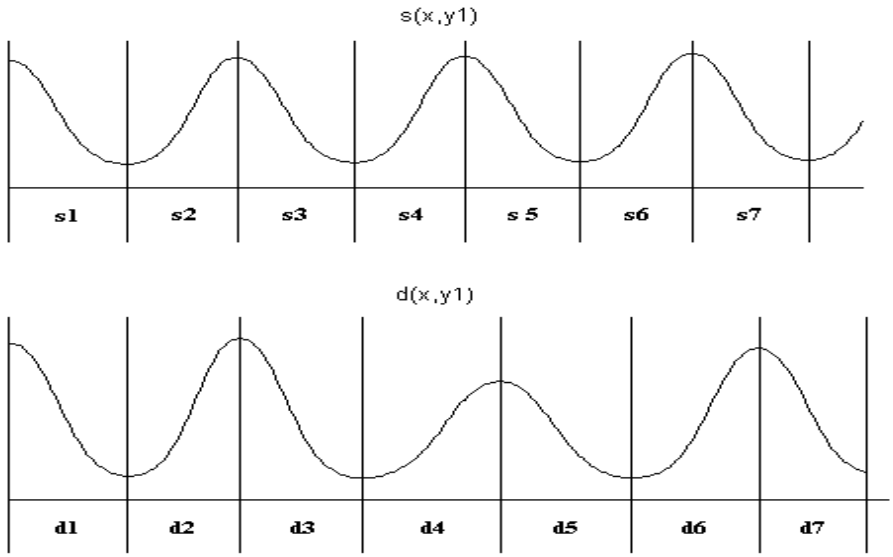

Figure 2.11 Fringe divided into monotonic intervals for the reference plane (top) and the object (bottom)

Then we can perform normalisation processing on each monotonic interval using the following steps (suppose the intervals we selected are s_1 and d_1):

Step 1: Calculate the middle value of the selected monotonic interval in the referenece signal $s(x)$ and the middle value of the corresponding monotonic interval in the deformed signal $d(x)$ using the following two equations:

$$s_1^{mid} = \frac{s_1^{\max} + s_1^{\min}}{2} \tag{2.1}$$

$$d_1^{mid} = \frac{d_1^{\max} + d_1^{\min}}{2} \tag{2.2}$$

where $s_1^{\max}$ and $d_1^{\max}$ are the maximum values in intervals s_1 and d_1 respectively, and $s_1^{\min}$ and $d_1^{\min}$ are the minimum values.

Step 2: Work out s_1^r and d_1^r, which are the height range of intervals s_1 and d_1, using the following equations:

$$s_1^r = s_1^{\max} - s_1^{\min} \tag{2.3}$$

$$d_1^r = d_1^{\max} - d_1^{\min} \tag{2.4}$$

Step 3: Normalise the height of d_1 using the follow equation:

$$d_1^{fix} = [(d_1 - d_1^{mid}) * (\frac{s_1^r}{d_1^r})] + s_1^{mid} \tag{2.5}$$

where d_1^{fix} is the normalised deformed fringe data.

The deformed fringe will be normalised after we perform these steps on each interval of $d(x)$. Figure 2.12 shows the normalised fringe data.

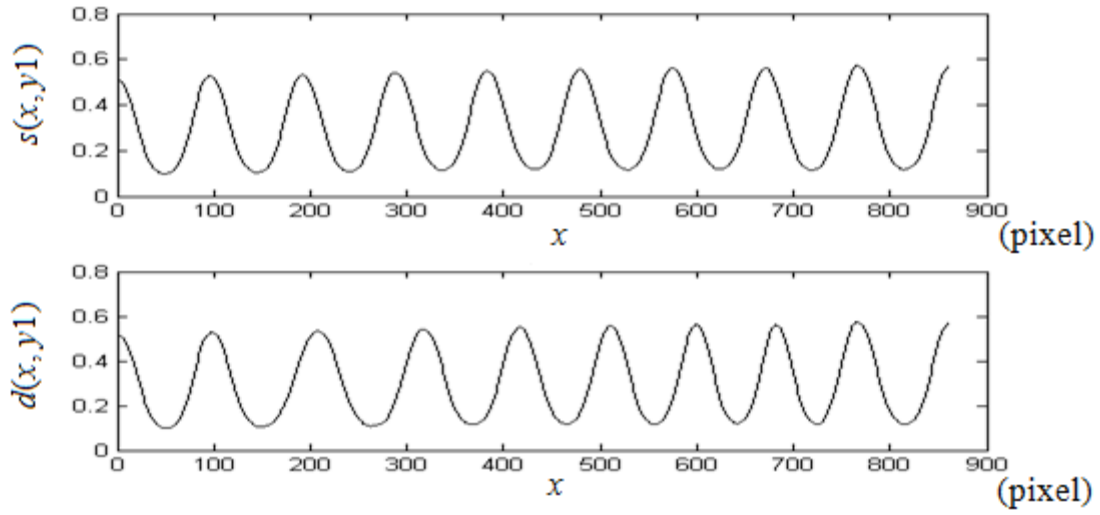

Figure 2.12 Normalised fringe data for the reference plane (top) and the object (bottom)

2.3.2 Improved IFSE

In SSE, we use the IFSE method to obtain the height information from the estimation of spatial shift. After the pre-processing on the acquired fringe data, all conditions for performing IFSE are satisfied. The procedure of IFSE is discussed in Chapter 1. However, during the implementation, problems still exist.

As described in Section 1.2.5.2, the first step of the IFSE method is setting an upper bound for the curve fitting error e_m, and then repeating the curving fitting step until the curve fitting error e_f is smaller than or equal to the bound. However, too much time will be consumed on calculation if the initial degree of polynomial used for curve fitting starts from 1.

One suggested solution is increasing the initial degree of polynomial used for curve fitting. We know that the reference fringe pattern is sinusoidal, it is a periodic pattern and, in theory, the curve fitting polynomial for each monotonic interval should be the same. However, in practice, there will be a slight difference between each interval due to noise and distortion. Therefore, we need to do curve fitting for each interval, but the degree of curve fitting polynomial can vary within a small range. We can set the starting value of *k* near this range or just give a fixed value of *k* that is selected from the range. This method will reduce the computation time because we only need to calculate the range for *k* one or two times instead of calculating it for every interval. Figure 2.13 shows the flow chart of this improved IFSE method.

Compared with Figure 1.4, Figure 2.13 has two changes. First, before we perform the IFSE processing, two pre-processing steps are added. Second, the initial value of *k* is not limited to be 1; higher initial values can be used to reduce the computation time. As shown in the flow chart, after unwrapping (the unwrapping method will be discussed in Chapter 3), we can retrieve the height distribution of the object.

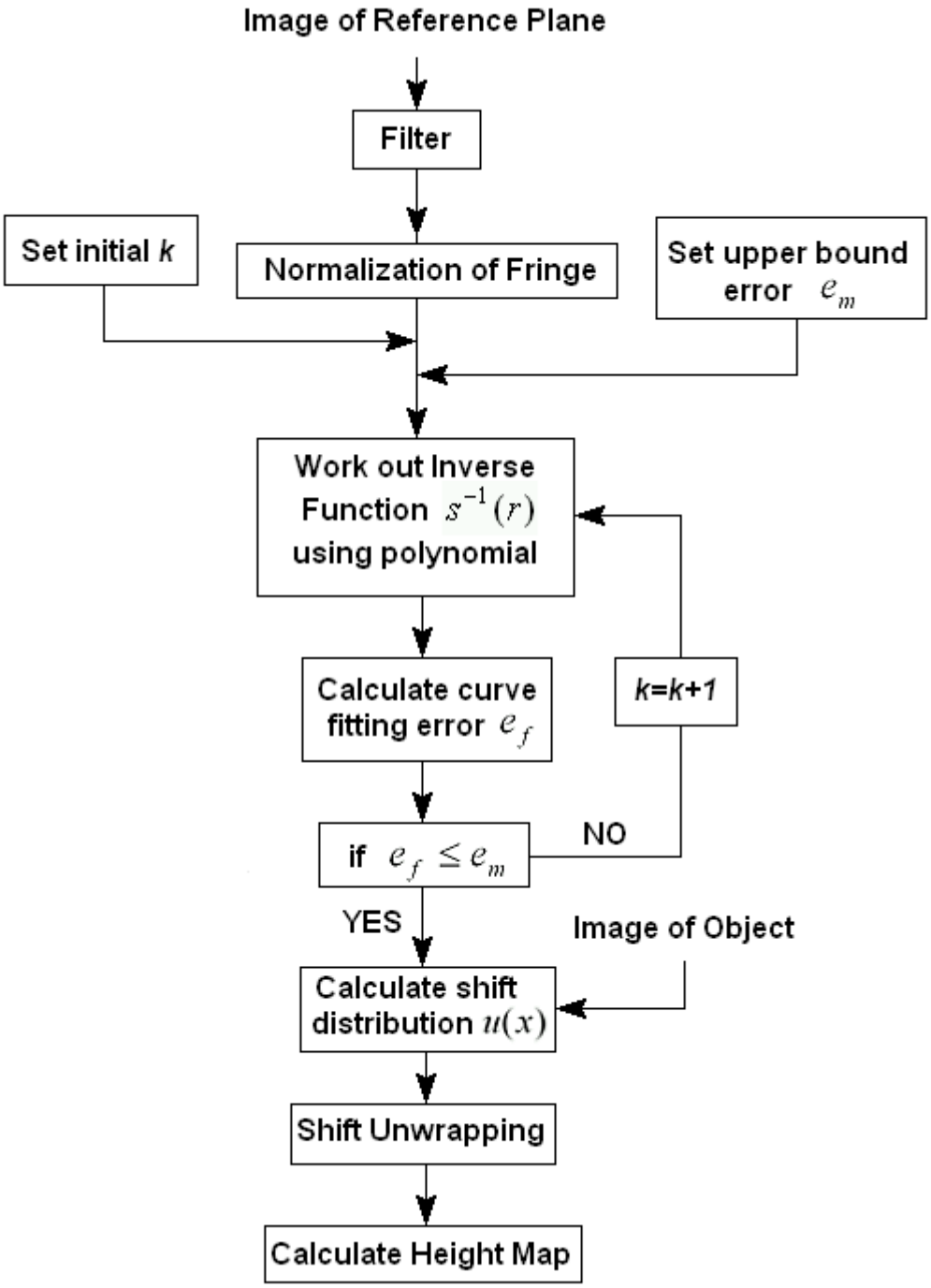

Figure 2.13 Flowchart of improved IFSE processing

2.3.3 Reconstruction of the Object's Surface

The final step of the implementation is the reconstruction of the object's surface. Using the improved IFSE method discussed above, we can retrieve the height distribution. We use MATLAB to reconstruct the 3D model of object's surface. Figure 2.14 shows the final reconstructed object surface.

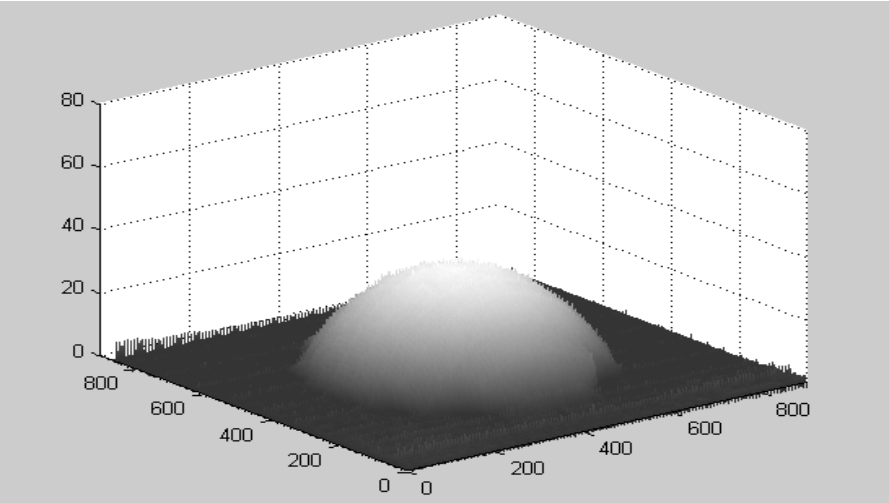

Figure 2.14 3D Reconstruction results

2.4 The Limitation of Traditional Sinusoidal Fringe

As discussed above, conventional PDE uses the detection of phase shift from original and deformed fringe patterns to enable retrieval of the 3D shape. The projected fringe pattern is limited to be sinusoidal, but in practice, problems occur that severely impact on the accuracy of measurement.

The sinusoidal fringe pattern is not suitable for the IFSE method in the SSE approach. The inverse function of a sinusoidal pattern requires a very high degree of curve fitting polynomial, which greatly increases the computation time. The curve fitting error still exists and degrades the accuracy of measurement. While increasing the degree of

curve fitting polynomial may reduce the curve fitting error, it cannot completely eliminate the error due to the characteristics of the sinusoidal function. In this section, we discuss the disadvantages of using a sinusoidal fringe pattern.

2.4.1 Disadvantages of a Sinusoidal Fringe Pattern

According to the theoretical analysis in Chapter 1, conventional PDE approaches, such as FTP and PSP, can retrieve the phase shift information precisely if the projected fringe pattern is pure sinusoidal. However, in practice, it is very hard to realise due to the undesired factors that are inherent in digital projection.

A major problem is the nonlinear projection luminous response, referred to as gamma distortion [72, 73], which is introduced by visual display systems to enhance human perception of the sensation of lightness. The gamma distortion compromises the geometric structure of the projected signal.

The gamma distortion can be considered to be a power function of intensity. In general, it can be modelled by [72, 73]:

$$w(x, y) = u(x, y)^{\gamma} \qquad \text{for } u \in [0,1] \tag{2.6}$$

where $u(x, y)$ is the image intensity function delivered to the projector, $w(x, y)$ is the actual output image intensity distribution and γ is typically a fractional value $1 < \gamma < 3$ that is specific to the display system.

Then, we suppose that the image intensity function that is delivered to the projector is a pure sinusoidal intensity distribution, which means that:

$$u(x, y) = a + b\cos(2\pi f_0 x) \tag{2.7}$$

where *a* and *b* are constants for the projected fringe offset and contrast, respectively, and f_0 is the spatial carrier frequency of the projected fringe.

Substituting Equation (2.7) to Equation (2.6), we have:

$$w(x, y) = [a + b\cos(2\pi f_0 x)]^{\gamma} \tag{2.8}$$

As we know, γ is a fractional value, and we can represent Equation (2.8) as a Fourier series below:

$$w(x, y) = c_0 + c_1\cos(2\pi f_0 x) + \sum_{m=2}^{\infty} c_m \cos(m[2\pi f_0 x]) \tag{2.9}$$

where *m* is the order of harmonic components and c_m is the corresponding amplitudes, and:

$$c_m = \frac{2}{\lambda}\int_0^{\lambda} w(x, y)\cos(m[2\pi f_0 x])dx \tag{2.10}$$

where λ is the spatial period of the fringe image.

According to Equations (2.8) and (2.9), we can see that the projected pure sinusoidal fringe is geometrically distorted and higher harmonic components are introduced due to the gamma distortion.

From Equation (1.7), we can find that the height distribution $h(x)$ is only associated with $\phi(x)$, which is the phase shift of the fundamental component. Therefore, those higher harmonic components must be eliminated if we want to retrieve the accuracy

height distribution. That is why a pure sinusoidal fringe pattern is better, but because of the gamma distortion, the higher harmonic components always exist and severely affect the accuracy of measurement.

One possible solution to the problem is to use filters to eliminate the higher harmonic components and pick up the fundamental component of the fringe pattern. However, in practice, it is difficult to design an ideal filter that can completely eliminate the higher harmonic components and make the filtered fringe pure sinusoidal. Moreover, if the deformed fringe pattern has an overlapped spectrum, bandpass filtering will also be unusable. Therefore, errors will inevitably arise if we use sinusoidal fringe pattern as projected fringe pattern.

2.4.2 Limitation in IFSE

Because the conventional PDE retrieves the height distribution of an object's surface by using the phase shift $\phi(x)$, it is vulnerable to the geometric change brought about by these distortions, such as gamma distortion and period distortion. Fortunately, because the SSE approach uses the spatial shift distribution $u(x)$ to retrieve the height distribution, it has a strong counter-interference capability against geometric distortion. Although SSE approaches provide more degrees of freedom in fringe pattern selection, in current work on SSE [83 - 86], sinusoidal fringe patterns are still employed. The issue of choosing fringe patterns with the aim to achieve the best efficiency and accuracy performance has remained unresolved.

The use of a sinusoidal fringe pattern is never the best choice for an IFSE-based SSE approach. As described above, a straightforward method to obtain the inverse function of $s(x)$ is data fitting by the following polynomial function of *k*-th order. The coefficients $a_0, a_1, \cdots, a_k$, by the least square principle, can be determined by solving

the equation:

$$\begin{bmatrix} N & \sum_{i=1}^{N} x_i & \cdots & \sum_{i=1}^{N} x_i^k \\ \sum_{i=1}^{N} x_i & \sum_{i=1}^{N} x_i^2 & \cdots & \sum_{i=1}^{N} x_i^{k+1} \\ \vdots & \vdots & & \vdots \\ \sum_{i=1}^{N} x_i^k & \sum_{i=1}^{N} x_i^{k+1} & \cdots & \sum_{i=1}^{N} x_i^{2k} \end{bmatrix} \begin{bmatrix} a_0 \\ a_1 \\ \vdots \\ a_k \end{bmatrix} = \begin{bmatrix} \sum_{i=1}^{N} y_i \\ \sum_{i=1}^{N} x_i y_i \\ \vdots \\ \sum_{i=1}^{N} x_i^k y_i \end{bmatrix} \tag{2.11}$$

where N is the number of data samples. From Equation (2.11), it is clear that with an increase in k, there will be a significant increase in computational burden. To improve efficiency in terms of computational burden, the polynomial should be as simple as possible, that is, its order sbould be as low as possible.

To show that how the order of the polynomial is related to the shape of the fringes, the sinusoidal fringe was studied, and Figure 2.15 shows the monotonic part of a sinusoidal function where the length of this segment is 100 pixels. Data fitting on its inverse function with different degrees of polynomial was performed. Table 2.2 shows the relationship between the curve fitting error e_k and k, the degrees of polynomial used for fitting, which clearly show that the degree of the polynomial must be high enough to approximate the inverse function.

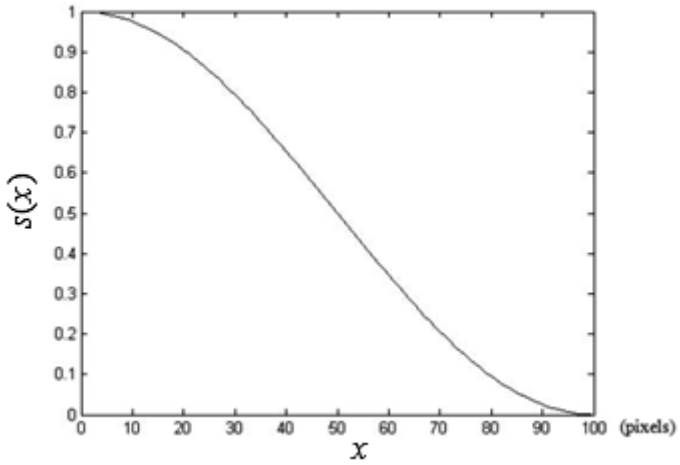

Figure 2.15 Selected monotonic interval of sinusoidal waveform

Table 2.2 Curving fitting error for different degrees of polynomial

k	1	2	3	4	5
e_k	12.0773	12.0594	1.9247	1.9197	0.6070

k	6	7	8	9	10
e_k	0.6048	0.2633	0.2621	0.1373	0.1364

2.5 DFP-based on Triangular Fringe Patterns and SSE

In the SSE approach, because the height distribution is directly retrieved from the spatial shift distribution $u(x)$, the projected fringe is not required to have any particular structure. Because there are so many disadvantages of using a sinusoidal fringe pattern as the projected fringe pattern (as discussed above), it is prudent to design a new kind of fringe pattern to use as the projected fringe pattern.

In this section, the improvement of SSE by designing a different fringe pattern to use as the projected fringe pattern instead of the traditional sinusoidal fringe is discussed. First the rules for the fringe design are given. Based on these rules, a triangular fringe pattern is proposed. Theoretical analysis follows to give a detailed illustration of the applicability of this fringe pattern.

2.5.1 Rules of Fringe Design

From Chapter 1, it is clear that the SSE approach has many advantages in comparison with the conventional PDE approach. One of these advantages is that it does not depend on the structure of the projected fringe pattern. In theory, the traditional sinusoidal fringe pattern can be replaced by some other kind of fringe pattern. But this does not mean that any fringe pattern can be used in SSE. Some fringes may be worse than sinusoidal and rules are needed to find a fringe pattern that can overcome the disadvantages of the sinusoidal fringe.

- Simple

The first rule for fringe design is that the designed fringe should be simple and concise in function.

As discussed above, the projected fringe suffers from geometric and nonlinear distortions that are mainly caused by gamma distortion. This influence is unavoidable, but it can be alleviated. To do this, fringes with simple functions that show strong counter-interference capability against gamma distortion are needed. The gamma distortion can be modelled using Equation (2.6), and using a linear function as the projected fringe function $u(x, y)$, after gamma distortion, the actual output function $w(x, y)$ will be three-degree at the maximum because γ is typically a fractional value $1 < \gamma < 3$. Hence in IFSE, a three-degree polynomial is enough for curve fitting the inverse function perfectly. The computation time will be greatly reduced.

On the other side, a high-degree function means more complexity in computation, which will increase the system load and computation time. This is not useful for real-time applications.

- Periodic

The SSE-based approach does not require the projected fringe patterns to be sinusoidal or periodic. However, non-periodic fringe patterns need to be designed each time for different objects. Therefore, the periodic fringe pattern is still used.

- Monotonic

This rule is in consideration of the IFSE method. As discussed above, IFSE requires the retrieved signal function $r = s(x)$ to be a monotonic function, or monotonic in intervals of *x*.

2.5.2 The Selection of a Triangular Fringe

Based on the rules above, two kinds of fringe pattern that satisfied all the rules are introduced. These fringes are the sawtooth fringe and the triangular fringe, which are shown in Figures 2.16 and 2.17, respectively. When the sawtooth fringe was used, a new problem arises.

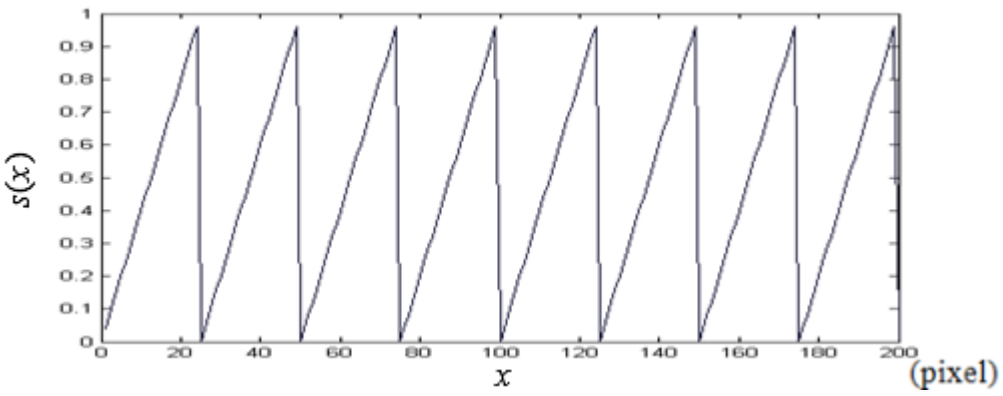

Figure 2.16 Sawtooth fringe

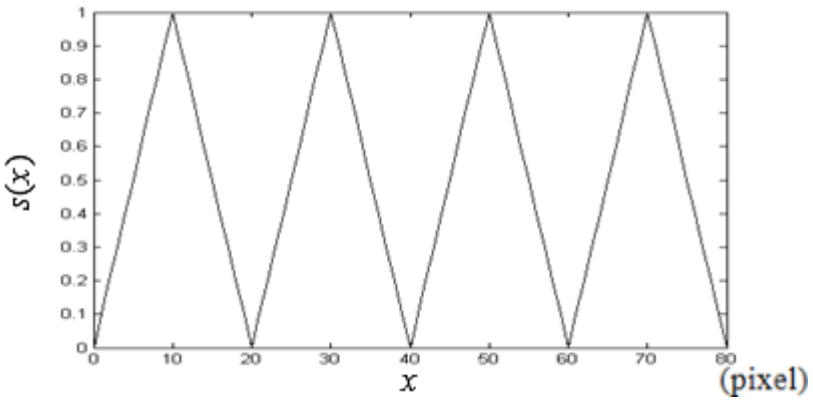

Figure 2.17 Triangle fringe

To illustrate the problem with the sawtooth fringe, a test image was projected, as shown in Figure 2.18, to analyse the distortion. This image only has two intensity levels: white and black, which represent the maximum and the minimum of the intensity. In theory, the curve of the intensity data for this image should be like that shown in Figure 2.19, which only has a sharp drop in the middle of the curve.

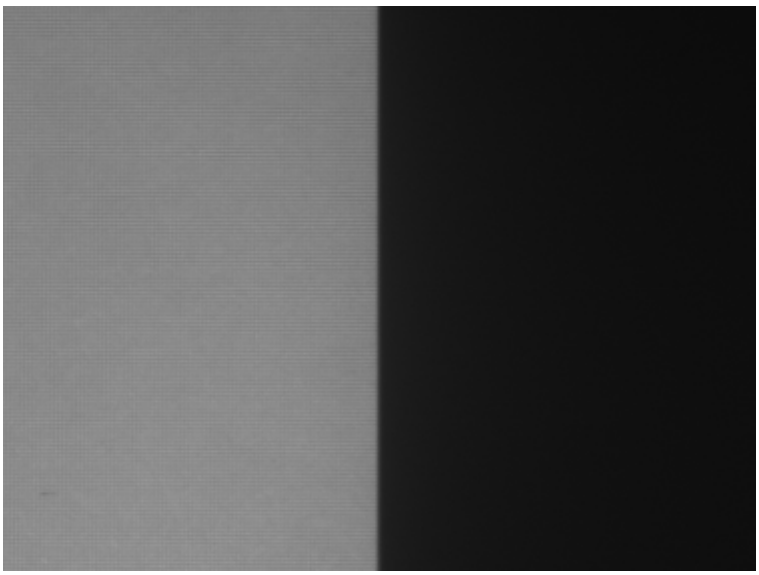

Figure 2.18 Test image with white and black

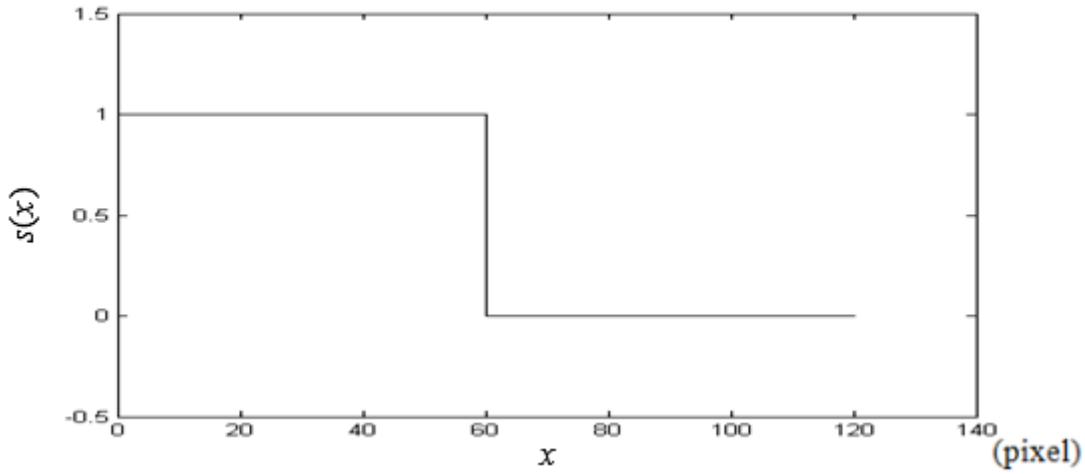

Figure 2.19 Intensity data of test image in theory

However, after projection, the intensity data retrieved from the test image is shown in Figure 2.20, which has been distorted from Figure 2.18.

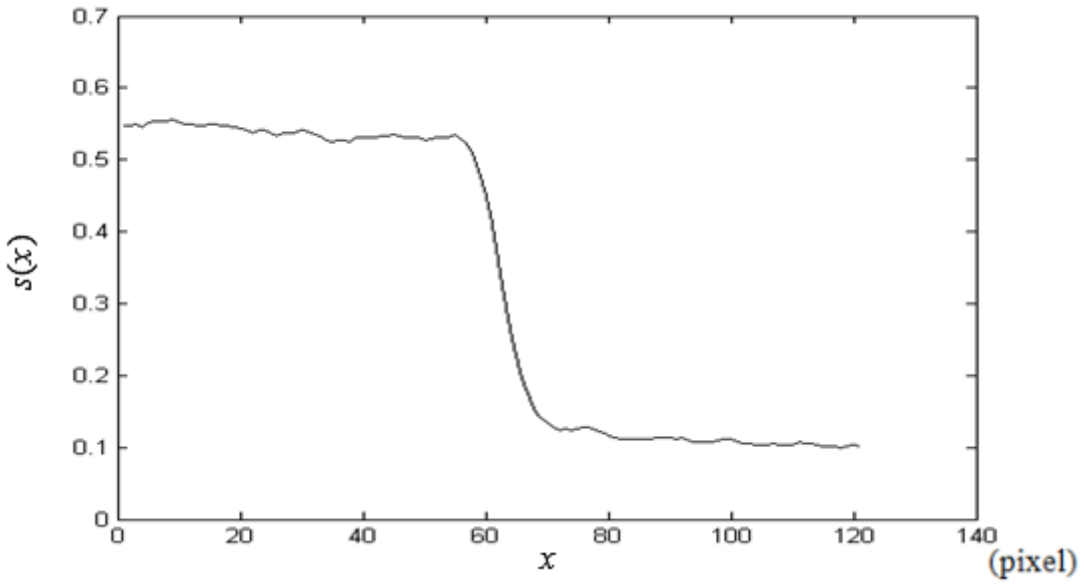

Figure 2.20 Intensity data retrieved from projected test image

In Figure 2.20, the curve structure that is supposed to be a sharp drop is distorted into a downward slope. After investigating this of distortion, each decreasing interval

generated has the same length along the *x*-axis. Hence we infer that this distortion is introduced by defocusing, which is another system limitation of the digital projector [79, 80]. The same problem occurs with the sawtooth fringe, where the sharp drops are distorted into downward slopes.

Because the triangular fringe does not have a sharp drop in its structure, it will not suffer from this kind of distortion. Hence the triangular fringe is selected for use in the new method. The following section will first give an introduction to the triangular fringe pattern, and then discuss the advantages associated with this selection.

2.5.2.1 Introduction to the Triangular Fringe

The first fringe period of the triangular pattern can be expressed as follows:

$$s(x)=\begin{cases}\dfrac{2a}{\lambda}x, & when \quad 0\le x\le\dfrac{1}{2}\lambda\\ 2a\cdot(1-\dfrac{x}{\lambda}), & when \quad \dfrac{1}{2}\lambda\le x\le\lambda\end{cases} \tag{2.12}$$

where α is the contrast of the projected fringe, which is in the range of [0, 1], and λ is the period of fringe. The whole image is a periodic extension of $s(x)$. Figure 2.17 shows an example of the pattern of 4 fringes with α = 1.0 and λ = 20 pixels.

From Equation (2.12), it is seen that the triangular function is linear and monotonic over every half of its period $n\lambda\le x\le(n+\frac{1}{2})\lambda$ and $(n+\frac{1}{2})\lambda\le x\le(n+1)\lambda$, where *n* is the fringe index. Obviously, a linear function is very good because its inverse function is also a linear function. Considering $s(x)$ within the first fringe period, the inverse function is given by the following:

$$s^{-1}(r)=\begin{cases}\dfrac{\lambda}{2a}r, & when \quad 0\le r\le a\\ \lambda(1-\dfrac{r}{2a}), & when \quad a\le r\le 2a\end{cases} \tag{2.13}$$

The above relation implies that a linear function is sufficient to estimate the inverse function if there is no distortion associated with the projection. This is very advantageous because only two coefficients are required for a pure linear function. In the presence of nonlinear distortions, triangular patterns still have advantages because the projected patterns are still close to linear, and so is the inverse function. Let us consider that the projected triangular fringe patterns are subject to gamma distortion described by Equation (2.12). The actual projected pattern in the first fringe period is:

$$s(x)=\begin{cases}\left(\frac{2a}{\lambda}\right)^{\gamma}x^{\gamma}, & when \quad 0\le x\le\frac{1}{2}\lambda\\ a^{\gamma}\cdot(2-\frac{2x}{\lambda})^{\gamma}, & when \quad \frac{1}{2}\lambda\le x\le\lambda\end{cases} \tag{2.14}$$

Because γ is typically a fractional value within the range $1 < \gamma < 3$, it is easy to evaluate the minimal degree of the polynomial for it to approximate the inverse function with a given error. Figure 2.21 gives the results of a numerical computation for the case when $\gamma = 2$. The *x*-axis is the variable *x*, and the *y*-axis is the results of $y = f_k[s(x)]$. When a perfect inverse function is used, we should have $y = f_k[s(x)] = x$, which is the solid line. Using a third-order polynomial, the dashed line is obtained, which is very close to the solid line with a very small curve fitting error of $e_k = 0.0231$. Hence, a third-order polynomial is enough to estimate the inverse function. In contrast, when a sinusoidal fringe pattern is used, a tenth-order polynomial is required to yield the same curve fitting error. Hence the triangular patterns are much more computationally efficient than the sinusoidal patterns.

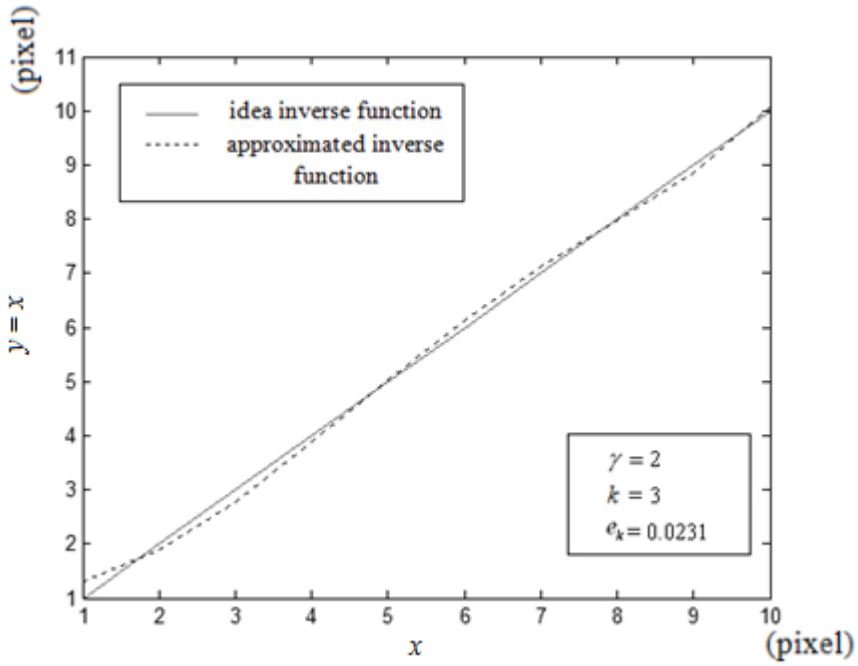

Figure 2.21 Curve of inverse functions

2.5.2.2 Advantage of Triangular Fringe

The design of this triangular fringe completely satisfies the requirements that it be simple, periodic and monotonic.

From Equation (2.12), it can be seen the triangular function we designed is a one-degree piecewise linear function. In both function and structure, it satisfies the requirement for simplicity.

From Equation (2.12), it is clear that this fringe function is controlled by adjusting the period value λ. Thus the triangular function is periodic.

From Figure 2.17, it is easy to see that the structure of the triangular function is monotonic and increases each half period.

Because the triangular function completely follows these rules, the design has great

advantages compared with the sinusoidal fringe pattern. The first advantage is reduced system load. Because the designed function is a piecewise linear function, the inverse function is easier to calculate in IFSE. The second advantage is that the triangular fringe pattern has strong counter-interference capability against geometric and nonlinear distortion, especially in solving the gamma distortion problems.

For gamma distortion, according to the Equation (2.6), the distorted fringe function will have no more than three degrees because γ is typically a fractional value $1 < \gamma < 3$. Therefore, the inverse function of the distorted fringe will also have no more than 3 degrees. For the sinusoidal fringe, at least 10 degrees are needed to achieve and the triangluar fringe has a great advantage in saving computation time.

In conclusion, the triangular fringe has advantages over the traditional sinusoidal fringe in sparing system load and counter-distortion capability, especially for gamma distortion.

2.6 Experiments and Results

2.6.1 Simulation

To test the performance of the triangular fringe pattern introduced in Section 2.5, simulation was employed to test the performance of the proposed triangular fringe pattern. A flat board with a height of 10 mm was simulated as the object's surface. The fringe images were then distorted using gamma correction with the gamma value is set to 1.60.

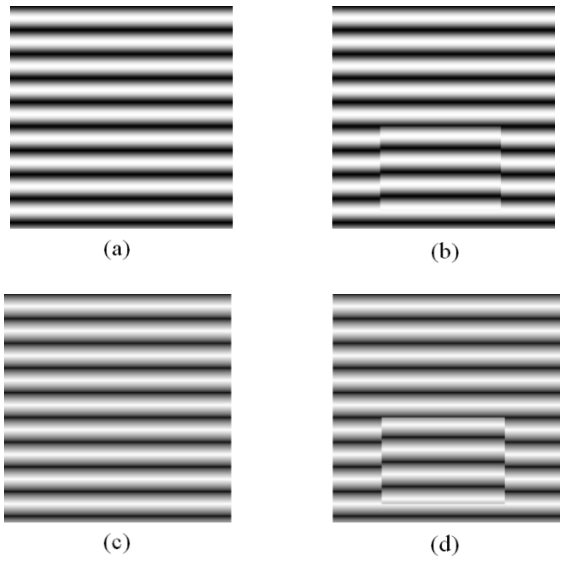

Figure 2.22 The simulated fringe pattern images

Figure 2.22 gives the simulated fringe pattern images. Figures 2.22 (a) and (b) show the sinusoidal fringe pattern on the reference plane and the object's surface, respectively, while Figures 2.22 (c) and (d) show the triangular fringe pattern on the reference plane and the object's surface, respectively.

Figure 2.23 (a) shows the height distribution of a cross-section of the flat board at the central line. In this figure, x represents the length of flat board (in pixels) and h is the height (mm). Note that the degree of the polynomial for the inverse function was selected to be 3 (k = 3). Figures 2.23 (b) and (c) show the results using the sinusoidal fringe pattern in the cases of k = 3 and 10, respectively.

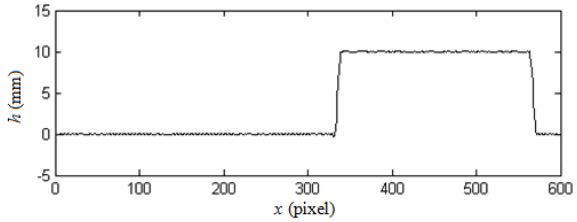

(a) Retrieved height distribution using triangular fringe, k = 3

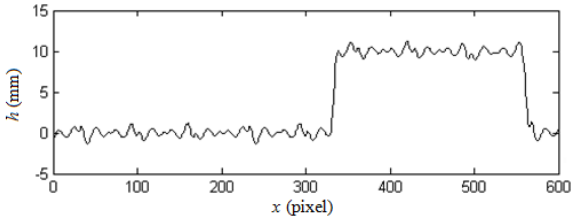

(b) Retrieved height distribution using sinusoidal fringe, k = 3

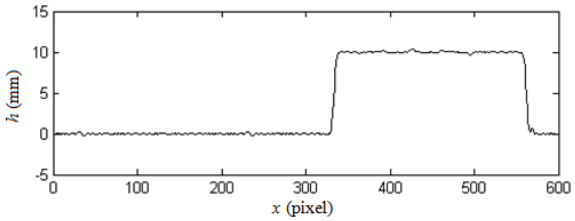

(c) Retrieved height distribution using sinusoidal fringe, k = 10

Figure 2.23 Retrieved height distribution results (simulated board)

The reconstructed 3D surface shape of the object is shown in Figure 2.24. Figure 2.24 (a) is the result using triangular fringe with k = 3. The results from using a sinusoidal fringe are shown in Figures 2.24 (b) and (c), where the polynomial degrees are 3 and 10, respectively.

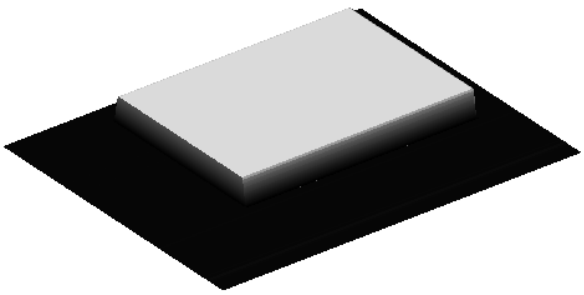

(a) 3D reconstructed result using triangular fringe, k = 3

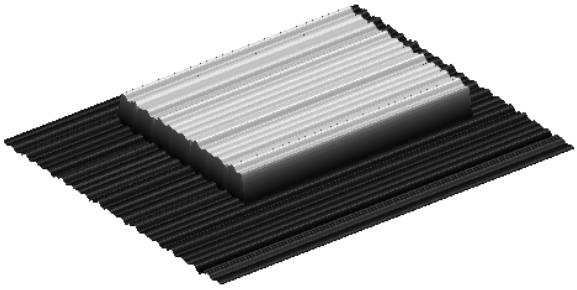

(b) 3D reconstructed result using sinusoidal fringe, k = 3

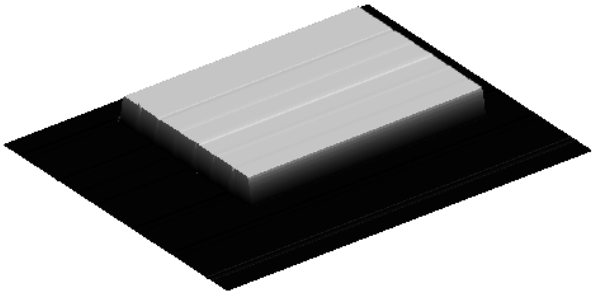

(c) 3D reconstructed result using sinusoidal fringe, $k = 10$

Figure 2.24 3D reconstructed results (simulated board)

The error distributions of these reconstruct results was calculated and are shown in Table 2.3.

Table 2.3 Error distribution of reconstruct results (simulated board)

	Max error (Positive)	Max error (Negative)	Mean square error
Triangular fringe ($k = 3$)	0.0494 mm	−0.0515 mm	0.0007 mm
Sinusoidal fringe ($k = 3$)	1.1923 mm	−1.0033 mm	0.2196 mm
Sinusoidal fringe ($k = 10$)	0.3633 mm	−0.3094 mm	0.0084 mm

From the results above, we can see that with same polynomial degree, the triangular fringe performs much better than the sinusoidal fringe. Also, for the same level of accuracy, the degree of polynomial associated with triangular fringe patterns can be much lower than that needed with the sinusoidal patterns. The degree of the polynomial has significant impact on the efficiency of the 3D measurement in terms of computational burden and the time required. In the examples above, where the

degrees of the polynomials for sinusoidal and triangular patterns were 10 and 3, respectively, there will be a significant reduction in terms of computational burden with the proposed approach.

2.6.2 Experiments and Results

Experiments were also carried out in the laboratory to verify the validity of the proposed method. The experimental set-up was the same as that in Section 2.3.

The first object used was a flat board with height is 18 mm. The captured sinusoidal fringe patterns on the object's surface and on the reference plane are shown in Figures 2.25 (a) and (b) respectively. Figures 2.25 (c) and (d) show the captured triangular fringe patterns on the object's surface and on the reference plane. In the figures, there are 13 fringes, each covering 30 pixels. The resolution of each captured fringe images is 390 × 390 pixels.

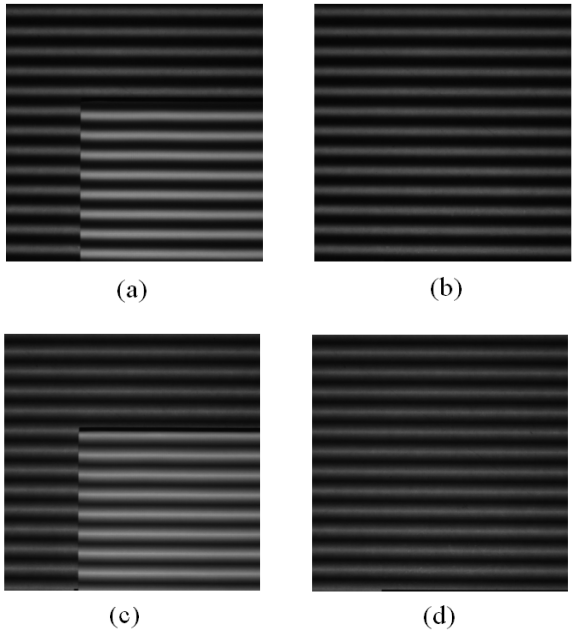

Figure 2.25 Fringe patterns observed (board)

The fringe was divided into monotonic intervals and the IFSE approach was applied to each of the intervals to obtain the height distribution of the board. Figure 2.26 (a) shows the height distribution of a cross-section of the board at the central line. In this figure, x is the length of board (in pixels), and h label is the height (mm). Note that the degree of the polynomial for the inverse function was selected to be 3 (k = 3).

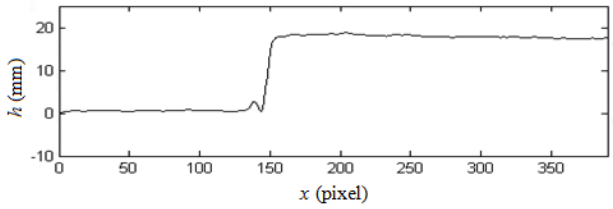

(a) Retrieved height distribution using triangular fringe, k = 3

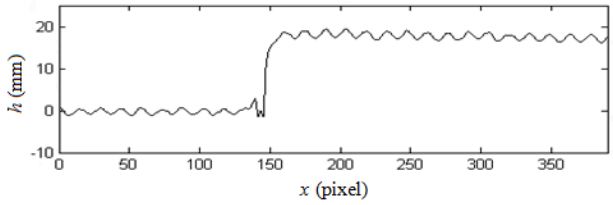

(b) Retrieved height distribution using sinusoidal fringe, k = 3

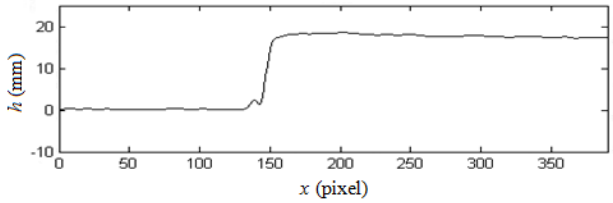

(c) Retrieved height distribution using sinusoidal fringe, k = 10

Figure 2.26 Retrieved height distribution result (board)

Figure 2.26 also gives the results of height distribution retrieved using the sinusoidal fringe with different polynomial degrees. Figures 2.26 (b) and (c) show height distributions where the degree of the polynomials was 3 and 10, respectively.

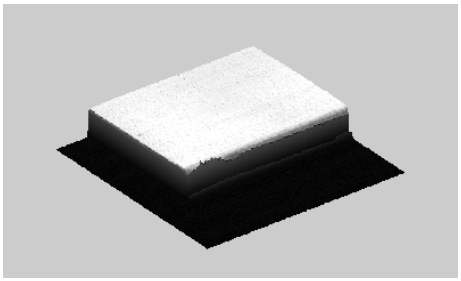

(a) 3D reconstructed result using triangular fringe, k = 3

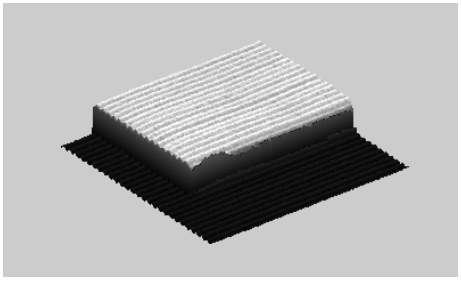

(b) 3D reconstructed result using sinusoidal fringe, k = 3

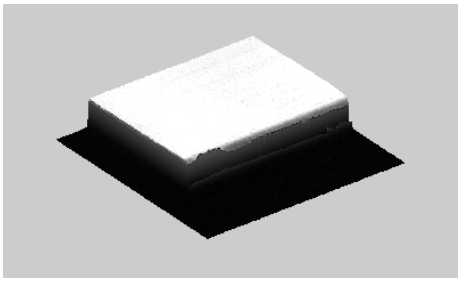

(c) 3D reconstructed result using sinusoidal fringe, k = 10

Figure 2.27 3D reconstruct results (board)

The 3D surface shape of the object was reconstructed using triangular patterns where the degree of polynomial is 3 and the results are shown in Figure 2.27 (a). For comparison, results of the reconstructions using the sinusoidal patterns with polynomials of degree 3 and 10 are depicted in Figures 2.27 (b) and (c), respectively. Because the height of this board is already known, the error distributions of these reconstructed results were calculated and are shown in Table 2.4.

Table 2.4 Error distribution of reconstruct results (board)

	Max error (positive)	Max error (negative)	Mean square error
Triangular fringe (k = 3)	0.8290 mm	−0.7094 mm	0.1407 mm
Sinusoidal fringe (k = 3)	1.4787 mm	−2.0044 mm	0.6493 mm
Sinusoidal fringe (k = 10)	0.5456 mm	−0.7875 mm	0.1627 mm

It can be seen that, using third-degree polynomials, the proposed triangular patterns yield much higher accuracy than the sinusoidal pattern. To achieve the same accuracy with a sinusoidal pattern, the degree of the polynomial must be much higher (i.e. 10) than that used for triangular patterns (i.e., 3).

The proposed technique was also tested using the dome. Figure 2.28 shows the captured fringe patterns using sinusoidal fringe pattern (a, b) and triangular fringe pattern (c, d). There were about 8 fringes, each covering 40 pixels. The resolution of each captured fringe images is 320 × 320 pixels.

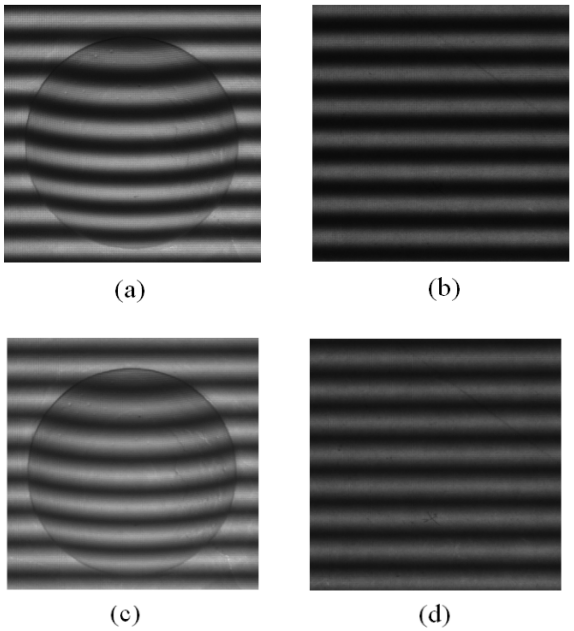

Figure 2.28 Fringe patterns observed (dome)

Figure 2.29 shows the height distribution obtained for the middle line in this dome. Figure 2.29 (a) is the reconstructed object shape using triangular fringe pattern with polynomial degree k = 3, and Figures 2.29 (b) and (c) gives the reconstructed object shape using a sinusoidal fringe with polynomial degrees k = 3 and k = 10, respectively. From these results, it can be seen that for the degree of polynomial of 10 or above, the sinusoidal pattern can achieve the same accuracy as using a triangular pattern with polynomial degree k = 3.

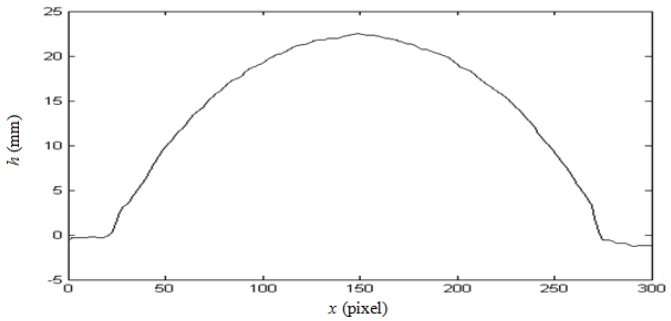

(a) Retrieved height distribution using triangular fringe, k = 3

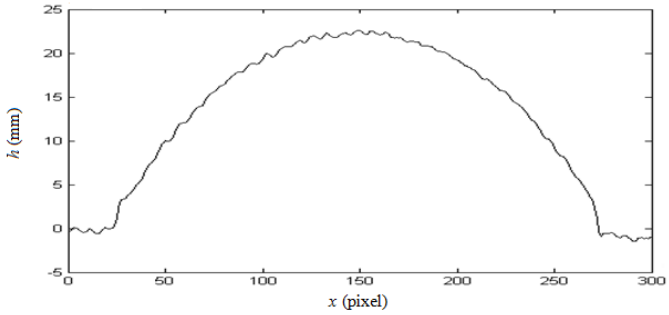

(b) Retrieved height distribution using sinusoidal fringe, k = 3

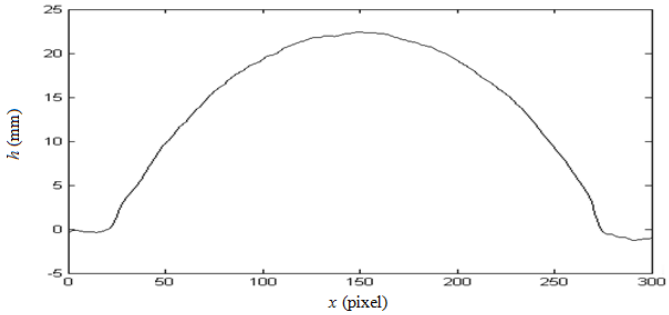

(c) Retrieved height distribution using sinusoidal fringe, k = 10

Figure 2.29 Retrieved height distribution result (dome)

Figure 2.30 gives the reconstructed 3D surface shape of the object. Figure 2.30 (a) shows the result using a triangular fringe with $k = 3$. Figures 2.30 (b) and (c) show the results using a sinusoidal fringe with $k = 3$ and 10, respectively.

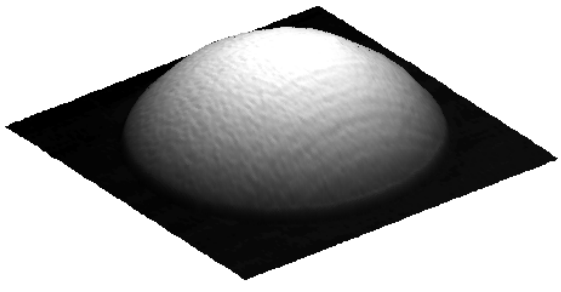

(a) 3D reconstructed result using triangular fringe, k = 3

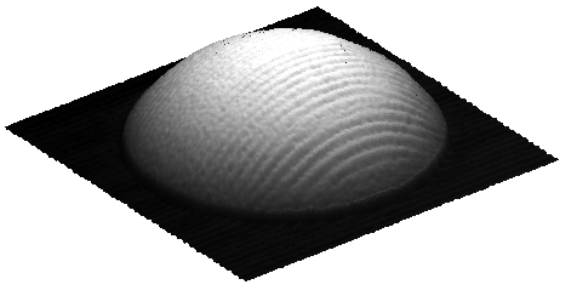

(b) 3D reconstructed result using sinusoidal fringe, k = 3

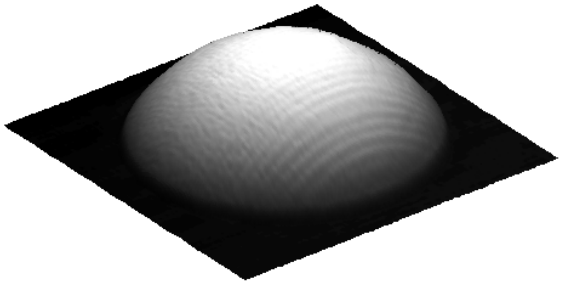

(c) 3D reconstructed result using sinusoidal fringe, k = 10

Figure 2.30 3D reconstructed results (dome)

From the results above, the triangular fringe performs much better than sinusoidal fringe with same polynomial degree and for the same level of accuracy; the degree of polynomial associated with triangular fringe patterns can be much lower than that with the sinusoidal patterns. These experimental results successfully verified the efficiency of the proposed method, where using the sinusoidal fringe patterns will spend more calculation time compared with using triangular fringe patterns in the same accuracy level.

It should be pointed out that the proposed approach is based on projection of a single fringe pattern, and the measurement accuracy is not as high as these approaches using multiple image patterns, such as multi-step PSP. In chapter 4, we will investigate the use of multiple triangular fringe patterns.

2.7 Conclusions

In this chapter, the implementation of the SSE approach was presented. First, a DFP system was set up. Detailed information about this system was given, including the system structure and software interface. Then the procedure of implementation was introduced with an emphasis on the problems encountered in practice. Proposed solutions included pre-processing and improving the IFSE method. The result is shown to prove the contribution of the implementation, where the computation time is greatly reduced while using the improved IFSE method.

This chapter also discussed the shortcomings and limitations associated with the use of sinusoidal fringe patterns. The sinusoidal waveform is vulnerable to geometry distortion and nonlinear intensity distortion, and it not suitable for the IFSE method in SSE approach. All of these problems result in additional computation.

To address these limitations, a novel IFSE method was proposed based on theoretical analysis. This method uses the triangular fringe pattern instead of a sinusoidal fringe pattern. In contrast with the method using sinusoidal fringe patterns, the proposed method is advantageous because it has (1) better immunity to nonlinear distortions associated with digital projection and (2) improved efficiency in terms of computational burden required for 3D measurement. The performance of the proposed method was then verified by simulations and experiments.

Chapter 3 Shift Unwrapping in the SSE Approach

3.1 Introduction

In both PDE and SSE, the wrapping problem exists and becomes a major impediment to retrieving height distribution information about object surfaces. In PDE-based approaches, the phases are limited within the main range from $[-\pi, \pi]$. To restore the actual shape of the object, phase unwrapping must be carried out. In the SSE-based approach, most of the projected fringe patterns are also periodic and the shift can only be detected without ambiguity within the range of $[0, \lambda]$, where λ is the width of the individual fringe. This will also result in discontinuity. Many methods have been proposed to solve the unwrapping problem in the PDE approach [44 - 71], but little work has yet done for the unwrapping problem in the SSE approach. In this chaper, a review of the phase wrapping problem in PDE-based FPP and the shift wrapping problem in SSE-based FPP is presented. Two approaches for carrying out shift unwrapping are proposed with their performance confirmed by experiments.

This chapter is organised as follows. Section 3.2 presents a detailed introduction of the wrapping problem, including the wrapping problem in both the conventional PDE and SSE approaches. Section 3.3 discusses unwrapping as the solution to the wrapping problem. This includes a review of the phase unwrapping problem, and based on this, a new theory of shift unwrapping using a reliability-guided algorithm is given. An experiment is then described that confirms the performance of the new shift unwrapping theory. Section 3.4 introduces another shift unwrapping method in which multiple-wavelengths are used. This section gives a review of the multiple-wavelength phase unwrapping algorithm introduced by Zhang [68, 69], and based on this, a multiple-wavelength unwrapping algorithm for the SSE approach is proposed. Experimental results are then given to demonstrate that the proposed method can be used to measure complex objects with significant step height using the

SSE approach. Section 3.5 provides the conclusion to this chapter.

3.2 The Wrapping Problem

As discussed previously, in the conventional PDE approach, the phase shift information contains the height distribution of object surface. However, the phase function is a periodic function with the period of 2π, and the phase shift information retrieved in most PDE-based approaches can only be identified within the range of [−π, π]. A phase shift that is bigger than π or smaller than −π is wrapped into this range and the wrapping problem occurs. The same problem occurs in the SSE approach because the projected fringe is a periodic fringe of width λ. The spatial shift information retrieved will only be detected within the main value of [0, λ] and this can also be considered to be a wrapping problem.

3.2.1 Wrapping Problem in the Conventional PDE Approach

From Equation (1.7) we have:

$$\phi(x) = 2\pi \frac{d_0 h(x)}{\lambda l_0} \tag{3.1}$$

where $\lambda = 1/f_0$ is the width of an individual fringe. Obviously, $\phi(x)$ can take any value, depending on $h(x)$, d_0, l_0 and λ. However, with most PDE-based approaches, $\phi(x)$ can only be identified within the range of [−π, π]. In other words, $\phi(x)$ is obtained by the modulo 2π operation, resulting in discontinuities in its values near π (pi and −pi) appearing in the phase map. This is called the wrapping problem. To recover the absolute phase $\Phi(x)$ from the wrapped phase $\phi(x)$, we have:

$$\Phi(x) = 2\pi m(x) + \phi(x) \text{, where } m(x) = Integer\left[\frac{\Phi(x)}{2\pi}\right] \tag{3.2}$$

where $m(x)$ is an integer indicating the number of 2π lost due to the wrapping problem. The procedure of retrieving $m(x)$ is called phase unwrapping [69].

3.2.2 Wrapping Problem in the SSE Approach

The wrapping problem also exists in SSE-based approaches. From Equation (1.17) we have:

$$u(x) = \frac{d_0 h(x)}{l_0} \tag{3.3}$$

Depending on $h(x)$, d_0 and l_0, the shift function $u(x)$ may take any value. However, because $s(x)$ has a fringe structure with a periodic fringe of width λ, $u(x)$ can only be detected within the main values of [0, λ]. In other words, $u(x)$ is wrapped into [0, λ]. The absolute shift function, denoted as $U(x)$, should be continous and can be recovered from the wrapped shift function $u(x)$ as follows:

$$U(x) = \lambda m(x) + u(x) \text{, where } m(x) = Integer\left[\frac{U(x)}{\lambda}\right] \tag{3.4}$$

This process is referred to as shift unwrapping.

3.3 Reliability-guided Shift Unwrapping Algorithm

As discussed earlier, the wrapping problem exists in both conventional PDE and SSE. Because the wrapping problem causes the height distribution information to suffer from great distortion, it becomes a main obstacle to 3D profilometry. To solve the wrapping problem, unwrapping is needed. Unwrapping is a process that restores the original phase or shift map. Because the conventional PDE approach has attracted most research interest, solutions for the wrapping problem in the phase shift based approaches are also given. These solutions are referred to the phase unwrapping approaches [44, 45].

In SSE-based FPP, shift unwrapping is also required to restore the 3D shape of the object's surface correctly. However, shift unwrapping for SSE-based FPP is still an outstanding issue. In this section, the phase unwrapping problem in PDE-based approaches is first reviewed, and a method for solving the shift unwrapping problem is then presented.

3.3.1 A Review of Phase Unwrapping

Phase unwrapping refers to the process of restoring $\Phi(x)$ from $\phi(x)$. Usually, the phase is wrapped in the following way. When $\Phi(x)$ increases and reaches points π, 3π, 5π, … (i.e., odd multiples of π), $\phi(x)$ drops from π to $-\pi$. Similarly, when $\Phi(x)$ decreases and reaches the same points, $\phi(x)$ jumps from $-\pi$ to π. The phase unwrapping process should reverse this process. When the phase drops from π to $-\pi$, we should add 2π to the unwrapped $\Phi(x)$, and when the phase jumps from $-\pi$ to π, we should add -2π.

Most existing phase unwrapping approaches begin by determining the differences

between neighbouring values. If a value suffers from wrapping, the absolute value of the difference should be more than π and can be determined as a breach of the continuity of the original phase map. This value is then recorded as a discrete point. The compensation of 2π is performed based on these discrete points to reconstruct the unwrapped phase maps. It is important to note that these methods are based on the hypothesis that the differences between neighbouring values in the original phase map are less than π.

3.3.2 Shift Unwrapping in SSE-based FPP

To work out how to unwrap the shift, we can see how $U(x)$ is wrapped into $u(x)$:

- When $U(x)$ increases and reaches points λ, 2λ, 3λ, … (i.e., integer multiples of λ), $u(x)$ exhibits a drop of λ with its value dropping from λ to 0.
- When $U(x)$ decreases and reaches the same points, $u(x)$ will jump from 0 to λ.

Shift unwrapping should reverse process to go from $u(x)$ to $U(x)$. When we observe a drop from λ to 0, we should add λ to the wrapped result, and when we notice a jump from 0 to λ, we should add −λ. Assuming that the object has a continuous surface and that $u(x)$ is acquired in discrete form, that is $u(x)$ ($i = 0, 2, 3, ..., N$), shift unwrapping should be carried out using the following procedure:

Step 1: Initialisation $U(x) = \lambda m(x) + u(x)$, where $m(x_0)$ is determined by the height of the object at x_0. Because $u(x) << \lambda$, from Equations (3.3) and (3.4) we have $u(x_0) = \dfrac{d_0 h(x_0)}{l_0}$ and $m(x_0) = Integer\left[\dfrac{U(x_0)}{\lambda}\right]$

Step 2: Start from $u(x_0)$ and for $u(x_i)$, where $i = 1, 2, 3, ..., N$. If $U(x_i)$ increases and is followed by a drop of λ (i.e., $u(x_i) - u(x_{i-1}) = -\lambda$), we should

increase $m(x)$ by 1 (i.e., $m(x_i) = m(x_{i-1}) + 1$). If $U(x_i)$ decreases followed by a jump of λ (i.e., $u(x_i) - u(x_{i-1}) = \lambda$), then decrease $m(x)$ by 1 (i.e., $m(x_i) = m(x_{i-1}) - 1$) otherwise, keep $m(x)$ unchanged (i.e., $m(x_i) = m(x_{i-1})$). Compute the unwrapped shift by $U(x) = \lambda m(x) + u(x)$

The above procedure is straightforward, but a number of issues must be resolved for its implementation in practice. Firstly, we need to determine if $u(x_i)$ increases or decreases. Secondly we need to be able to detect sharp drops and sharp jumps. In ideal cases when the surface is continuous, $s(x_i)$ and $d(x_i)$ are free of noise and these can be detected easily. However, in practice, both $s(x_i)$ and $d(x_i)$ may contain noise, resulting in $u(x_i)$ that is corrupted by noise and disturbance. To eliminate the influence of noise and disturbance, we should ensure that $u(x_i)$ is as smooth as possible with respect to x_i . To this end the following is proposed:

- Pre-processing of $s(x_i)$ and $d(x_i)$ by means of a digital filter to remove noise and to smooth the waveform of $s(x_i)$ and $d(x_i)$. The aim of pre-processing is to eliminate unwanted noise and disturbance while retaining the original waveform of $s(x_i)$ and $d(x_i)$. The selection of parameters for these filters can follow the method introduced in Section 2.3.1.1.
- To determine the slope of $s(x_i)$, we first evaluate the difference of $u(x_i)$ over successive samples by $\Delta u(x_i) = u(x_i) - u(x_{i-1})$, and then take the sign of the variance by $\delta_i = sign\{\Delta u(x_i)\}$ (where δ_i equals 1, 0 and −1 for $\Delta u(x_i) > 0$, $\Delta u(x_i) = 0$ and $\Delta u(x_i) < 0$, respectively). We carry out the following:

If $\frac{1}{M}\sum_{j=i-M}^{i-1}\delta_i > 0$, then $u(x_i)$ increases, or

If $\frac{1}{M}\sum_{j=i-M}^{i-1}\delta_i < 0$, then $u(x_i)$ decreases.

In practice, a sharp jump or drop may transverse a few data samples on $u(x_i)$. Assuming that the jump or drop occurs within *L* samples, we can use the following to detect the drop:

If $u(x_i)-u(x_{i-L}) > \lambda_t$, then $u(x_i)$ jumps, or

If $u(x_i)-u(x_{i-L}) < -\lambda_t$, then $u(x_i)$ drops.

where λ_t is a threshold that should be chosen based on the quality of $u(x_i)$. With the pre-processing of $s(x_i)$ and $d(x_i)$, $u(x_i)$ is smooth enough and we choose $\lambda_t = \lambda/2$.

3.3.3 A Novel Shift Unwrapping Algorithm based on Reliability-guided Method

Although the shift unwrapping method introduced in the previous section is rather simple, the implementation of this method in practice is still a challenging task. As discussed earlier, this method can only be implemented easily in ideal cases when the surface is continuous and when $s(x_i)$ and $d(x_i)$ are free of noise. This shift unwrapping method suffers from discontinuity on object surfaces and the wrong decision may be made regarding the addition or substraction of λ. To solve this problem, one approach is the quality-guided unwrapping method, which carries out phase unwrapping by comparing the wrapped phase at neighbouring pixels and adding or subtracting multiples of 2π. A quality map is used to guide the phase unwrapping

path. The unwrapping process starts from the highest quality point and continues to the lower quality ones until it finishes. Several methods have been proposed to generate the quality map [46 – 53].

Similar to the method in Herráez *et al*. [50], the method introduced also creates a reliability map to guide the unwrapping path. The reliability map is constructed based on the second difference between a value and its neighbouring pixels. The calculation of second differences for pixels in an image can be explained with the help of Figure 3.1.

$(x\text{-}1, y\text{-}1)$	$(x\text{-}1, y\text{-}1)$	$(x+1, y\text{-}1)$
$(x\text{-}1, y)$	(x, y)	$(x+1, y)$
$(x\text{-}1, y+1)$	$(x, y+1)$	$(x+1, y+1)$

Figure 3.1 Calculation of the second differences in an image

To calculate the second difference for a pixel, the values of its orthogonal and diagonal neighbours in a 3 × 3 window are required. The second difference D of an (x, y) pixel then can be calculated using the equation:

$$D(x,y) = [H^2(x,y) + V^2(x,y) + D_1^2(x,y) + D_2^2(x,y)]^{1/2} \tag{3.5}$$

where

$$
\begin{aligned}
H(x,y) &= W[u(x-1,y)-u(x,y)]-W[u(x,y)-u(x+1,y)] \\
V(x,y) &= W[u(x,y-1)-u(x,y)]-W[u(x,y)-u(x,y+1)] \\
D_1(x,y) &= W[u(x-1,y-1)-u(x,y)]-W[u(x,y)-u(x+1,y+1)] \\
D_2(x,y) &= W[u(x-1,y+1)-u(x,y)]-W[u(x,y)-u(x+1,y-1)]
\end{aligned}
\tag{3.6}
$$

$W((\cdot))$ is a simple wrapping operation to remove any λ steps between two consecutive pixels. For pixels at the borders of the image, the second differences *D* are set to infinity.

Thus the reliability *R* of a pixel is defined as

$$R = \frac{1}{D} \tag{3.7}$$

Consequently, pixels are more reliable if their second differences are lower.

Once the reliability map is built, the unwrapping path can be found using the same algorithm given in Herráez *et al*. [50].

3.3.4 Experiments and Results

To test the performance of the approach proposed in Section 3.3.3, laboratory experiments were carried. The experimental set-up was same as in Chapter 2.

In this experiment, two half domes were used as measurement objects. Figure 3.2 (a) shows the objects and Figure 3.2 (b) shows the captured triangular fringe patterns on the object's surface. The resolution of each captured fringe images is 500 × 300 pixels.

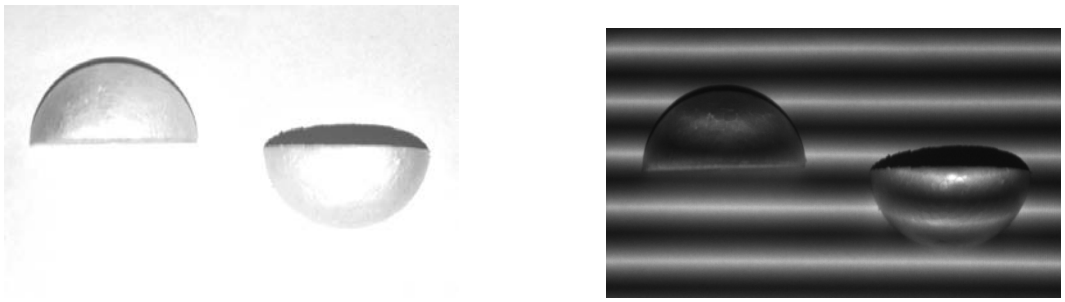

(a) (b)

Figure 3.2 Captured images of two half domes: (a) objects, (b) fringes images

The proposed reliability-guided shift unwrapping algorithm is then used to perform the unwrapping. Figure 3.3 shows the 3D reconstructed results, where Figure 3.3 (a) shows the wrapped result, and Figure 3.2 (b) gives the result after unwrapping.

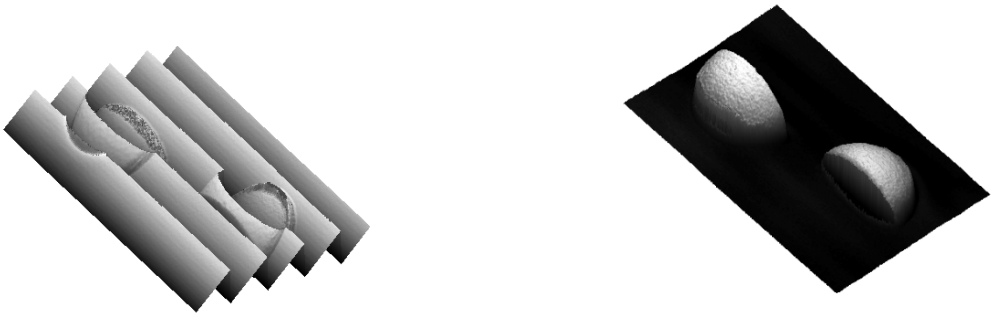

(a) (b)

Figure 3.3 3D reconstruct result: (a) wrapped result and (b) unwrapped result

It can be seen that both objects have discontinuity on their surface. After unwrapping using the proposed method, the object's surface information is retrieved correctly. This result demonstrates that the proposed method can solve the shift unwrapping problem and successfully measure objects with discontinuity on their surfaces.

3.4 Multiple-Wavelength Shift Unwrapping Algorithm

In Section 3.3, a reliability-guided shift unwrapping algorithm to solve the shift

unwrapping problem was introduced. The experimental result demonstrated that the proposed method shows good performance on shift unwrapping, even if there is some discontinuities on the object's surface. However, because this method performs unwrapping by accessing its neighbouring pixels, it has a limitation when unwrapping the shift map for arbitrary step heights or isolated parts.

The same problem also happens in phase unwrapping. To solve this problem, Zhang [68, 69] introduced a multiple-wavelength phase unwrapping algorithm. In Zhang's method [68, 69], an image with a single fringe covering the whole measurement area is first projected, followed by a series of fringe images with the number of fringes on each image increasing by a constant factor. Because the first image only contains one fringe, unwrapping is not required. Then the phase of the second image can be unwrapped by referring to the first image. After the phase of second image is obtained, it can be used to correct the third image, and so on.

Inspired by Zhang's method [69], a new approach is introduced to unwrap the shift. In the proposed method, a series of fringe images are projected. The first image has only one fringe covering the whole measurement area, and other images are characterised by their wavelengths decreasing by a constant factor. As with Zhang's method [69], shift unwrapping is carried out sequentially, starting with the images with the longest wavelengths to the images with the shortest wavelengths.

3.4.1 A Review of the Multiple-wavelength Phase Unwrapping Algorithm

In this section, a brief review of the multiple-wavelength phase unwrapping algorithm proposed by Zhang [69] is given. In this method, a series of fringe patterns are projected one-by-one. Supposing that the measurement area has a resolution of $W \times H$ and the projected fringe images are vertical, the first fringe pattern only has a single fringe with its spatial wavelength λ_1 the same as W. As the fringe covers the whole

measurement area, phase unwrapping is not required, and $\phi_1(x) = \Phi_1(x)$ and $m_1(x) \equiv 0$.

A series of fringe images are then projected with their wavelengths decreased by a factor of 1/*N*. For example, the wavelength of the *k*th fringe pattern is given by $\lambda_k = N\lambda_{k+1}$. As we know, $\phi_1(x) = \Phi_1(x)$, and because $\lambda_1 = N\lambda_2$, it will have $\Phi_2(x) = N\Phi_1(x)$ [69]. Combining this with Equation (3.2) yields the following:

$$m_2(x) = Integer\left[\frac{N\Phi_1(x)}{2\pi} - \frac{\phi_2(x)}{2\pi}\right] \tag{3.8}$$

where the operator Integer[.] obtains the closest integer value. The wrapped phase $\phi_2(x)$ can be unwrapped on a pixel-by-pixel basis by referring to the retrieved $m_2(x)$:

$$\Phi_2(x) = 2\pi m_2(x) + \phi_2(x) \tag{3.9}$$

After $\Phi_2(x)$ is obtained, it can be used to recover $\phi_3(x)$. Therefore, in general, for $\lambda_k = \lambda_{k-1} / N$,

$$m_k(x) = Integer\left[\frac{N\Phi_{k-1}(x)}{2\pi} - \frac{\phi_k(x)}{2\pi}\right] \tag{3.10}$$

and the absolute phase map $\Phi_k(x)$ can be retrieved using Equation (3.2).

Because the unwrapped phase is obtained without relying on pixel neighbourhoods within the same phase map, unwrapping errors will not propagate from one noisy neighbourhood to spatially adjacent regions of the image. Similarly, noise contained in images obtained using longer wavelengths will not propagate into images obtained using shorter wavelengths. Therefore, this technique can more accurately measure

complex surfaces that may contain significantly elevated profile steps, while at the same time improving reliability and noise immunity by minimising the propagation of localised phase unwrapping errors.

3.4.2 A Novel Shift Unwrapping Algorithm based on Multiple-wavelength Method

Based on Zhang's method [69], a multiple-wavelength unwrapping algorithm for SSE approach is introduced. In this algorithm, we assume that the measurement area has a resolution of $W \times H$ and the projected fringe images are vertical. The wavelength of the fringe that is projected initially is selected to be W, that is, $\lambda_1 = W$. Because this single fringe stripe covers the whole measurement area, shift unwrapping is not needed, and we have $u_1(x) = U_1(x)$ and $m_1(x) \equiv 0$.

We then choose $\lambda_2 = \lambda_1 / N$. From Equation (3.3), it is easy to see that the real shift function $U(x)$ is only related to the height distribution $h(x)$ and the two distances d_0 and l_0. Because these values are fixed, the true shift functions for different wavelengths λ should be the same, that is, $U_2(x) = U_1(x) = U(x)$. Combining this with Equation (3.4), we have:

$$m_2(x) = Integer\left[\frac{U_1(x)}{\lambda_2} - \frac{u_2(x)}{\lambda_2}\right] \tag{3.11}$$

This means that $u_2(x)$ can now be unwrapped using $m_2(x)$, which in turn was obtained from information contained in the longer wavelength shift $U_1(x)$. This can be carried out on a pixel-by-pixel basis:

$$U_2(x) = \lambda_2 m_2(x) + u_2(x) \tag{3.12}$$

Because the shift $U_1(x)$ is only used for obtaining the integer $m_2(x)$, the noise of $U_1(x)$ does not propagate to $U_2(x)$. With $U_2(x)$ retrieved, we now can use it to obtain $U_3(x)$, where $\lambda_3 = \lambda_2 / N$. In general, for $\lambda_k = \lambda_{k-1} / N$, we have:

$$m_k(x) = Integer\left[\frac{U_{k-1}(x)}{\lambda_k} - \frac{u_k(x)}{\lambda_k}\right] \tag{3.13}$$

and the real shift function $U(x)$ can be retrieved using Equation (3.4).

From Equation (3.13), we can find that the unwrapped shift map is retrieved by referring to the longer wavelength shift map. Compared with algorithms that use neighbouring pixels to do the unwrapping, the method proposed here can measure the surface profile with larger steps. Because the noise from the longer wavelengths' images will not propagate to the shorter wavelength images, the measurement's overall accuracy is purely determined by the image with the shortest wavelength.

3.4.3 Experiments and Results

To test the performance of the approach proposed in Section 3.4.2, experiments were carried out in the laboratory. The experimental set-up is the same as for the previous experiments. To verify that the proposed method can measure the surface profile with arbitrary step height, a flat box of 43 mm high was first chosen as the measured object. Figure 3.4 (a) shows a photograph of the object. Figure 3.4 (b) shows the captured triangular-pattern fringe image of the object with wavelength $\lambda = 20$. Figures 3.4 (c) and (d) show the captured fringe images of the object with wavelengths $\lambda = 40$ and $\lambda = 80$. In order to highlight the edge part of box, the capture images are cut into the resolution of 140 × 80 pixels.

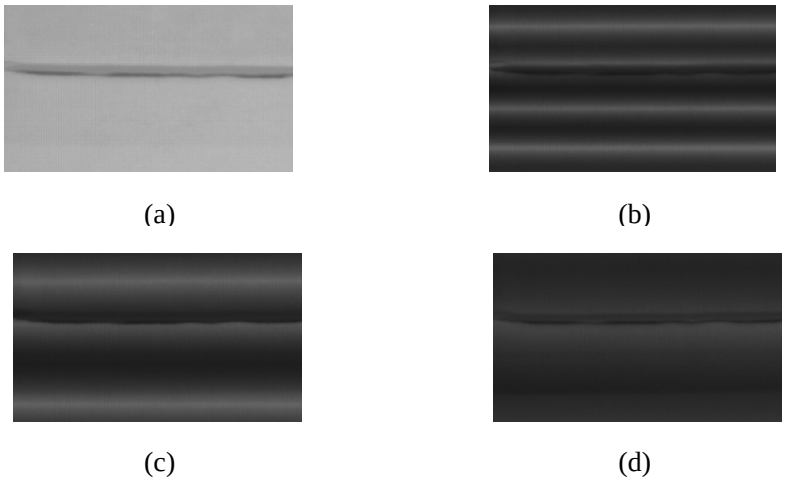

(a) (b)

(c) (d)

Figure 3.4 Captured fringe images of a flat box: (a) object, (b) fringes image (λ = 20), (c) fringes image (λ = 40) and (d) fringes image (λ = 80)

We first reconstruct this object using the single wavelength triangular-pattern spatial-shifting algorithm. The wrapped $u(x)$ is unwrapped using the reliability-guided shift unwrapping algorithm introduced in Section 3.3 and the proposed multiple-wavelength algorithm is also used. Figure 3.5 shows the cross-section of the object and Figure 3.6 shows the 3D reconstruct results.

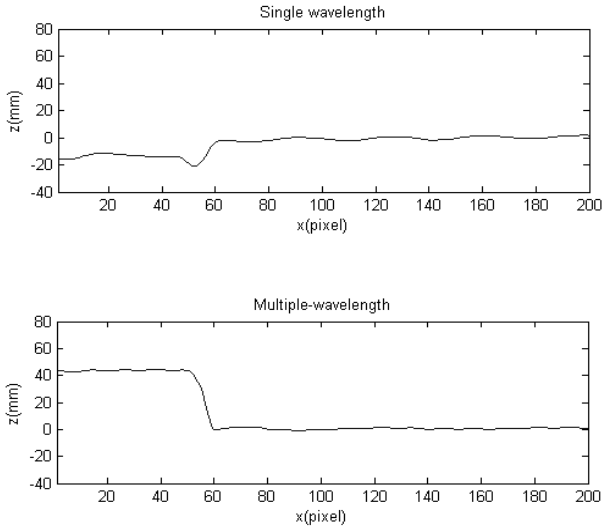

Figure 3.5 Cross-section of flat box

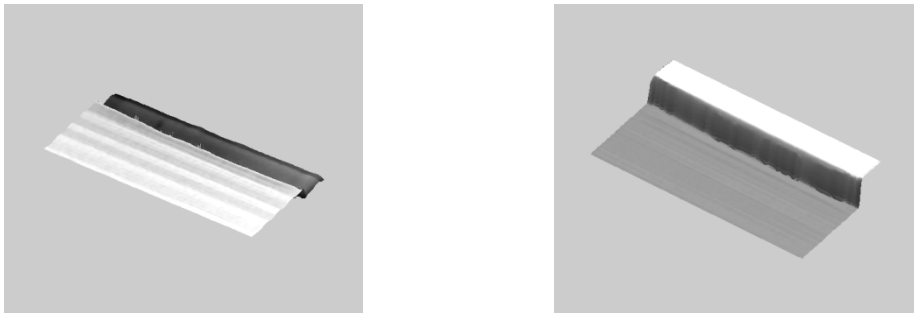

(a) (b)

Figure 3.6 3D reconstructed results of flat box: (a) result using a single wavelength algorithm and (b) result using a multiple-wavelength algorithm

From Figure 3.5 and Figure 3.6, it can be seen that the result obtained using the single wavelength algorithm is not correct because the box height result is about −17 mm. Using the multiple-wavelength algorithm, the step height was measured successfully, where the height result is about 43 mm. This experiment demonstrates that the proposed approach can successfully perform the measurement, even when the surface profile has a step.

The performance of the proposed method for the measurement of a mask characterised by a complex surface shape was then tested. In this experiment, a four-wavelength triangular-pattern spatial-shifting algorithm with $\lambda_1 = 480$ and N = 2 was used. Figure 3.7 (a) shows the mask, and Figures 3.7 (b) to (e) show the captured fringe images of the object with wavelengths $\lambda_1 = 480$, $\lambda_2 = 240$, $\lambda_3 = 120$, $\lambda_4 = 60$, respectively. The resolution of each captured fringe images is 225 × 300 pixels.

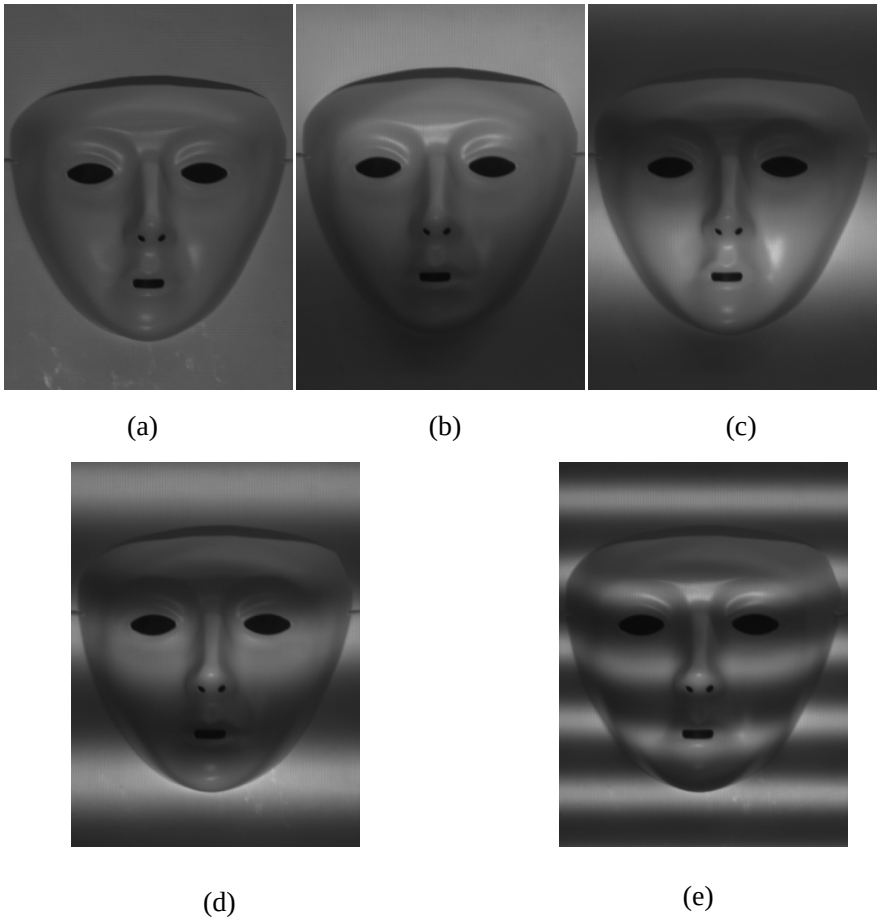

(a) (b) (c)

(d) (e)

Figure 3.7 Captured fringe images of mask with different wavelengths: (a) object, (b) fringes image ($\lambda = 480$), (c) fringes image ($\lambda = 240$), (d) fringes image ($\lambda = 120$) and (e) fringes image ($\lambda = 60$)

Figure 3.8 shows the reconstructed 3D surface shape of the object using the proposed unwrapping method. It can be seen that the mask is reconstructed successfully. The height information for those places with high step drop (mask edge, nose) is retrieved correctly. Some details, such as the mouth and eyes, are also recovered successfully. This result demonstrates that the proposed method can successfully measure complex objects with arbitrary step heights.

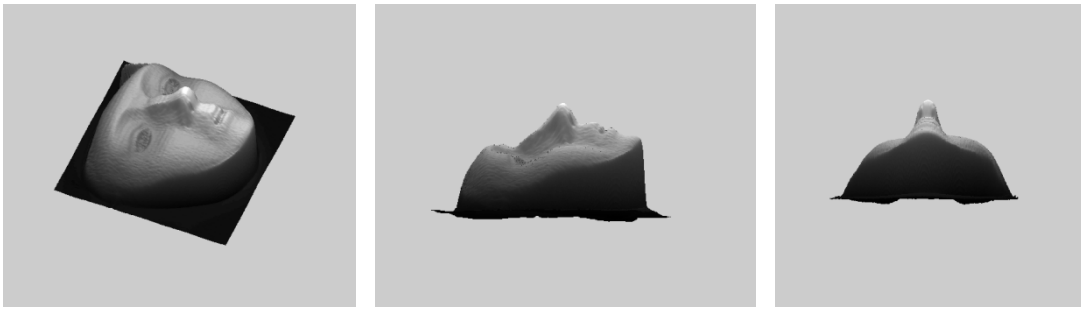

Figure 3.8 3D reconstructed results of mask

The proposed technique was also tested using another complex object, a plaster hand model. Figure 3.9 (a) shows the model, and Figures 3.9 (b) to (e) show the captured fringe images of object with different wavelengths. The resolution of each captured fringe images is 300 × 300 pixels.

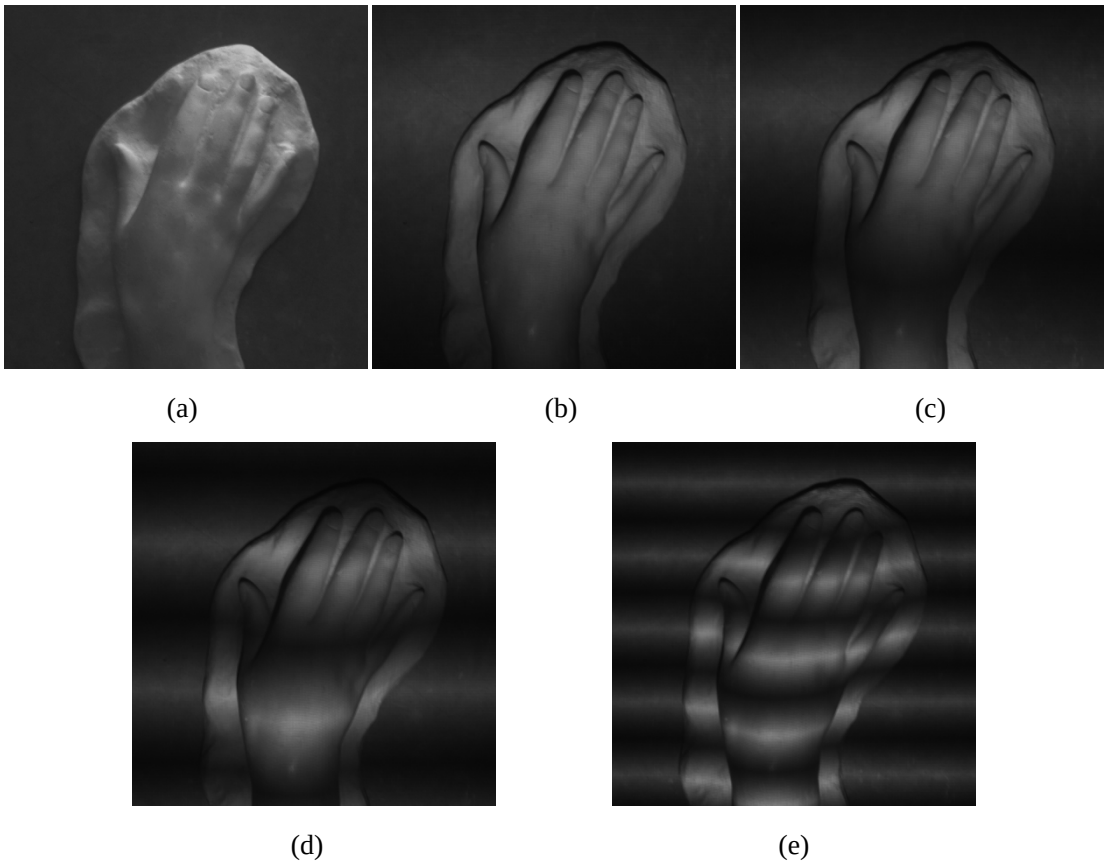

(a) (b) (c)

(d) (e)

Figure 3.9 Captured fringe images of hand model with different wavelengths: (a) object, (b) fringes image ($\lambda = 480$), (c) fringes image ($\lambda = 240$), (d) fringes image ($\lambda = 120$) and (e) fringes image ($\lambda = 60$)

Figure 3.10 depicts the reconstructed 3D surface shape of the hand model using the proposed unwrapping method. The model is successfully reconstructed in the measurement, which shows that the proposed method can be used for complex object surfaces with sudden height changes.

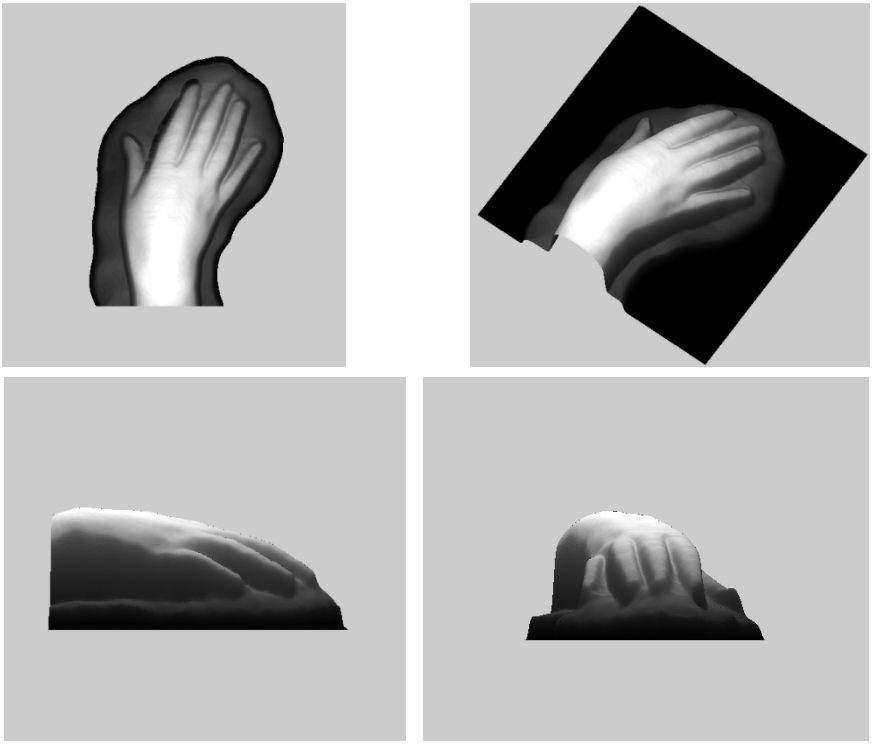

Figure 3.10 3D reconstruct results of hand model

3.5 Conclusions

In this chaper, the shift wrapping problem associated with SSE based FPP was discussed. Compared with PDE based approaches, SSE techniques are advantageous because non-sinusoidal fringe patterns can be employed, and they do not suffer from the nonlinear distortion associated with the DFP. However, as with the phase unwrapping problem encountered in PDE-based approaches, a shift unwrapping problem also exists in SSE-based approaches. The problem arises as the result of fringe reuse (i.e., fringes periodic light intensity variance), and the shift can only be identified without ambiguity

with the range of a fringe width. To solve this problem, a reliability-guided shift unwrapping algorithm that referred to the reliability-guided phase unwrapping algorithm used in conventional PDE-based FPP was first presented. The experimetal results show the effectiveness of the proposed unwrapping technique.

Although the proposed reliability-guided shift unwrapping algorithm works well, it still has a restriction where it is unable to unwrap the shift map if there are arbitrary step heights or isolated parts. Hence, another shift unwrapping technique to overcome this limitation was presented, which was based on the method proposed by Zhang [69] for phase unwrapping. To test the performance of proposed method, experiments were carried out on three objects that have arbitrary step heights and complex surface shapes: a flat box, a mask and a plaster hand-model. The results show that the proposed method can be successfully used for measuring surfaces with arbitrary step height.

Chapter 4 A Novel 3D Shape Measurement Method based on Projection of Triangular Patterns

4.1 Introduction

As discussed in Chapter 3, a novel multiple-wavelength unwrapping algorithm for SSE approach is proposed. In this method, a series of fringe patterns with frequencies that increase by a constant factor are projected. The first image has only one fringe covering the whole measurement area (i.e., its frequency is 1), and the remaining images are characterised by their frequency increasing by a constant factor (or their wavelengths decreasing by a constant factor). For example, for unwrapping an image pattern with 16 fringes, at least 4 additional images are required to perform the unwrapping. The method is not suitable for fast 3D measurement because the number of image patterns can be large. Therefore, achieveing a reduction in the number of image patterns while maintaining the accuracy of shift unwrapping remains a challenging problem.

In this chapter, inspired by the method proposed for phase unwrapping by Ding, *et al*. [70, 71], a method for shift unwrapping based on projection of two fringe patterns with different spatial frequencies is introduced to address the problem of reducing the number of image patterns. A novel 3D shape measurement method is proposed based on projection of a set of triangular patterns with a higher frequency and a triangular pattern with a lower frequency. The former are used to yield a high-frequency shift map by the multi-step triangular-pattern profilometry method in Wu, *et al*. [90], and the latter is used to obtain a low-frequency shift map using the single-step triangular-pattern SSE algorithm. With the proposed method, the corresponding absolute shift maps can be retrieved, which enables the measurement of the profile of the object's surface. Compared with multiple-wavelength unwrapping algorithm for SSE approach, the number of image patterns is greatly reduced because only one additional image is used.

It should be noted that the selection of pairs of frequencies has the restriction that the two frequencies must be coprime. To address this problem, a selected-wavelength shift unwrapping algorithm is introduced, which uses the wavelength instead of the frequency. The selection of wavelengths has no restriction, thus the design of the image patterns can be more flexible.

This chapter is organised as follows. Section 4.2 gives a review of existing selected-frequency phase unwrapping algorithms and then introduces a method for unwrapping spatial shift maps of two fringe patterns with different frequencies. Based on this method, a novel 3D shape measurement approach that uses the projection of triangular patterns of two selected frequencies is proposed in Section 4.3. In this section, a brief review of the multiple-step triangular-pattern SSE algorithm is given. The principle of the proposed 3D shape measurement approach is then introduced, and a set of experimental results are presented to demonstrate performance of the method. Section 4.4 introduces an improved approach that uses wavelengths instead of frequencies, thereby removing the restriction on selected frequencies. The performance of this improved approach is then confirmed by experiments. Section 4.5 concludes this chapter.

4.2 Selected-frequency Shift Unwrapping Algorithm

4.2.1 A Review of Selected-frequency Phase Unwrapping Algorithm

In this section, a brief review of the selected-frequency phase unwrapping algorithm proposed by Ding *et al*. [70, 71] is given. In this method, two image patterns are projected onto the object's surface. Two normalised spatial frequencies, f_1 and f_2, are used to describe these two patterns, which are positive integer numbers representing the total number of fringes on the patterns. Assuming that $\phi_1(x)$ and $\phi_2(x)$ are the

retrieved wrapped phase maps, the absolute phase maps $\Phi_1(x)$ and $\Phi_2(x)$ can be obtained using Equation (3.2):

$$\Phi_i(x) = 2\pi m_i(x) + \phi_i(x), \qquad i = 1, 2 \tag{4.1}$$

From Equation (1.7), we can find the following relationship [69]:

$$f_2\Phi_1(x) = f_1\Phi_2(x) \tag{4.2}$$

Combining Equations (4.1) and (4.2) yields:

$$\frac{f_2\phi_1(x) - f_1\phi_2(x)}{2\pi} = m_2(x)\, f_1 - m_1(x)\, f_2 \tag{4.3}$$

Equation (4.3) reveals an interesting property that can be employed to determine $m_1(x)$ and $m_2(x)$. Because $m_1(x)$, $m_2(x)$, f_1 and f_2 are all intergers, the right-hand side of this equation will be an integer, and the left-hand side must also be the same integer. Because the left-hand side of the equation can be obtained from the wrapped phase maps $\phi_1(x)$ and $\phi_2(x)$, the integer for the right-hand side can be obtained based on the value of the left-hand side. If there is a unique mapping between all the possible values of the right-hand side to $m_1(x)$ and $m_2(x)$, then $m_1(x)$ and $m_2(x)$ can be retrieved.

After the analysis in Ding *et al*. [71], it has been proved that there existing a unique mapping from $[f_2\phi_1(x) - f_1\phi_2(x)]/2\pi$ to $m_1(x)$ and $m_2(x)$, if f_1 and f_2 are coprime. Hence the absolute phase maps can be retrieved by the following steps:

Step 1: Select two frequencies (f_1, f_2) and construct a mapping table, making sure that the table provides a unique mapping from $m_2(x)f_1 - m_1(x)f_2$ to $m_1(x)$ and $m_2(x)$. It should be noted that two selected frequencies must be coprime.

Step 2: Project two fringe patterns onto the object and acquire the two wrapped phase maps $\phi_1(x)$ and $\phi_2(x)$ using a phase detection algorithm.

Step 3: Calculate $[f_2\phi_1(x) - f_1\phi_2(x)]/2\pi$ by rounding its value to the closest integer, denoted as *M*. Using the mapping table derived in Step 1, find the row (or entry) whose value of $m_2(x)f_1 - m_1(x)f_2$ is the closest to *M*. Record the corresponding $m_1(x)$ and $m_2(x)$ in the same row.

Step 4: Using $m_1(x)$ and $m_2(x)$ obtained in Step 3, reconstruct the absolute phase maps by Equation (4.1).

4.2.2 A Novel Shift Unwrapping Algorithm based on Selected-frequency Method

4.2.2.1 The Proposed Algorithm

Based on Ding *et al.*'s method [70], a selected-frequency unwrapping algorithm for the SSE approach is introduced. In this algorithm, the measurement area has a resolution of *W* × *H*, and the normalised spatial frequencies of the two patterns are f_1 and f_2 respectively, which are positive integers representing the total number of fringes on the respective patterns. The corresponding wavelengths are $\lambda_1 = H / f_1$ and $\lambda_2 = H / f_2$. Combining this with Equation (3.4) yields the following:

$$U_i(x) = \frac{H}{f_i} m_i(x) + u_i(x), \qquad i = 1, 2 \tag{4.4}$$

Because $U(x)$ only depends on $h(x)$, d_0 and l_0. The two unwrapped shift functions should be same, that is, $U_2(x) = U_1(x) = U(x)$. Hence we have:

$$\frac{H}{f_1} m_1(x) + u_1(x) = \frac{H}{f_2} m_2(x) + u_2(x) \tag{4.5}$$

or

$$\frac{f_1 f_2}{H}[u_1(x) - u_2(x)] = m_2(x) f_1 - m_1(x) f_2 \tag{4.6}$$

Using the similar reasoning to that in Ding *et al.* [70], we are able to derive a unique mapping from $U(x)$ to $m_1(x)$ and $m_2(x)$, as follows:

$$m_1(x) = \begin{cases} f_1 - 1 & \frac{(f_1 - 1)H}{f_1} \le U(x) < H \\ \cdots & \cdots \\ 2 & \frac{2H}{f_1} \le U(x) < \frac{3H}{f_1} \\ 1 & \frac{H}{f_1} \le U(x) < \frac{2H}{f_1} \\ 0 & 0 \le U(x) < \frac{H}{f_1} \end{cases} \tag{4.7}$$

and

$$m_2(x) = \begin{cases} f_2 - 1 & \frac{(f_2 - 1)H}{f_2} \le U(x) < H \\ \cdots & \cdots \\ 2 & \frac{2H}{f_2} \le U(x) < \frac{3H}{f_2} \\ 1 & \frac{H}{f_2} \le U(x) < \frac{2H}{f_2} \\ 0 & 0 \le U(x) < \frac{H}{f_2} \end{cases} \tag{4.8}$$

Combining the right hand side of Equations (4.7) and (4.8), the whole range [0, *H*] can be divided into $f_1 + f_2$ segments. Using the same approach as in Ding *et al*. [70], we can show that each segment corresponds to different values of $m_2(x) f_1 - m_1(x) f_2$ as well as different combinations of $m_1(x)$ and $m_2(x)$. Therefore, a table can be generated to form a unique mapping from $m_2(x) f_1 - m_1(x) f_2$ to $m_1(x)$ and $m_2(x)$.

Because $f_1 f_2 [u_1(x) - u_2(x)] / H = m_2(x) f_1 - m_1(x) f_2$, we can uniquely determine $m_1(x)$ and $m_2(x)$ from the value of $f_1 f_2 [u_1(x) - u_2(x)] / H$. Let us choose $f_1 = 5$ and $f_2 = 8$, the mapping relationship is shown in Table 4.1.

Table 4.1 Mapping from $m_2(x) f_1 - m_1(x) f_2$ to $m_1(x)$ and $m_2(x)$

$m_2(x) f_1 - m_1(x) f_2$	$m_1(x)$, $m_2(x)$	$m_2(x) f_1 - m_1(x) f_2$	$m_1(x)$, $m_2(x)$
7	1, 3	1	3, 5
6	3, 6	0	0, 0
5	0, 1	−1	2, 3
4	2, 4	−2	4, 6
3	4, 7	−3	1, 1
2	1, 2	−4	3, 4

From the above results we can reconstruct the absolute shift maps of the two fringe patterns using the following steps.

Step 1: Select two frequencies (f_1, f_2) and construct a mapping table, making sure that the table provides a unique mapping from $m_2(x)f_1 - m_1(x)f_2$ to $m_1(x)$ and $m_2(x)$.

Step 2: Project two fringe patterns onto the object and acquire the two shift distance maps $u_1(x)$ and $u_2(x)$ by a spatial estimation algorithm.

Step 3: Calculate $f_1 f_2[u_1(x) - u_2(x)]/H$ by rounding its value to the closest integer, denoted as *M*. Using the lookup table derived in Step 1, find the row (or entry) whose value of $m_2(x)f_1 - m_1(x)f_2$ is the closest to *M*. Record the corresponding $m_1(x)$ and $m_2(x)$ in the same row.

Step 4: Using $m_1(x)$ and $m_2(x)$ obtained in Step 3, reconstruct the absolute shift maps $U(x)$ using Equation (4.4).

The unwrapped shift map is retrieved point by point, and compared with algorithms that use neighbouring pixels to do the unwrapping, the method proposed here can measure a surface profile that has larger steps or multiple separate objects.

4.2.2.2 Frequency Pair Selection

From the previous section, we know that the validity of the proposed approach relies on the existence of a unique mapping from $m_2(x)f_1 - m_1(x)f_2$ to $m_1(x)$ and $m_2(x)$. This requires that both sides of Equation (4.6) must not yield the same value for any two values of *x*, such as x_a, x_b (a ≠ b). In other words, the following must hold:

$$\frac{f_1 f_2}{H}\left[u_1(x_a) - u_2(x_a)\right] \neq \frac{f_1 f_2}{H}\left[u_1(x_b) - u_2(x_b)\right] \qquad \text{or}$$

$$m_2(x_a) f_1 - m_1(x_a) f_2 \neq m_2(x_b) f_1 - m_1(x_b) f_2 \qquad \text{for} \quad x_a \neq x_b . \tag{4.9}$$

The above can be proved by *reductio ad absurdum*. Let us first discuss the simpler case where f_1 and f_2 are coprime. There exist three possible scenarios making the two pairs of $(m_1(x), m_2(x))$ different: (a) $m_1(x_a) \neq m_1(x_b)$ and $m_2(x_a) \neq m_2(x_b)$, (b) $m_1(x_a) \neq m_1(x_b)$ and $m_2(x_a) = m_2(x_b)$, and (c) $m_1(x_a) = m_1(x_b)$ and $m_2(x_a) \neq m_2(x_b)$. Without a loss of generality, let us discuss case (a). Assume that the following is valid:

$$m_2(x_a) f_1 - m_1(x_a) f_2 = m_2(x_b) f_1 - m_1(x_b) f_2 \tag{4.10}$$

This equation can be rewritten as:

$$\frac{m_1(x_a) - m_1(x_b)}{m_2(x_a) - m_2(x_b)} = \frac{f_1}{f_2} \tag{4.11}$$

Because f_1 and f_2 are coprime, Equation (4.11) must be equivalent to the following:

$$m_1(x_a) - m_1(x_b) = k f_1 \quad \text{and} \quad m_2(x_a) - m_2(x_b) = k f_2 \tag{4.12}$$

where k is an integer and $k \neq 0$.

From Equations (4.7) and (4.8), we have the ranges of $m_1(x)$ and $m_2(x)$: $0 \leq m_1(x_a) \leq f_1 - 1$, $0 \leq m_1(x_b) \leq f_1 - 1$, $0 \leq m_2(x_a) \leq f_2 - 1$ and $0 \leq m_2(x_b) \leq f_2 - 1$, so:

$$-(f_1 - 1) \leq m_1(x_a) - m_1(x_b) \leq (f_1 - 1) \quad \text{and} \quad -(f_2 - 1) \leq m_2(x_a) - m_2(x_b) \leq (f_2 - 1) \tag{4.13}$$

Comparing Equation (4.12) with Equation (4.13), it is obvious that $-1 < k < 1$ (i.e., $k = 0$), which contradicts the fact that $k \neq 0$. Hence, Equation (4.10) will not be true for the case (a). Thus we have:

$$m_2(x_a) f_1 - m_1(x_a) f_2 \neq m_2(x_b) f_1 - m_1(x_b) f_2 \tag{4.14}$$

In the same way, we can prove that Equation (4.14) holds for the other two cases.

We then consider the case where f_1 and f_2 are not coprime. If we let n be the greatest common divisor (g. c. m.) of f_1 and f_2, we have $f_1 = ng_1$ and $f_2 = ng_2$, where g_1 and g_2 are positive integers that are coprime. Hence, Equation (4.11) can be rewritten as:

$$\frac{m_1(x_a) - m_1(x_b)}{m_2(x_a) - m_2(x_b)} = \frac{g_1}{g_2} \tag{4.15}$$

Because g_1 and g_2 are coprime, Equation (4.15) must be equivalent to the following:

$$m_1(x_a) - m_1(x_b) = kg_1 \text{ and } m_2(x_a) - m_2(x_b) = kg_2 \tag{4.16}$$

Comparing Equation (4.16) with Equation (4.13), it is obvious that $-n < k < n$. Because $n > 1$, there exists an integer k ($k \neq 0$) that satisfies Equation (4.15). Hence, Equation (4.10) will be true, which proves that there is no unique mapping from $m_2(x) f_1 - m_1(x) f_2$ to $m_1(x)$ and $m_2(x)$.

Combining the analyses above, we conclude that only if f_1 and f_2 are coprime, there exists a unique mapping from $m_2(x) f_1 - m_1(x) f_2$ to $m_1(x)$ and $m_2(x)$ that will

enable us to determine $(m_1(x), m_2(x))$ to recover the two absolute shift maps using the proposed method.

4.2.2.3 Shift Error Bound

In Section 4.2.2.1, after calculating $f_1 f_2 [u_1(x) - u_2(x)] / H$, we need to round its value to the closest integer to find the corresponding $m_1(x)$ and $m_2(x)$. However, a problem with this method is that the arithmetic rounding operation has a high potential to introduce errors when $u_1(x)$ and $u_2(x)$ is corrupted by unwanted noise or distortion. If these errors occur, the lookup table will return incorrect values and introduce error in the retrieved absolute shift map. The anti-error capability of the proposed approach is studied in this section.

From Equation (4.6), we know that the values of $f_1 f_2 [u_1(x) - u_2(x)] / H$ are all integers, that is, the minimum gap between the values of $f_1 f_2 [u_1(x) - u_2(x)] / H$ is 1.

If an error in $f_1 f_2 [u_1(x) - u_2(x)] / H$ exceeds 0.5, the rounding operation will return the incorrect value. Error in $f_1 f_2 [u_1(x) - u_2(x)] / H$ must not exceed 0.5 if we want to round $f_1 f_2 [u_1(x) - u_2(x)] / H$ into the correct integer. Assuming shift errors in the wrapped shift maps $u_1(x)$ and $u_2(x)$ are $\Delta u_1(x)$ and $\Delta u_2(x)$ respectively, we have:

$$\frac{f_1 f_2}{H} [\Delta u_1(x) - \Delta u_2(x)] < 0.5 \tag{4.17}$$

Let $\Delta u_{\max} = \max(|\Delta u_1(x)|, |\Delta u_2(x)|)$, from Equation (4.17) we can find the upper bound of the allowable shift error:

$$0 \le \Delta u_{\max} < \frac{0.25H}{f_1 f_2} \tag{4.18}$$

In practice, if the error satisfies $0 \le \Delta u_1(x) < \frac{0.25H}{f_1 f_2}$ and $0 \le \Delta u_2(x) < \frac{0.25H}{f_1 f_2}$, the proposed method can be used correctly.

4.3 3D Shape Measurement based on Projection of Triangular Patterns of Two Selected Frequencies

In Section 4.2, a selected-frequency shift unwrapping technique was presented for solving the problem of shift wrapping associated with SSE-based FPP. In this technique, two wrapped shift functions $u_1(x)$ and $u_2(x)$ are required. These wrapped shift functions can be retrieved by the SSE algorithm. In Section 2.5, a single-step triangular-pattern SSE algorithm was introduced. The proposed approach is based on the projection of a single fringe pattern, and although this approach can improve efficiency in terms of the computational burden required for 3D measurement, the measurement accuracy is not as high as for the approaches using multiple images. Recently, Wu *et al*. [90] introduced a multiple-step triangular-pattern SSE algorithm by combining IFSE with the multiple-step triangular-pattern phase shifting algorithm [91 - 93], which greatly improves the accuracy of measurement.

Based on this technique, a novel 3D shape measurement method that combines single-step and multiple-step triangular-pattern SSE algorithms is proposed. In this method, triangular patterns of two different spatial frequencies are projected. The higher frequency patterns are used to implement the FPP, and the lower frequency pattern is used for shift unwrapping. The proposed method is able to solve the shift unwrapping problem associated with the existing multi-step triangular-pattern FPP by the projection of an additional fringe pattern.

4.3.1 A Review of Multiple-step Triangular-pattern SSE Algorithm

In this section, a review of the multiple-step triangular-pattern SSE algorithm is first given. In Chapter 2, a single-step triangular-pattern SSE algorithm was introduced. However, in practice, the single fringe pattern still suffers from the influence of background illumination. To solve this problem, multiple-step triangular patterns are used. Assuming the intensity function of the captured *N* fringe patterns are denoted by $I_n(x)$ $(n=1,2,\ldots,N)$. $I_1(x)$ contains triangular fringes with period *T* (or pitch) and other patterns are formed by shifting $I_1(x)$ along *x* by an integer multiple of *T*/*N*, that is, $I_n(x)=I_1(x-(nT/N))$. In the case of two-step triangular patterns, $I_1(x)$ and $I_2(x)$ are shown in Figure 4.1, where $I_{\max}$ and $I_{\min}$ are the maximum and minimum intensities and $I_{\min}$ can be considered to be the background illumination. $r_0(x)$ is defined as intensity ratio, which can be calculated by:

$$r_0(x)=\frac{\left|I_1(x)-I_2(x)\right|}{I_v} \tag{4.19}$$

where $I_v=I_{\max}-I_{\min}$.

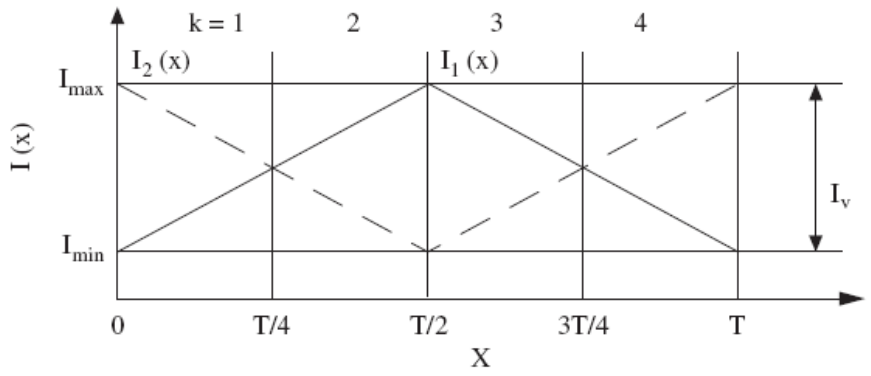

(a)

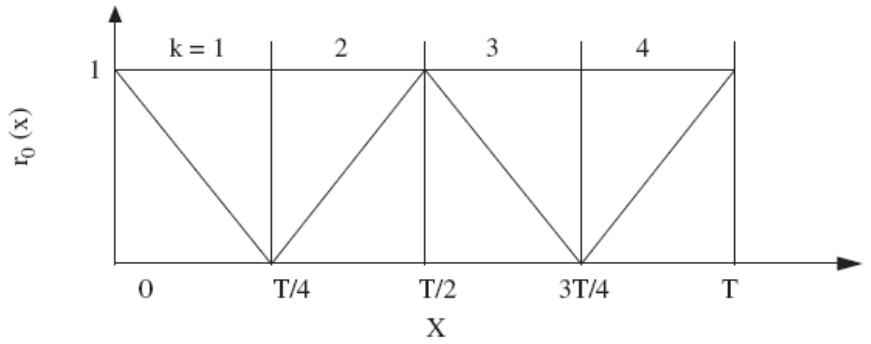

(b)

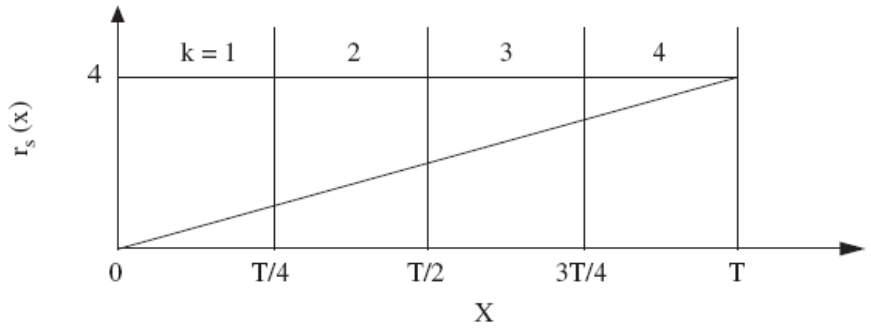

(c)

Figure 4.1 Intensity ratio calculations for two-step triangular-pattern method: (a) cross-section of two triangular patterns shifted by half of the fringe period, (b) cross-section of triangular shape intensity ratio and (c) cross-section of intensity ratio after removal of triangles

From Figure 4.1 (b), it is easy to find that $r_0(x)$ has the triangular shape ranging from 0 to 1, and it does not contain $I_{\max}$ and $I_{\min}$, implying that $r_0(x)$ is not influenced by background illumination. Because $r_0(x)$ has the period $T/2$, the following is used to yield an intensity ratio with the period T:

$$r_s(x) = (-1)^k r_0(x) + 2 \times round(\frac{k}{2}) - 1, \quad k = 1, 2, 3, 4 \tag{4.20}$$

where k is referred to as the region number, by which each fringe period T is divided into four equally spaced segments. It should be noted that $r_s(x)$ is from the reference plane. The intensity ratio from the object plane, denoted as $r_d(x)$, can be obtained from the reflected fringe patterns from the object with the same operations. Because the intensity ratios are the linear function of the fringe patterns, based on the superposition principle, it must have

$$r_d(x) = r_s(x - u(\mathrm{x})) \tag{4.21}$$

Hence, the shift function $u(x)$ can be retrieved as follows:

$$u(x) = x - r_s^{-1}(r_d(x)) \tag{4.22}$$

As shown in Figure 4.1 (c), $r_s(x)$ is a saw-tooth function. Even when it is deformed by the nonlinear distortion inherent in digital projection, it is still a monotonic function and, therefore, its inverse function exists. This method can also be used for the multiple-step triangular-pattern algorithm [90].

The multiple-step triangular-pattern SSE algorithm can be considered to be a combination of IFSE and the multiple-step triangular-pattern phase shifting algorithm [91 - 93]. Compared with the single-step triangular-pattern SSE algorithm, the measurement accuracy is greatly improved due to the use of multiple patterns. Also compared with the existing intensity ratio based techniques [91 - 93], the method proposed in Wu *et al*. [90] does not suffer from the influence of nonlinear distortion.

4.3.2 A Novel 3D Shape Measurement Method using Projection of Triangular Patterns of Two Selected Frequencies

In this section, a novel 3D shape measurement method based on the projection of triangular patterns of two selected frequencies is proposed. Because both $m_1(x)$ and $m_2(x)$ can be used to reconstruct the absolute shift maps, we can select the one with the lower measurement noise. Usually, the higher the spatial frequency used, the smaller the noise induced. We will project a set of triangular patterns with a higher frequency, from which a shift map can be obtained using the multiple-step triangular-pattern SSE algorithm [90]. Then, a triangular pattern with a lower frequency is projected, and the shift map can be retrieved by the single-step triangular-pattern SSE algorithm. The absolute shift map of the higher frequency can be recovered using the method described in Section 4.2.2, which is then used to determine the 3D shape. The procedure of the 3D shape measurement can be described using the flow chart in Figure 4.2.

From the flow chart in Figure 4.2, we see that two different methods are used for retrieving the wrapped shift map. For the image pattern with higher frequency, the multiple-step triangular-pattern spatial-shifting algorithm is used. Here *N* is the number of images captured and depends on the steps of the algorithm. As in the method proposed by Wu *et al*. [90], at least two steps are required, and the measurement accuracy can be improved by increasing the number of the spatial-shift steps. On the other side of the flow chart, the single-step triangular-pattern spatial-shifting algorithm is applied for the image pattern with the lower frequency and requires only a single image pattern.

It can be seen from the flow chart in Figure 4.2 that compared with the existing single frequency multiple-step triangular-pattern spatial-shifting algorithm, the proposed method requires only one additional image pattern to be projected. This is much more

efficient in terms of the number of fringe patterns required in contrast with the multiple-wavelength shift unwrapping method introduced in Section 3.4.

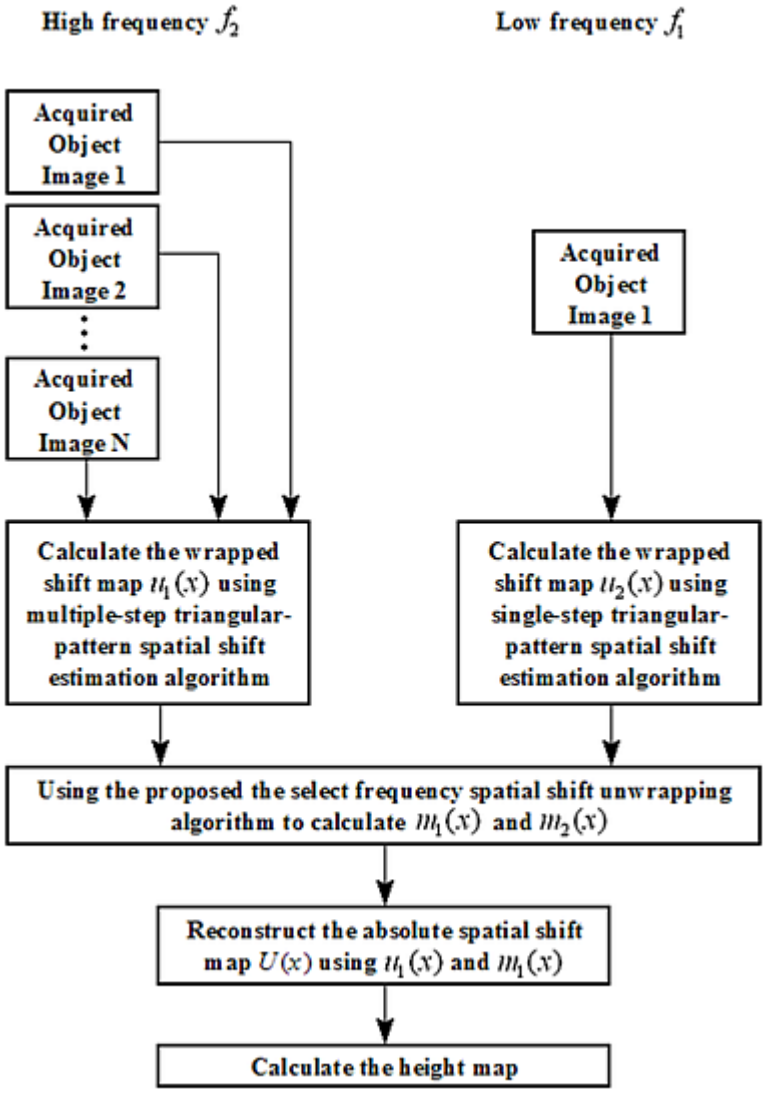

Figure 4.2 Flow chart of the proposed method

It should be pointed out that the information of object surface is all retrieved from the image pattern with higher frequency. The image pattern with the lower frequency is only used for solving the unwrapping problem, and it will not change the accuracy of the whole reconstruction. Thus the proposed method can receive the same accuracy as

Wu's method. As the measurement speed is depending on the number of images used, the measurement speed for the proposed method can be much closed to the method introduced by Wu, because only one additional image is added. Compared with the proposed multiple-wavelength unwrapping algorithm for the SSE approach in Section 3.4.2, the measurement speed will greatly increased, because less number of images is required.

4.3.3 Experiments and Results

To test the performance of the approach proposed in the previous section, experiments were carried out in the laboratory. The experimental set-up was the same as in Chapters 2 and 3. To verify that the proposed method can measure the profile of a surface with arbitrary step height, a flat box 84 mm high was first chosen as the measured object. Figure 4.3 (a) shows a photograph of the object. Figure 4.3 (b) shows the captured fringe image of the object with spatial frequency $f = 5$. Figures 4.3 (c) to (f) show the captured 4-step fringe images of the object with spatial frequency $f = 8$. The resolution of each captured fringe images is 150 × 200 pixels.

We first use a single frequency multiple-step triangular-pattern spatial shifting algorithm to reconstruct this object. The 4-step fringe images with normalised spatial frequency $f = 8$ are used. The wrapped $u(x)$ is retrieved using the multiple-step triangular-pattern SSE algorithm, and it is unwrapped using the reliability-guided shift unwrapping algorithm introduced in Section 3.3. As a comparison, the proposed method is also used. An additional fringe image with normalised spatial frequency $f = 5$ is captured, and the wrapped $u(x)$ is retrieved using the single-step triangular-pattern SSE algorithm. Figure 4.4 shows the cross-section of the object and Figure 4.5 shows the 3D reconstructed results.

Figure 4.4 (a) and Figure 4.5 (a) show that if we only use higher frequency patterns, the object's step height is measured as about 24 mm, which is obviously incorrect given the true value of 84 mm. However, with the proposed method, the step height can be measured accurately, with the result very close to 84 mm. This experiment demonstrates that the proposed approach can successfully perform the measurement, even when the surface profile has a large step.

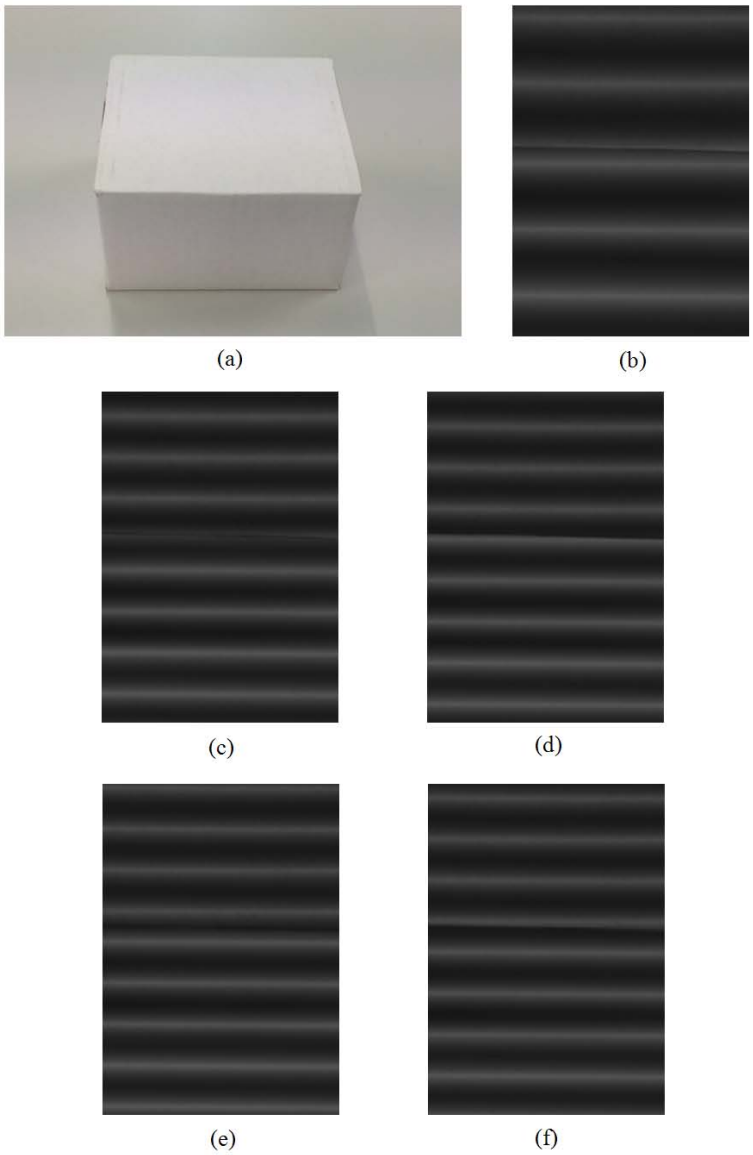

Figure 4.3 Captured fringe images of flat box: (a) object, (b) fringe image ($f = 5$) and (c) to (f) fringe images ($f = 8$)

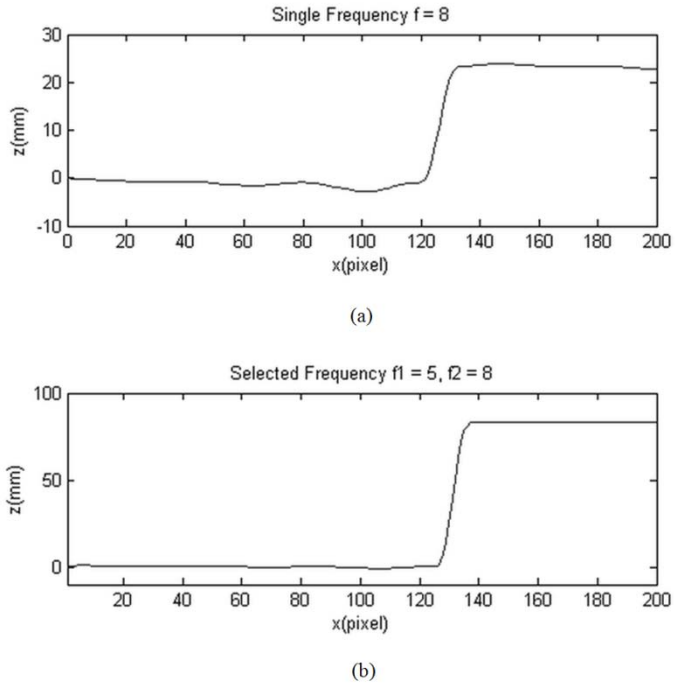

Figure 4.4 Cross-section of flat box: (a) result using single frequency algorithm (f = 8) and (b) result using select frequency algorithm (f_1 = 5, f_2 = 8)

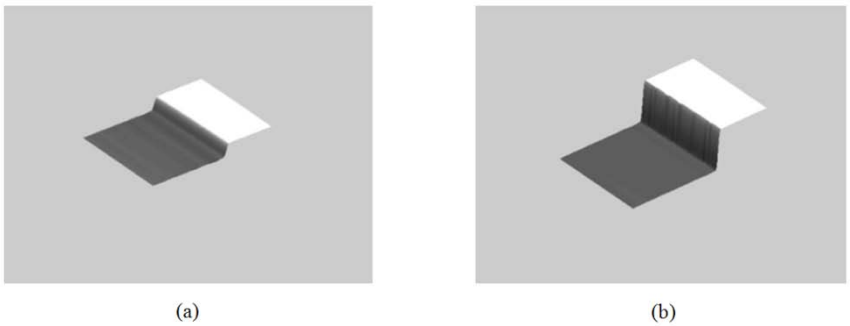

Figure 4.5 3D reconstructed results of flat box: (a) result using single frequency algorithm (f = 8) and (b) result using select frequency algorithm (f_1 = 5, f_2 = 8)

As discussed in Section 4.2.2, because the measurement is performed on a point-by-point basis, this technique can also be used to measure multiple separate objects or islands. To verify this, two separate objects were measured: a mask model and a plaster hand model. Both objects have complex surface shapes. The proposed method was used with two spatial frequencies $f_1 = 8$ and $f_2 = 13$ respectively. Two experiments were performed by fixing the higher frequency, but using a different number of steps (3 steps and 6 steps) for retrieving the wrapped $u(x)$. Figure 4.6 (a) shows the two objects and Figure 4.6 (b) shows the captured fringe images of the objects with frequency $f_1 = 8$. Figure 4.7 shows the captured images of the objects with 3-step triangular patterns with frequency $f_2 = 13$, and Figure 4.8 depicts the 6-step fringe images of objects with frequency $f_2 = 13$. The resolution of each captured fringe images is 540 × 312 pixels.

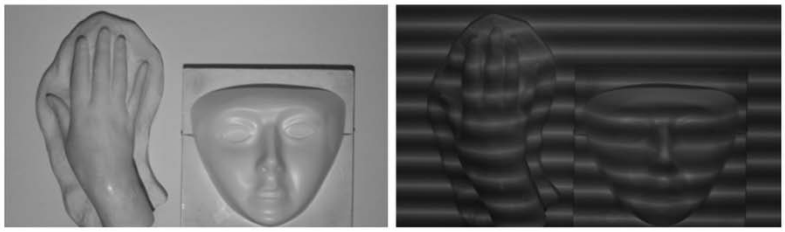

Figure 4.6 Captured fringe images of separate objects with different wavelengths. (a) objects and (b) fringes image ($f_1 = 8$)

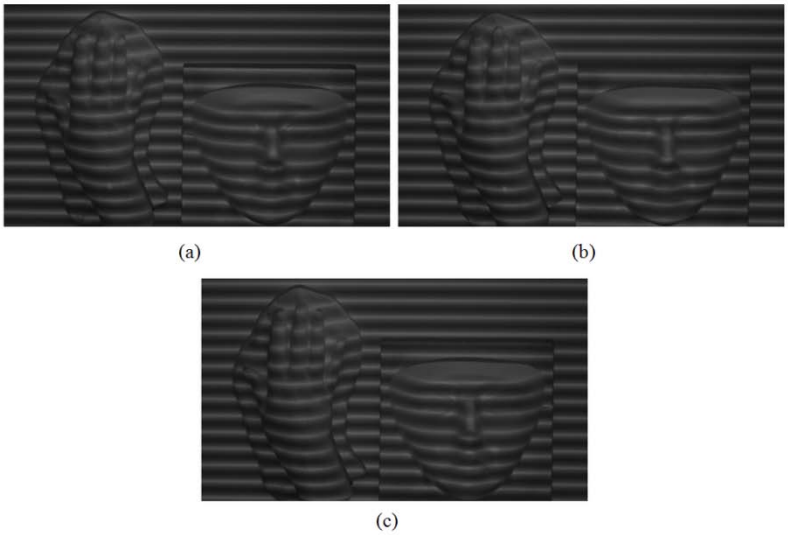

Figure 4.7 Captured 3-step fringe images of objects with $f_2 = 13$, where (a) to (c) are the fringe images in different steps

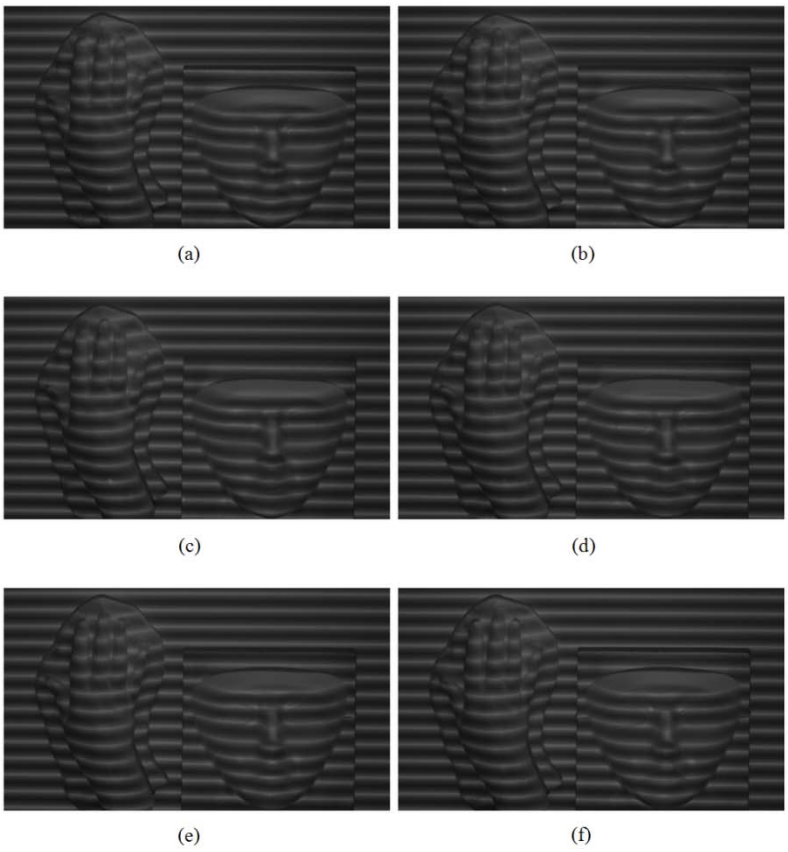

Figure 4.8 Captured 6-step fringe images of objects with $f_2 = 13$, where (a) to (f) are the fringe images in different steps

Figure 4.9 and Figure 4.10 show the reconstructed 3D surface shapes of the objects using the proposed unwrapping method, where Figure 4.9 shows the result using 3-step fringe images and Figure 4.10 gives the result using 6-step fringe images. The two separate objects are reconstructed successfully in both measurements. The height information at the places with high step drops (edge of mask, hand and nose) is retrieved correctly. Some details, such as the mouth and the eyes, are also recovered. This result demonstrates that the proposed method can successfully measure complex objects with arbitrary step height, even if the two objects are completely separate. The quality of the reconstructed model is improved with an increase in the number of steps for the higher frequency image.

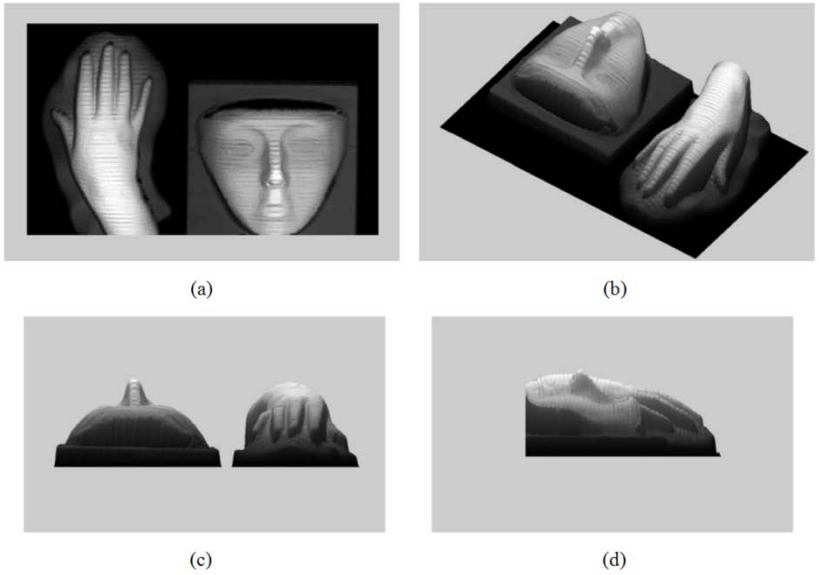

Figure 4.9 3D reconstructed results of two separate objects using 3-step fringe images, where (a) to (d) are the results in from different angles

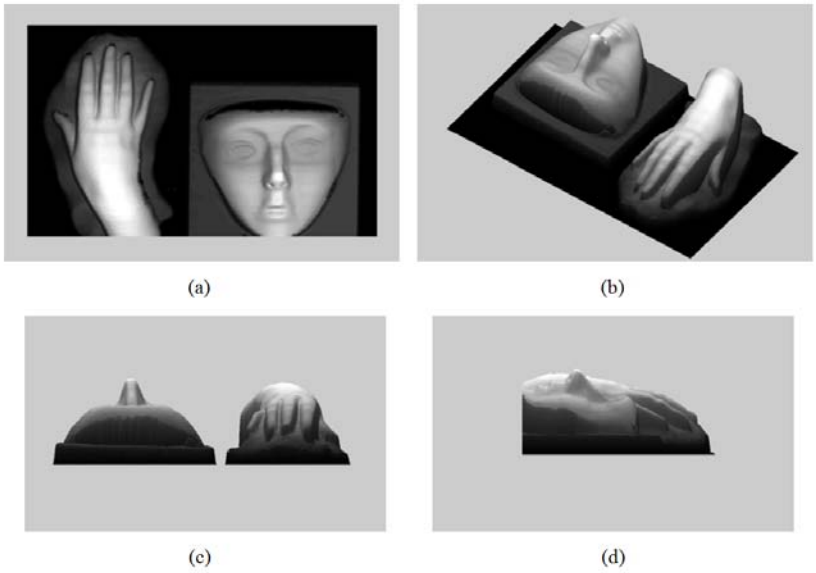

Figure 4.10 3D reconstructed results of two separated objects using 6-step fringe images, where (a) to (d) are results from different angles

The results above show that the proposed method works very well. Complex object surfaces with significant step heights or multiple separate objects can be measured successfully with the same accuracy as the method in Wu *et al*. [90]. Compare with the existing multiple-wavelength unwrapping algorithm for SSE approach, the number of image patterns required is greatly reduced.

4.4 3D Shape Measurement Based on Projection of Triangular Patterns of Two Selected Wavelengths

In Section 4.2, a selected-frequency shift unwrapping algorithm was introduced to solve the shift unwrapping problem associated with SSE. The principle for frequency pair selection and shift error bound for this algorithm was also given, where the selection of the frequency pair has the restriction that the two selected frequencies must be coprime. To meet such a requirement, the total number of pixels perpendicular to the fringe must be an integer multiple of the number of pixels within the fringe. However, such a

selection may not be possible in some cases. For example, if the measurement area is 800 × 600 pixels and the selected frequencies are $f_1 = 8$ and $f_2 = 13$, the numbers of pixels per fringe period will be about 75 and 46.1538, respectively, which are not integers and, therefore, are not implementable. In this section, the possibilities that the selected frequencies do not need to be integers is investigated, thus yielding more flexibility for the design of the patterns.

4.4.1 A Novel 3D Shape Measurement Method using Projection of Triangular Patterns of Two Selected Wavelengths

4.4.1.1 Selected-wavelength Shift Unwrapping Algorithm

From the algorithm given in Section 4.2.2, the most important step is the generation of the lookup table. Once the table is generated, the unwrapped shift map can be retrieved point-by-point. If the table can be generated without the the limitation of f_1 and f_2, selections can be more flexible.

To solve the problem, the algorithm is improved. In this method, the fringe wavelengths λ_1 and λ_2 are chosen to describe the two fringe patterns instead of using the two frequencies f_1 and f_2. Because $\lambda_1 = H / f_1$ and $\lambda_2 = H / f_2$, we can have this equation:

$$\frac{\lambda_1}{\lambda_2} = \frac{f_2}{f_1} \tag{4.23}$$

Because f_1 and f_2 are coprime, we can have $\lambda_1 = nf_2$ and $\lambda_2 = nf_1$, where *n* is the greatest common divisor (g. c. m.) of them. Hence, we can convert $H = \lambda_1 f_1 = \lambda_1 \lambda_2 / n$.

The following improved algorithm generates the table only using the wavelengths:

Step 1: Select two wavelengths (λ_1, λ_2) and find the greatest common divisor (g. c. m.) n of them, such that $\lambda_1 = ng_1$ and $\lambda_2 = ng_2$, where g_1 and g_2 are positive integers which are coprime.

Step 2: Use (g_2, g_1) to construct a mapping table, making sure that the table provides a unique mapping from $m_2(x)g_2 - m_1(x)g_1$ to $m_1(x)$ and $m_2(x)$.

Step 3: Project two fringe patterns onto the object and acquire the two shift distance maps $u_1(x)$ and $u_2(x)$ using a spatial estimation algorithm. Calculate $[u_1(x) - u_2(x)]/n$ by rounding its value to the closest integer, denoted as *M*. Using the lookup table derived in Step 2, find the row (or entry) whose value of $m_2(x)g_2 - m_1(x)g_1$ is the closest to *M*. Record the corresponding $m_1(x)$ and $m_2(x)$ in the same row.

Step 4: Using $m_1(x)$ and $m_2(x)$ obtained in Step 3, reconstruct the absolute shift maps $U(x)$ using Equation (3.4).

The generation of the lookup table only depends on two wavelengths (λ_1, λ_2), hence in this algorithm there is no limitation of measurement area *H* and frequency selections. Also from the algorithm, because the greatest common divisor (g. c. m.) *n* can be any value, there is no restriction on the selection of these two wavelengths (λ_1, λ_2) (such as they must be coprime). Thus, it can provide more flexibility in the design of the patterns.

4.4.1.2 Shift Error Bound

The shift error bound of this new algorithm is discussed in this section. In the previous section, $[u_1(x)-u_2(x)]/n$ needed to be rounded to the closest integer to find the corresponding $m_1(x)$ and $m_2(x)$. Hence, the arithmetic rounding operation still has a high potential to introduce errors when $u_1(x)$ and $u_2(x)$ are corrupted by unwanted noise or distortion. Using the same analysis as in Section 4.2.2.3, the minimum gap between the values of $[u_1(x)-u_2(x)]/n$ is 1, and if an error in $[u_1(x)-u_2(x)]/n$ exceeds 0.5, the rounding operation will return with an incorrect value. Assuming that the shift errors in the wrapped shift maps $u_1(x)$ and $u_2(x)$ are $\Delta u_1(x)$ and $\Delta u_2(x)$ respectively, we have:

$$\left[\Delta u_1(x)-\Delta u_2(x)\right]/n < 0.5 \tag{4.24}$$

Let $\Delta u_{\max} = \max(|\Delta u_1(x)|, |\Delta u_2(x)|)$, then from Equation (4.24) we can find the upper bound of the allowable shift error:

$$0 \le \Delta u_{\max} < 0.25n \tag{4.25}$$

In practice, if $0 \le \Delta u_1 < 0.25n$ and $0 \le \Delta u_2 < 0.25n$, the proposed method will work correctly.

4.4.2 Experiments and Results

Experiments were carried out to test the performance of the approach proposed in the previous section. In the first experiment, two separate objects, a horse and a human head sculpture, were used. Both objects have complex surface shapes. The proposed method was used with two wavelengths $\lambda_1 = 24$ and $\lambda_2 = 39$. Figure 4.11 (a) shows the two objects, and Figures 4.11 (b) and (c) show the captured fringe images of the

objects with wavelengths $\lambda_1 = 24$ and $\lambda_2 = 39$, respectively. The resolution of each captured fringe images is 590 × 360 pixels.

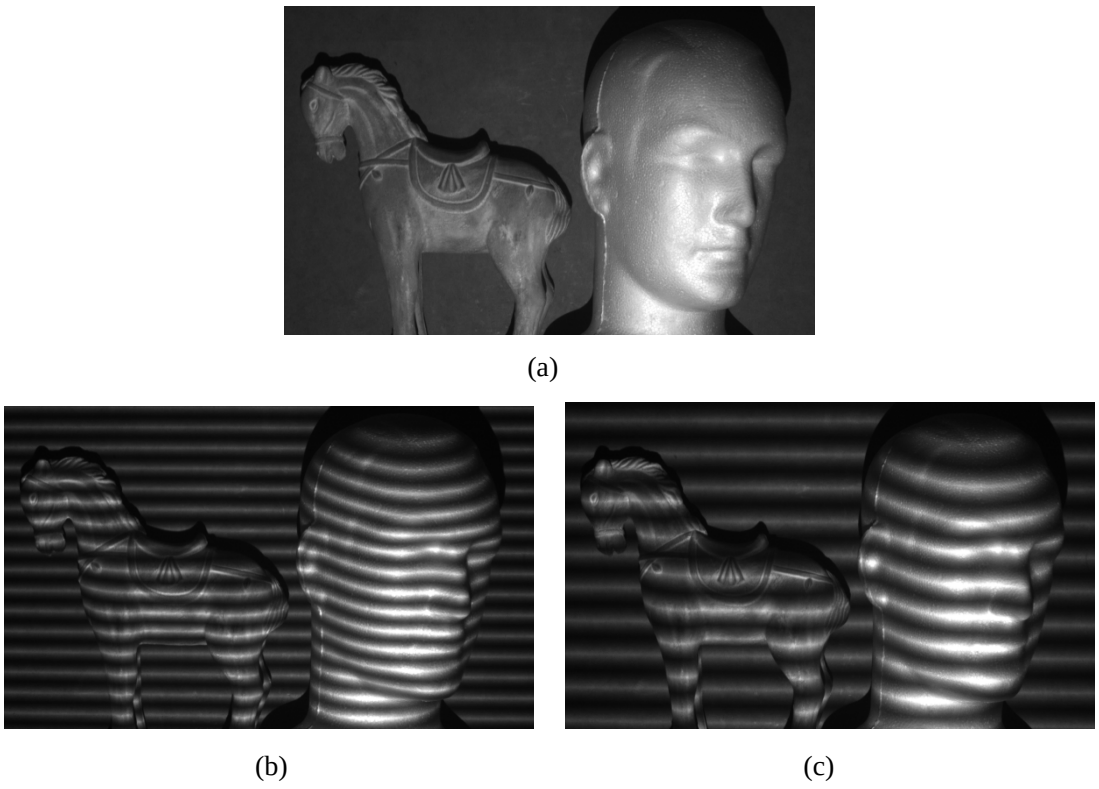

(a)

(b) (c)

Figure 4.11 Captured fringe images of separate objects with different wavelengths: (a) objects, (b) fringe image (λ= 24) and (c) fringe image (λ= 39)

From Figures 4.11 (b) and (c), we can find that the spatial frequencies for the fringe images are about 15 and 9.2, which are neither coprime nor integers. However, using the proposed selected-wavelength shift unwrapping algorithm, we can still perform unwrapping on these objects. Figure 4.12 shows the successfully reconstructed 3D surface shapes of the objects.

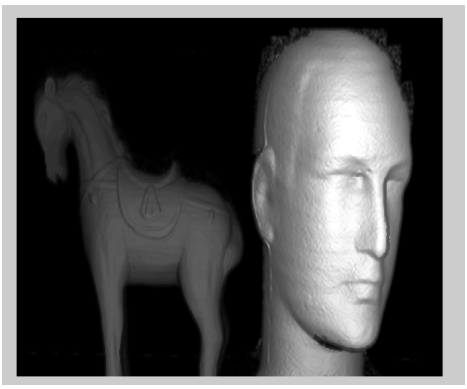

(a)

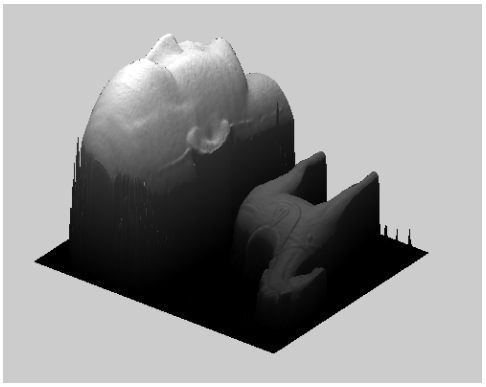

(b)

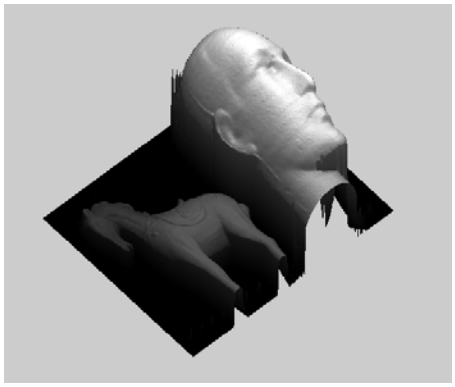

(c)

Figure 4.12 3D reconstruct results of two separated objects using 3-step fringe images, where (a) to (c) are the results in from different angles

Another experiment was performed, where two separate objects, the horse and a figure, were used as measurement objects. Both objects have complex surface shapes. In this experiment, the measurement area was changed but the wavelengths used were kept same; thus the spatial frequencies should be changed. Figure 4.13 (a) shows the two objects and Figures 4.13 (b) and (c) show the captured fringe images of the objects with wavelengths $\lambda_1 = 24$ and $\lambda_2 = 39$, respectively. The resolution of each captured fringe images is 590 × 390 pixels.

(a)

(b)

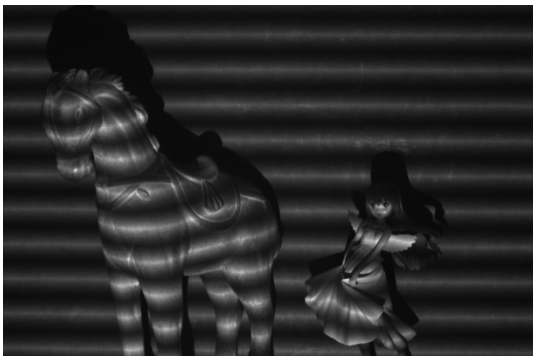

(c)

Figure 4.13 Captured fringe images of separate objects with different wavelengths: (a) objects,

(b) fringes image (λ= 24) and (c) fringes image (λ= 39)

From Figures 4.13 (b) and (c), we can calculate the spatial frequencies for the fringe images as about 16 and 10. The proposed selected-wavelength shift unwrapping algorithm was used to reconstruct the objects. Figure 4.14 shows the successfully reconstructed 3D surface shape of these objects.

(a)

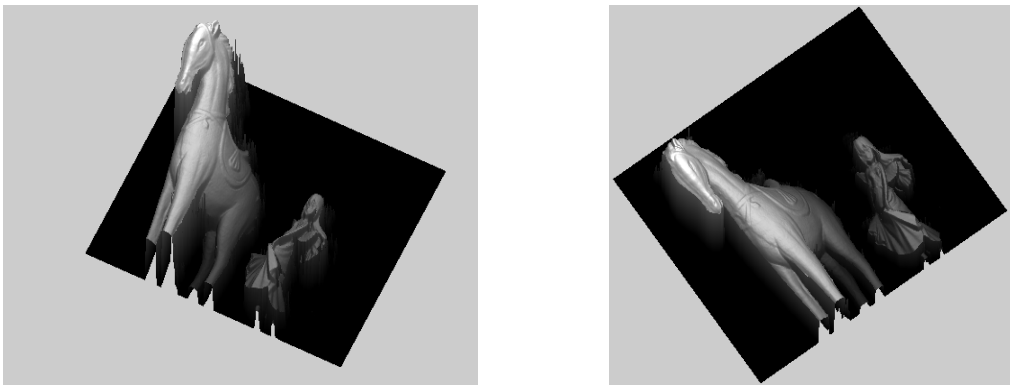

(b) (c)

Figure 4.14 3D reconstructed results of two separated objects using 3-step fringe images, where (a) to (c) are the results from different angles

4.5 Conclusions

In this chaper, a temporal shift unwrapping technique was presented for solving the problem of shift wrapping associated with SSE-based FPP. Based on this technique, a novel 3D shape measurement method was introduced. This method improves the existing multiple-step triangular-pattern SSE algorithm by the projection of only one additional image with a lower frequency. To test the performance of the proposed method, experiments were carried out on three different objects that have significant steps and complex surface shapes: a flat box, a mask, and a plaster hand-model. The results show that the proposed method works very well. Complex object surfaces with significant step heights or multiple separate objects can be measured successfully with the same accuracy as the method in Wu *et al*. [90]. Compared with the existing multiple-wavelength unwrapping algorithm for the SSE approach, the number of image patterns required is greatly reduced. The proposed method was further improved in this chapter, where the restriction on frequency selection was also removed. Experiments were carried out to verify that the improved method can provide more flexibility for the design of the patterns.

Chapter 5 Conclusions and Future Work

5.1 Conclusions

The main aim of this thesis is to implement the SSE approach for 3D profile measurement based on DFP. The research work includes reviewing the existing theories, performing the implementation based on these theories, and solving problems encountered in the practical experiments. In particular, three issues are considered in this thesis.

The first issue is discussed in Chapter 2. This provides details of the implementation of traditional SSE approaches for 3D profile measurement based on DFP and the improvement in efficiency using the SSE approach. A DFP system model based on the principle of FPP is presented. Using this system, the implementation of the SSE approach based on the SSE and IFSE theory is performed. However, problems that had not been mentioned in the literature occur during the implementation. Solutions are then developed to solve the problems, such as using a filter and fringe normalisation processing. An improved IFSE method is also introduced to reduce the computation time. The 3D model of an object's surface is reconstructed to show the performance of this implementation. In the remainder of Chapter 2, the limitations of using traditional sinusoidal fringe patterns as the projected fringe pattern is analysed. This includes vulnerability to geometric distortion and nonlinear intensity distortion, such as gamma distortion and high computational complexity in the IFSE method. To improve the efficiency, these limitations must be overcome. Because the SSE approach does not depend on the structure of the projected fringe pattern, an improved SSE approach using triangular fringe patterns instead of sinusoidal fringe patterns is proposed. The performance of the triangular fringe patterns is then demonstrated through analysis and experiments.

The second aspect considered in this thesis is to solve the shift unwrapping problem. As demonstrated in Chapter 3, a review of the phase unwrapping problem in conventional PDE-based FPP is presented. Based on this, a similar unwrapping problem exists in the SSE approach: the spatial shift unwrapping problem. To solve this problem, several methods are introduced in Chapter 3 and Chapter 4. These include the reliability-guided spatial shift unwrapping algorithm, multiple-wavelength spatial shift unwrapping algorithm, selected-frequency spatial shift unwrapping algorithm and selected-wavelength spatial shift unwrapping algorithm. These methods are described using graphs and mathematical expressions, with experimental results given to verify the effectiveness of the proposed spatial shift unwrapping techniques.

The last issue of interest to this thesis is the introduction of a novel 3D shape measurement method. In Chaper 4, the selected-frequency and selected-wavelength spatial shift unwrapping algorithms are proposed. Combining these methods with an existing multiple-step triangular-pattern SSE algorithm and the single-step triangular-pattern SSE algorithm, which is introduced in Chapter 2, a novel 3D shape measurement method is proposed. This method improves the existing multiple-step triangular-pattern SSE algorithm [90] by the projection of only one additional image with a lower frequency. To test the performance of the proposed method, experiments were carried out on several different objects that have significant steps and complex surface shapes. The results show that the proposed method works very well.

5.2 Suggestions for Future Research Work

Although the spatial shift detection approach for 3D profile measurement based on DFP have been successfully implemented, some issues still exist and require further research work.

The most important issue for future work is the camera coverage problem. In most

FPP approaches, only one camera is used to capture the fringe pattern. However, due to the field-of-view limit and optical occlusion effects of the camera, a traditional single-camera system is not suitable for the measurement of large-scale and complex objects. Also if we want to build a full 360° 3D image in future, multiple views are required. To solve this problem, two approaches are proposed. One approach is using single camera to capture multiple pictures of the object from different viewing directions [94 - 96]. However, this approach requires repeated translation of the camera and object to exact locations and orientations in space, which is time-consuming and prone to re-positioning errors. Another approach is using a multi-camera system, which is common in surface profilometry [97 - 100]. Although this method requires additional cameras, there is no need for translation of the camera and object to exact locations and orientations in space because the positions of both the camera and the object are fixed and it, therefore, has a significant reduction in processing time. All the approaches based on this method use stereo vision or a PDE-based approach. The design of a multi-camera system based on the SSE approach is still an issue. Because the SSE approach has many advantages in comparison with the conventional PDE approach, a SSE approach based multi-camera system can be designed to improve the measurement.

Another issue is the usage of colour fringes. Compared with the black and white image used in implementation here, the coloured image contains more object height information and thereby greatly increases data acquisition speed. For example, for a three-step triangular-pattern SSE algorithm, at least 3 images are required if the black and white image is used. However, for coloured image, only one image is enough because there are three different colour channels. Due to the fringe projection system designed here supports colour fringe projection, to effectively use colour in FPP is an attractive but challenging issue.

Finally, the experimental system should be improved to reduce the influence of

environmental factors, such as ambient light, to obtain more accurate results.

REFERENCES

[1] F. Chen, G. M. Brown, and M. Song, “Overview of three-dimensional shape measurement using optical methods,” *Optical Engineering*, vol. 39, no. 1, pp. 10–22, 2000.

[2] American Society of Photogrammetry, *Manual of Photogrammetry*, 4th ed. Falls Church, VA: American Society of Photogrammetry, 1980.

[3] U. R. Dhond and J. K. Aggarwal, “Structure from stereo – a review,” *IEEE Transactions on Systems, Man, and Cybernetics*, vol. 19, no. 6, pp. 1489–1510, 1989.

[4] M. Z. Brown, D. Burschka, and G. D. Hager, “Advances in computational stereo,” *IEEE Transactions on Pattern Analysis and Machine Intelligence*, vol. 25, no. 8, pp. 993–1008, 2003.

[5] R. Zhang, P. Tsai, J. E. Cryer, and M. Shah, “Shape from shading: A survey,” *IEEE Transactions on Pattern Analysis and Machine Intelligence*, vol. 21, no. 8, pp. 690–706, 1999.

[6] K. Kanatani and T. Chou, “Shape from texture: General principle,” *Artificical Intelligence*, vol. 38, no. 1, pp. 1–48, 1989.

[7] S. K. Nayar and Y. Nakagawa, “Shape from focus,” *IEEE Transactions on Pattern Analysis and Machine Intelligence*, vol. 16, no. 8, pp. 824–831, 1994.

[8] M. Subbarao and T. Choi, “Accurate recovery of three dimensional shape from image focus,” *IEEE Transactions on Pattern Analysis and Machine Intelligence*, vol. 17, no. 3, pp. 266–274, 1995.

[9] C. Polhemus, “Two-wavelength interferometry,” *Applied Optics*, vol. 12, no. 9, pp. 2071–2074, 1973.

[10] K. Creath, Y. Cheng, and J. C. Wyant, “Contouring aspheric surfaces using two-wavelength phase-shifting interferometry,” *Optica Acta*, vol. 32, no. 12, pp. 1455–1464, 1985.

[11] Y. Cheng and J. C. Wyant, “Multiple-wavelength phase-shift interferometry,” *Applied Optics*, vol. 24, no. 6, pp. 804–807, 1985.

[12] K. Haines and B. P. Hildebrand, “Contour generation by wavefront reconstruction,” *Physics Letters*, vol. 19, no. 1, pp. 10–11, 1965.

[13] J. S. Zelenka and J. R. Varner, “Multiple-index holographic contouring,” *Applied Optics*, vol. 8, no. 7, pp. 1431–1434, 1969.

[14] Y. Y. Hung, J. L. Turner, M. Tafralian, J. D. Hovanesian, and C. E. Taylor, “Optical method for measuring contour slopes of an object,” *Applied Optics*, vol. 17, no. 1, pp. 128–131, 1978.

[15] H. El-Ghandoor, “Tomographic investigation of the refractive index profiling using speckle photography technique,” *Optics Communications*, vol. 133, no. 1–6, pp. 33–38, 1997.

[16] N. Abramson, “Holographic contouring by translation,” *Applied Optics*, vol. 15, no. 4, pp. 1018–1022, 1976.

[17] R. Rodriguez-Vera, D. Kerr, and F. Mendoza-Santoyo, “Electronic speckle contouring,” *Journal of the Optical Society of America A*, vol. 9, no. 11, pp. 2000–2008, 1992.

[18] H. Takasaki, “Moiré topography,” *Applied Optics*, vol. 9, no. 6, pp. 1467–1472, 1970.

[19] R. Harding and R. Tait, “Moiré techniques applied to automated inspection of machined parts,” in *Proceedings of SME Vision ’86 Conference, Detroit, MI, June 3-5 1986*. Dearborn, MI: Machine Vision Association of SME, 1986.

[20] I. Moring, H. Ailisto, “Active 3-D vision system for automatic model-based shape inspection,” *Optics and Lasers in Engineering*, vol. 10, no. 3–4, pp. 149-160, 1989.

[21] J. S. Massa, G. S. Buller, A. C. Walker, S. Cova, M. Umasuthan, and A. M. Wallace, “Time-of-flight optical ranging system based on time correlated single-photon counting,” *Applied Optics*, vol. 37, no. 31, pp. 7298–7304, 1998.

[22] J. Batlle, E. Mouaddib, and J. Salvi, “Recent progress in coded structured light as a technique to solve the correspondence problem: A survey,” *Pattern Recoginition*, vol. 31, no. 7, pp. 963–982, 1998.

[23] J. Salvi, J. Pages, and J. Batlle, “Pattern codification strategies in structured light systems,” *Pattern Recoginition*, vol. 37, no. 4, pp. 827–849, 2004.

[24] Z. Ji and M. C. Leu, “Design of optical triangulation devices,” *Optics and Laser Technology*, vol. 21, no. 5, pp. 335–338, 1989.

[25] S. Gorthi and P. Rastogi, “Fringe projection techniques: whither we are?” *Optics and Lasers in Engineering*, vol. 48, no. 2, pp. 133–140, 2010.

[26] M. Takeda, H. Ina, and S. Kobayashi, “Fourier-transform method of fringe-pattern analysis for computer-based topography and interferometry,” *Journal of the Optical Society of America A*, vol. 72, no. 1, pp. 156–160, 1982.

[27] M. Takeda and K. Mutoh, “Fourier transform profilometry for the automatic measurement of 3-D object shapes,” *Applied Optics*, vol. 22, pp. 3977–3982, 1983.

[28] X. Su and W. Chen, “Fourier transform profilometry: A review,” *Optics and Lasers in Engineering*, vol. 35, no. 5, pp. 263–284, 2001.

[29] H. Zhang, M. J. Lalor, and D. R. Burton, “Spatiotemporal phase unwrapping for the measurement of discontinuous objects in dynamic fringe-projection phase-shifting profilometry,” *Applied Optics*, vol. 38, no. 16, pp. 3534–3541, 1999.

[30] M. Halioua and H. C. Liu, “Optical three-dimensional sensing by phase measuring profilometry,” *Optics and Lasers in Engineering*, vol. 11, no. 3, pp.185–215, 1989.

[31] J. Li, H. Su, and X. Su, “Two-frequency grating used in phase-measuring profilometry,” *Applied Optics*, vol. 36, no. 1, pp. 277–280, 1997.

[32] Y. Fu and Q. Luo, “Fringe projection profilometry based on a novel phase shift method,” *Optics Express*, vol. 19, no. 22, pp. 21739–21747, 2011.

[33] S. Toyooka and M. Tominga, “Spatial fringe scanning for optical phase measurement,” *Optics Communications*, vol. 51, no. 2, pp. 68–70, 1984.

[34] S. Toyooka and Y. Iwaasa, “Automatic profilometry of 3-D diffuse objects by spatial phase detection,” *Applied Optics*, vol. 25, no. 10, pp. 1630–1633, 1986.

[35] R. Rodriguez-Vera and M. Servin, “Phase locked loop profilometry,” *Optics and Lasers Technology*, vol. 26, no. 6, pp. 393–398, 1994.

[36] D. M. Meadows, W. O. Johnson, and J. B. Allen, “Generation of surface contours by moiré patterns,” *Applied Optics*, vol. 9, no. 4, pp. 942–947, 1970.

[37] A. Asundi and Z. Wensen, “Unified calibration technique and its applications in optical triangular profilometry,” *Applied Optics*, vol. 38, no. 16, pp. 3556–3561, 1999.

[38] C. Wust and D. W. Capson, “Surface profile measurement using color fringe projection,” *Machine Vision and Applications*, vol. 4, pp. 193–203, 1991.

[39] P. Huang, Q. Ho, F. Jin, and F. Chiang, “Colour-enhanced digital fringe projection technique for high-speed 3-D surface contouring,” *Optical Engineering*, vol. 38, no. 6, pp. 1065–1071, 1999.

[40] Z. Zhang, C. E. Towers, and D. P. Towers, “Robust color and shape measurement of full color artifacts by RGB fringe projection,” *Optical Engineering*, vol. 51, no. 2, p. 021109, 2012.

[41] J. Guo, X. Peng, J. Yu, X. Liu, A. Li, and M. Wang, “Real-time 3D imaging by using color structured light based on Hilbert transform,” *Proceeding of SPIE*, vol. 8856, pp. 885624, 2013.

[42] A. J. Moore and F. Mendoza-Santoyo, “Phase demodulation in the space domain without a fringe carrier,” *Optics and Lasers in Engineering*, vol. 23, no. 5, pp. 319–330, 1995.

[43] J. Villa, M. Servin, and L. Castillo, “Profilometry for the measurement of 3-D object shapes based on regularized filters,” *Optics Communication*, vol. 161, no. 1-3, pp. 13–18, 1999.

[44] K. Itoh, “Analysis of the phase unwrapping algorithm”, *Applied Optics*, vol. 21, no. 4, pp. 2470-2470, 1982.

[45] D. C. Ghiglia and M. D. Pritt, *Two-Dimensional Phase Unwrapping: Theory, Algorithms, and Software*. New York, NY: John Wiley & Sons, 1998.

[46] D. J. Bone, “Fourier fringe analysis: The two-dimensional phase unwrapping problem,” *Applied Optics*, vol. 30, no. 25, pp. 3627–3632, 1991.

[47] J. A. Quiroga, A. Gonzalez-Cano, and E. Bernabeu, “Phase unwrapping algorithm based on an adaptive criterion,” *Applied Optics*, vol. 34, no. 14, pp. 2560–2563, 1995.

[48] B. Ströbel, “Processing of interferometric phase maps as complex-valued phasor images,” *Applied Optics*, vol. 35, no. 13, pp. 2192–2198, 1996.

[49] J. Li, X. Su, and J. Li, “Phase unwrapping algorithm based on reliability and edge detection,” *Optical Engineering*, vol. 36, no. 6, pp. 1685–1690, 1997.

[50] M. A. Herráez, D. R. Burton, M. J. Lalor, and M. A. Gdeisat, “Fast two-dimensional phase-unwrapping algorithm based on sorting by reliability following a noncontinuous path,” *Applied Optics*, vol. 41, no. 35, pp. 7437–7444, 2002.

[51] C. Quan, C. J. Tay, L. Chen, and Y. Fu, “Spatial-fringe-modulation-based quality map for phase unwrapping,” *Applied Optics*, vol. 42, no. 35, pp. 7060–7065, 2003.

[52] X. Su and W. Chen, “Reliability-guided phase unwrapping algorithm: A review,” *Optics and Lasers in Engineering*, vol. 42, no. 3, pp. 245–261, 2004.

[53] S. Zhang, X. Li, and S. Yau, “Multilevel quality-guided phase unwrapping algorithm for real-time three-dimensional shape reconstruction,” *Applied Optics*, vol. 46, no. 1, pp. 50–57, 2007.

[54] K. Creath, “Step height measurement using two-wavelength phase-shifting interferometry,” *Applied Optics*, vol. 26, no. 14, pp. 2810–2816, 1987.

[55] Y. Cheng and J. C. Wyant, “Two-wavelength phase shifting interferometry,” *Applied Optics*, vol. 23, no. 24, pp. 4539–4543, 1984.

[56] R. Onodera and Y. Ishii, “Two-wavelength interferometry that uses a Fourier-transform method,” *Applied Optics*, vol. 37, no. 34, pp. 7988–7994, 1998.

[57] J. E. Decker, J. R. Miles, A. A. Madej, R. F. Siemsen, K. J. Siemsen, S. D. Bonth, K. Bustraan, S. Temple, and J. R. Pekelsky, “Increasing the range of unambiguity in step-height measurement with multiplewavelength interferometry-application to absolute long gauge block measurement,” *Applied Optics*, vol. 42, no. 28, pp. 5670–5678, 2003.

[58] M. Roy, C. J. R. Sheppard, G. Cox, and P. Hariharan, “White-light interference microscopy: a way to obtain high lateral resolution over an extended range of heights,” *Optics Express*, vol. 14, no. 15, pp. 6788–6793, 2006.

[59] N. Warnasooriya and M. K. Kim, “LED-based multiwavelength phase imaging interference microscopy,” *Optics Express*, vol. 15, no. 15, pp. 9239–9247, 2007

[60] D. P. Towers, J. D. C. Jones, and C. E. Towers, “Optimum frequency selection in multifrequency interferometry,” *Optics Letters*, vol. 28, no. 11, pp. 1–3, 2003.

[61] C. E. Towers, D. P. Towers, and J. D. C. Jones, “Absolute fringe order calculation using optimisied multifrequency selection in full-filed profilometry,” *Optics and Lasers in Engineering*, vol. 43, no. 7, pp. 788–800, 2005.

[62] L. Song, X. Dong, J. Xi, Y. Yu, and C. Yang, “A new phase unwrapping algorithm based on three wavelength phase shift profilometry method,” *Optics and Laser Technology*, vol. 45, pp. 319–329, 2013.

[63] Y. Xu, S. Jia, X. Luo, J. Yang, and Y. Zhang, “Multi-frequency projected fringe profilometry for measuring objects with large depth discontinuities,” *Optics Communications*, vol. 288, pp. 27–30, 2013.

[64] Y. Xu, S. Jia, Q. Bao, H. Chen, and J. Yang, “Recovery of absolute height from wrapped phase maps for fringe projection profilometry,” *Optics Express*, vol. 22, no. 14, pp. 16819–16828, 2014.

[65] J. M. Huntley and H. O. Saldner, “Temporal phase-unwrapping algorithm for automated interferogram analysis,” *Applied Optics*, vol. 32, no. 17, pp. 3047–3052, 1993.

[66] J. M. Huntley and H. O. Saldner, “Error-reduction methods for shape measurement by temporal phase unwrapping,” *Journal of the Optical Society of America A*, vol. 14, no. 12, pp. 3188–3196, 1997.

[67] H. O. Saldner and J. M. Huntley, “Temporal phase unwrapping: Application to surface profiling of discontinuous objects,” *Applied Optics*, vol. 36, no. 13, pp. 2770–2775, 1997.

[68] S. Zhang, “Digital multiple-wavelength phase-shifting algorithm,” *Proceedings of SPIE*, vol. 7432, p. 74320N, 2009.

[69] S. Zhang, “Phase unwrapping error reduction framework for a multiple-wavelength phase-shifting algorithm,” *Optical Engineering*, vol. 48, no. 10, pp. 105601, 2009.

[70] Y. Ding, J. Xi, Y. Yu, and J. Chicharo, “Recovering the absolute phase maps of two fringe patterns with selected frequencies,” *Optics Letters*, vol. 36, no. 13, pp. 2518–2520, 2011.

[71] Y. Ding, J. Xi, Y. Yu, W. Q. Cheng, S. Wang, and J. Chicharo, “Frequency selection in absolute phase maps recovery with two frequency projection fringes,” *Optics Express*, vol. 20, no. 12, pp. 13238–13251, 2012.

[72] M. J. Baker, J. F. Chicharo, and J. Xi, “An investigation into temporal gamma luminance for digital fringe Fourier transform profilometers”, presented at *IEEE International Symposium on Intelligent Signal Processing, WISP 2007, Madrid, Spain, October 3–5, 2007.*

[73] M. J. Baker, J. Xi, and J. F. Chicharo, “Elimination of γ non-linear luminance effects for digital video projection phase measuring profilometers”, *4th IEEE International Symposium on Electronic Design, Test & Applications, DELTA 2008, Hong Kong, January 23–25, 2008.*

[74] P. S. Huang, Q. Hu, and F. Chiang, “Error compensation for a three-dimensional shape measurement system,” *Optical Engineering*, vol. 42, no. 2, pp. 482-486, 2003.

[75] H. Guo, H. He, and M. Chen, “Gamma correction for digital fringe projection profilometry,” *Applied Optics*, vol. 43, no. 14, pp. 2906–2914, 2004.

[76] S. Zhang and P. S. Huang, “Phase error compensation for a 3-D shape measurement system based on the phase shifting method,” *Optical Engineering*, vol. 46, no. 6, pp. 063601, 2007.

[77] S. Zhang and S. Yau, “Generic nonsinusoidal phase error correction for three-dimensional shape measurement using a digital video projector,” *Applied Optics*, vol. 46, no. 1, pp. 36–43, 2007.

[78] B. Pan, Q. Kemao, L. Huang, and A. Asundi, “Phase error analysis and compensation for nonsinusoidal waveforms in phase-shifting digital fringe projection profilometry,” *Optics Letters*, vol. 34, no. 4, pp. 416–418, 2009.

[79] S. Lei and S. Zhang, “Flexible 3-D shape measurement using projector defocusing,” *Optics Letters*, vol. 34, no. 20, pp. 3080–3082, 2009.

[80] S. Lei and S. Zhang, “Digital sinusoidal fringe pattern generation: Defocusing binary patterns VS focusing sinusoidal patterns,” *Optics and Lasers in Engineering*, vol. 48, no. 5, pp. 561–569, 2010.

[81] K. Liu, Y. Wang, D. L. Lau, Q. Hao, and L. G. Hassebrook, “Gamma model and its analysis for phase measuring profilometry,” *Journal of the Optical Society of America A*, vol. 27, no. 3, pp. 553–562, 2010.

[82] J. L. Flores, G. Torales, J. A. Ferrari, G. Ayubi, O.E. Castillo and M. D. Martino, “Binary coded triangular fringes for 3-D surface-shape measurement,” *Applied Optics*, vol. 52, no. 15, pp. 3576–3582, 2013.

[83] Y. Hu, J. Xi, Z. Yang, E. Li, and J. Chicharo, “Study on generalized analysis model for fringe pattern profilometry,” *IEEE Transaction on Instrumentation and Measurement*, vol 57, no. 1, pp. 160–167, 2008.

[84] Y. Hu, J. Xi, E. Li, J. Chicharo, and Z. Yang, “Three-dimensional profilometry based on shift estimation of projected fringe patterns,” *Applied Optics*, vol. 45, no. 4, pp. 678–687, 2006.

[85] Y. Hu, J. Xi, J. Chicharo, E. Li, and Z. Yang, “Discrete cosine transform based shift estimation for fringe pattern profilometry using generalized analysis model,” *Applied Optics*, vol. 45, no. 25, pp. 6560–6567, 2006.

[86] Y. Hu, J. Xi, J. Chicharo, W. Cheng, and Z. Yang, “Inverse function analysis method for fringe pattern profilometry”, *IEEE Transactions on Instrumentation and Measurement*, vol. 58, no. 9, pp. 3305–3314, 2009.

[87] C. F. Gerald and P. O. Wheatley, *Applied Numerical Analysis*, 5th ed. Harlow, UK: Addison-Wesley, 1994.

[88] HITACHI, “HITACHI CP-X260 series,” [Online]. Available: http://www.projectorcentral.com/pdf/projector_manual_3254.pdf. Accessed 11 Feb 2015.

[89] Q. Hu, P. S. Huang, Q. Fu, and F. Chiang, “Calibration of a three-dimensional shape measurement system,” *Optical Engineering*, vol. 42, no. 2, pp. 487–493, 2003.

[90] K. Wu, J. Xi, Y. Yu, and Z. Yang, “3D profile measurement based on estimation of spatial shifts between intensity ratios from multiple-step triangular patterns,” *Optics and Lasers in Engineering*, vol. 51, no. 4, pp. 440–445, 2013.

[91] P. Jia, J. Kofman, and C. English, “Two-step triangular-pattern phase-shifting method for three-dimensional object-shape measurement,” *Optical Engineering*, vol. 46, no. 8, p. 083201, 2007.

[92] P. Jia, J. Kofman, and C. English, “Multiple-step triangular-pattern phase-shifting and the influence of number of steps and pitch on measurement accuracy,” *Applied Optics*, vol. 46, no. 16, pp. 3253–3262, 2007.

[93] P. Jia, J. Kofman, and C. English, “Intensity-ratio error compensation for triangular-pattern phase-shifting profilometry,” *Journal of the Optical Society of America A*, vol. 24, no. 10, pp. 3150–3158, 2007.

[94] X. Cheng, X. Su, and L. Guo, “Automated measurement method for 360° profilometry of 3-D diffuse objects,” *Applied Optics*, vol. 30, no. 10, pp. 1274–1278, 1991.

[95] H. Guo and M. Chen, “Multiview connection technique for 360-deg three-dimensional measurement,” *Optical Engineering*, vol. 42, no. 4, pp. 900–905, 2003.

[96] L. Li, N. Schemenauer, X. Peng, Y. Zeng, and P. Gu, “A reverse engineering system for rapid manufacturing of complex objects,” *Robotics and Computer-Integrated Manufacturing*, vol. 18, no. 1, pp. 53–67, 2002.

[97] C. Reich, R. Ritter, and J. Thesing, “3-D shape measurement of complex objects by combining photogrammetry and fringe projection,” *Optical Engineering*, vol. 39, no. 1, pp. 224–231, 2000.

[98] L. Song, J. Luo, B. Sun, and Y. Wen, “Two cameras vision model for the 3D shape recovery,” in *Fifth International Conference on Natural Computation*, vol. 6, *Tianjian, China, 14-16 August 2009*,Los Alamitos, CA: IEEE Computer Society, 2009. pp. 246–250.

[99] Y. Wang, K. Liu, Q. Hao, D. Lau, and L. G. Hassebrook, “Multicamera phase measuring profilometry for accurate depth measurement,” in *Proceedings of SPIE, Sensors and Systems for Space Applications*, vol. 6555, May 2007, p. 655509.

[100] E. Stoykova, A. Gotchev, and V. Sainov, “Analysis of a multi-wavelength multi-camera phase-shifting profilometric system for real-time operation,” *Optics Communication*, vol. 284, no. 1, pp. 88–97, 2011.